

HYDRODYNAMIC STUDY OF FEED SPACER GEOMETRY IN SPIRAL WOUND  
MEMBRANE MODULES

A dissertation submitted to the Graduate School of Environmental Engineering, The  
University of Kitakyushu in fulfillment of the requirements for the degree of Doctor of  
Engineering

by

Zhiming Han

March 2019

## **DEDICATION**

I hereby declare that this thesis has not been previously submitted to any other university or institution for obtaining an academic degree. Except quotation and data which are properly cited, this thesis contains my original works. The thesis is only submitted to The University of Kitakyushu in fulfillment of the requirement for a Degree of Doctor of Engineering.

Zhiming Han

Kitakyushu, Japan

March 2019

## **ABSTRACT**

In membrane technology, the two most used configurations of commercial membrane elements are spiral-wound and hollow-fiber. Spiral wound modules (SWM) wrap a leaf around a tube for perforated permeate collection to create a compact structure. Two flat membranes sheets separated by a spacer to form a channel for feed flow are assembled into a leaf. Spacer as an essential part of SWM not only create feed channel but also promote mixing of feed fluid at the same time which affected the flow pattern near membrane surface related to fouling trend and concentration gradient. The performance of conventional spacer woven and non-woven used to enhance mass transfer has been investigated by extensive works. Spacer geometry and the dead zone behind spacer were focused on through many numerical and experimental studies. Based on numerical simulation results indicated that fully woven spacers showed better performance than other configurations in mitigating concentration polarization and delivering water flux by mesh angle of  $60^{\circ}$ , but higher pressure drop was caused than their nonwoven counterpart.

Along with the experimental techniques, the time, cost, and risks were reduced by the computational techniques. As a reliable and efficient numerical analysis tool, CFD has been extensively applied to the flow conditions of the SW membrane modules. The interaction of the many different processes could be assessed through computational simulation. Without building spacers, CFD simulation can investigate hydrodynamics under various feed spacer geometry parameters. With the ongoing developments in CFD

techniques and computational resources, three-dimensional studies are being conducted, which can provide in-depth analysis of concentration patterns and hydrodynamics in membrane modules. In this thesis three-dimensional modeling of flow through spacer filled narrow channels is carried out using CFD package ANSYS CFX to investigate the impact of feed spacer filament on shear stress exerted on membrane surfaces and pressure drop, which two kinds of feed spacers were designed to improve flow pattern.

The processing of the results revealed the characteristics of the feed spacers. For the pillar-like spacer, through reductions in the connecting filament's diameter, the channel porosity reached 0.979. Regarding the maximum porosity, the dimensionless power number was reduced by 47.31% at Reynolds number 150 in comparison with a previously studied commercial spacer. The modified friction factor, as a dimensionless parameter, was employed to investigate the shear stress at the membrane's surface. At dimensionless power number  $10^6$ , the enhancement of the modified friction factor increased by approximately 22.27% in comparison with the results of a previous study. Based on the numerical prediction, the homogenization of shear stress distribution, which changed the flow profile near the membrane, was featured through contour plots. For the arc-like spacer, from 2D velocity vectors and shear stress contour mixing, the flow pattern and dead zone flushing were depicted. The ratio of low shear stress area to the total area increased with the inlet velocity closed to 20%. The energy consumption with respect to flow direction for the arched filament was 80% lower than that in the zigzag filament. Compared with previous commercial spacers' simulation, the friction factor was lower when the main flow was normal to the arched filament and the modified friction factor was close to the

commercial spacers. The homogenization was realized through the flow pattern created by the modified spacer.

## **LIST OF ABBREVIATIONS**

CFD Computational fluid dynamics

CP Concentration polarization

DNS Direct numerical simulation

LES Large eddy simulation

MF Microfiltration

NF Nanofiltration

PIV Particle image velocimetry

RO Reverse osmosis

SWM Spiral wound modules

UF Ultrafiltration

## LIST OF NOTATIONS

$a, b$	the semi-major axis and the semi-minor axis of the intersection elliptic cross-section (m)
$a_1, a_2, a_3, a_4, b_1, b_2, b_3, b_4$	the parameter in function (-)
$d$	diameter of feed spacer filaments/cylinders (m)
$D$	thickness of feed spacer filaments/cylinders (m)
$D_H$	the channel hydraulic diameter (m)
$f$	friction factor (-)
$f_{wall}$	the modified friction factor (-)
$h_f$	height of feed channel (m)
$\Delta L$	the element length (m)
$P$	pressure (Pa)
$\Delta p$	the pressure drop (Pa)
$P_n$	the dimensionless power number (-)
$Q$	flow rate ( $\text{m}^3 \text{s}^{-1}$ )
$Re$	Reynolds number (-)
$Re_{cyl}$	cylinder Reynolds number (-)
$U_{ave}$	average velocity ( $\text{m s}^{-1}$ )
$U_{sup}$	superficial velocity ( $\text{m s}^{-1}$ )
$V_{Spacer}$	feed spacer volume ( $\text{m}^3$ )
$V_{Total}$	channel space volume ( $\text{m}^3$ )

### Greek Letters

$\varepsilon$	feed spacer porosity/voidage
$\mu$	fluid viscosity (Pa s)
$\nu$	the kinematic viscosity (-)

$\rho$  fluid density ( $\text{kg m}^{-3}$ )

$\tau_{wall}$  average shear stress (Pa)

### Subscripts

ave average

sup super



## ACKNOWLEDGMENTS

I would like to thank my supervisor, Professor Hidenari Yasui and Professor Mitsuharu Terashima, without whom this thesis would not have been possible. Thank you for taking me on board and teaching me about the world of membranes, research and academic life. Besides, I would like to thank you committee members including Professor Yo Ito and Professor Masahiro Okuda for the helpful comments and suggestion during my research. I would also like to thank everyone at Hidenari Yasui lab.

Thank you to my closest friends Dr. Magnus So, with whom I shared the PhD adventure, for teaching me CFD simulation ANSYS-CFX. I also express my gratitude to the entire faculty of the Graduate School of Environmental Engineering for helping me in my academic life.

Finally, I would especially like to thank my family. My beloved wife Qing Chen has been extremely supportive of me throughout this entire process and has made countless sacrifices to help me get to this point. My beloved son Jianzhi Han has brought me joy and everyday laughter.

Zhiming Han

Defense Date 2.7.2019

## TABLE OF CONTENTS

DEDICATION .....	II
ABSTRACT.....	III
LIST OF ABBREVIATIONS.....	VI
LIST OF NOTATIONS .....	VII
ACKNOWLEDGMENTS .....	IX
TABLE OF CONTENTS.....	X
LIST OF TABLES.....	XIV
LIST OF FIGURES .....	XVI
CHAPTER1 INTRODUCTION .....	23
1.1 Background and motivation.....	23
1.2 Goals and objectives .....	26
1.3 Organization of this dissertation.....	27
CHAPTER2 LITERATURE SURVEY.....	32
2.1 Introduction.....	32
2.2 Membrane modules.....	33
2.2.1 Plate-and-frame module.....	35
2.2.2 Tubular membrane module.....	36
2.2.3 Hollow-fiber module .....	37
2.2.4 Spiral wound module.....	38
2.3 The parts of SWM.....	40
2.3.1 Collection tube.....	41

2.3.2 Permeate spacer .....	41
2.3.3 Feed spacer .....	42
2.3.4 Anti-telescoping devices.....	43
2.3.5 Module interconnection .....	43
2.3.6 Pressure vessel .....	44
2.4 Basic definitions and concepts.....	44
2.4.1 Fouling.....	44
2.4.2 Concentration polarization (CP).....	46
2.4.3 Shear stress .....	47
2.5 Studies aiming to the different geometry of the feed spacer in SWM modules .....	47
2.5.1 Woven and Unwoven spacer .....	51
2.5.2 Ladder-type spacer.....	56
2.5.3 Multi-spacer.....	58
2.5.4 Others.....	60
CHAPTER3 CFD.....	74
3.1 CFD simulation.....	74
3.1.1 Mathematical formulation .....	77
3.1.2 CFD modeling .....	80
3.1.3 Literature on CFD application .....	84
3.2 CFD protocol .....	85
3.2.1 The finite difference method .....	86
3.2.2 The finite volume method.....	87

3.2.3 The finite element method .....	87
3.3 Programming procedure.....	91
CHAPTER4 PILLAR-LIKE SPACER.....	96
4.1 Introduction.....	96
4.2 Materials and Methods.....	106
4.2.1 Characterization of the Pillar-Like Spacer .....	106
4.2.2 Computational Model .....	111
4.3 Results.....	117
4.3.1 Porosity.....	118
4.3.2 Friction Factor and the Dimensionless Power Number .....	122
4.3.3 The Modified Friction Factor .....	130
4.4 Conclusions.....	135
CHAPTER5 ARC-LIKE SPACER.....	145
5.1 Introduction.....	145
5.2 Modeling .....	156
5.2.1 Characterization of the modified feed Spacer .....	157
5.2.2 Model Description .....	162
5.3 Results and discussion .....	168
5.3.1 Flow Pattern and Shear Stress Distribution .....	168
5.3.2 Validation of Arc-like spacer Simulation .....	177
5.4 Conclusion .....	186
CHAPTER6 GENERAL CONCLUSIONS AND PERSPECTIVES.....	195

6.1 Summary .....	195
6.2 Conclusions.....	198
6.3 Perspectives.....	207

## LIST OF TABLES

Table 2-1 Major milestones in the development of membranes for industrial separations. .....	33
Table 2-2 Selected experiments conducted on visualization of the flow around feed spacers [17].....	48
Table 2-3 Summary of results from numerical 2-D simulations of flow in channels with transverse filaments [76]. ....	50
Table 2-4 Summary of results from 3D in channels with spacer [76]. ....	50
Table 3-1 CFD application in various areas [91]. ....	75
Table 3-2 Summaries of important contributions to membrane studies utilizing 3D CFD [99]. ....	85
Table 3-3 Commercial CFD code list. ....	86
Table 3-4 Summary of characteristics of discretization methods [29]. ....	89
Table 4-1 The selection of conjunction cross-section.....	109
Table 4-2 The selection of connecting filament .....	110
Table 4-3 The pressure drop function parameters. ....	120
Table 4-4 The friction factor function parameters. ....	124
Table 4-5 The dimensionless power number function parameters. ....	129
Table 5-1 The ratio of the control area to total area for the values of shear stress, which are smaller than 10% maximum value or greater than 90% maximum value. ....	176
Table 5-2 The pressure drop function parameters for case A. ....	179
Table 5-3 The pressure drop function parameters for case B. ....	180

Table 5-4 Interpolated value from fixed superficial velocity at Reynolds number 40. .. 183

## LIST OF FIGURES

Figure 2-1 Types of membrane modules. ....	34
Figure 2-2 A schematic view of plate-and-frame module [1].....	35
Figure 2-3 A schematic view of tubular membrane module [2].....	36
Figure 2-4 A schematic view of the hollow fiber module [3].....	37
Figure 2-5 A schematic view of SWM module out of the pressure vessel (A), the unwrapped situation with only two envelopes (B) and side view of the feed channel (C) [4]. ....	38
Figure 2-6 The parts of spiral wound modules. ....	41
Figure 2-7 Factors affecting bacteria attachment to membrane surface [6]. ....	45
Figure 2-8 Typical crossflow membrane filtration showing concentration polarization layer formation [13].....	46
Figure 2-9 Experimental study by using PIV [31].....	48
Figure 2-10 Spacer filament arrangements in 2D channel [63,64].....	51
Figure 2-11 Geometrical characteristics of retentate spacers [62,66].....	52
Figure 2-12 Dimension for spacer filaments and simulation domain [42]. ....	52
Figure 2-13 Transverse filament configurations investigated by Schwinge et al.[37]. ....	53
Figure 2-14 Schematic of the rectangular test cell of Karode and Kumar study [58]. ....	54
Figure 2-15 Schematics and computational domains of Shakaib et al. study [70]. ....	55
Figure 2-16 Spacer configuration of Gu et al. study [71]. ....	56
Figure 2-17 Scheme of ladder-type spacer from [53]. ....	57
Figure 2-18 Ladder-type spacer study comparing with other types of spacer [4]. ....	58



Figure 2-19 The multi-layer spacer investigated by Schwinge et al.[72].	59
Figure 2-20 The twisted tapes spacer with multi-layer designed by Li et al.[73].	60
Figure 2-21 Different shapes of spacer studied by Ranade et al. [59].	60
Figure 2-22 3D printed spacer investigated by Sreedhar et al.[74].	61
Figure 3-1 CFD structure.	74
Figure 3-2 CFD modeling.	80
Figure 3-3 ANSYS CFX structure.	89
Figure 4-1 2 layer and 3 layer spacer reported by Schwinge et al. [4].	98
Figure 4-2 Spacer fouling reported by Vrouwenvelder et al. [5].	99
Figure 4-3 Views of commercial RO membrane surfaces with indentations due to feed-spacer sheet compressed in-between envelopes reported by Karabelas et al. [6].	100
Figure 4-4 Three representative 3D printing technologies [7].	101
Figure 4-5 Images of standard feed spacers differing in thickness made with stereomicroscope at the same magnification factor reported by Araújo, P. A. et al.[10].	101
Figure 4-6 PIV applying in spacer simulation [11].	102
Figure 4-7 Illustration of biofilm development in time in the feed channel with spacer reported by Radu, A. I. et al. [12].	102
Figure 4-8 Velocity vector distribution at velocity equal to (a) 0.5 m/s; (b) 1.0 m/s; (c) 2.0 m/s — two cylinders [17].	104
Figure 4-9 The causes of scale formation in spiral wound RO modules reported by Pervov, Alexei G et al.[14].	105

Figure 4-10 Commercial spacers reported by Da Costa et al. [15].....	105
Figure 4-11 Schematic of tested flow-aligned spacers in Santos et al. study [16]. .....	106
Figure 4-12 A view of the morphology of the pillar-like feed spacer. ....	108
Figure 4-13 The geometrical characteristics of the pillar-like feed spacer.....	109
Figure 4-14 Computational Fluid Dynamics (CFD) model setting. ....	113
Figure 4-15 The pillar-like feed spacer's porosity.....	114
Figure 4-16 The computational grid for the pillar-like feed spacer.....	117
Figure 4-17 The pressure drop, associated with the connecting filament diameter, as a function of (a) the flow rate and (b) the average velocity. ....	119
Figure 4-18 The pressure drop and friction factor as a function of channel porosity for the inlet velocity at 0.04 m/s (at a constant flow rate).....	121
Figure 4-19 Contours of velocity in the main flow direction for the super velocity of 0.04 m/s (red: high, blue: low). (a) $d/a = 2$ ; (b) $d/a = 1$ ; (c) $d/a = 0.5$ ; (d) $d/a = 0.25$ . ...	122
Figure 4-20 The friction factor, associated with the connecting filament diameter, as a function of the Reynolds number. A comparison was made with the friction factor results of Haaksman et al. [23].....	124
Figure 4-21 The contours of total pressure in the main flow direction for the super velocity of 0.04 m/s (red: high, blue: low). (a) $d/a = 2$ ; (b) $d/a = 1$ ; (c) $d/a = 0.5$ ; (d) $d/a = 0.25$ .....	125
Figure 4-22 The friction factor associated with the conjunction cross-section, .....	125
Figure 4-23 The friction factor, associated with the configuration of connecting filament. .....	126

Figure 4-24 Different configuration of traverse filament .....	126
Figure 4-25 The dimensionless power number, associated with the connecting filament diameter, as a function of the Reynolds number. A comparison was made with the dimensionless results of Haaksman et al. [23]. .....	128
Figure 4-26 The dimensionless power number associated with the conjunction cross-section .....	129
Figure 4-27 The dimensionless power number associated with the configuration of connecting filament. ....	130
Figure 4-28 The contour plots of the wall shear stress ( $\tau$ ) profile on the upper membrane and the lower membrane generated by the pillar-like feed spacer. ....	131
Figure 4-29 The modified friction factor, associated with the connecting filament diameter, as a function of the dimensionless power number. A comparison was made with the modified friction factor of Haaksman et al. [23]. ....	133
Figure 4-30 The modified friction factor associated with the conjunction cross-section	133
Figure 4-31 The modified friction factor associated with the configuration of connecting filament. ....	134
Figure 5-1 SWRO plant construction cost breakdown [1]. ....	146
Figure 5-2 Computational reproduction of the modeling of the (left) woven net spacer and the (right) overlapped one [2]. ....	146
Figure 5-3 Conventional net-type spacers mentioned Lee et al. study [3]. ....	147
Figure 5-4 Selected filament arrangements in Gu, Boram et al.[4]. ....	147

Figure 5-5 Details with 2-d substrate concentration distribution and biofilm structures at different substrate concentrations in the feed water reported Radu, A. I. et al.[6]..	149
Figure 5-6 Experimental setup used for water flow measurements and visualization, using particle image velocimetry (PIV) [7].....	149
Figure 5-7 Proposed steps in the development of improved spacers for membrane filtration systems involving, 3D printing, CT scanning and numerical modeling in conjunction with experimental testing [8]. .....	150
Figure 5-8 Milestones of 3D printing in membrane modules design [3].....	150
Figure 5-9 A view of the morphology of the modified feed spacer.....	151
Figure 5-10 Streamline (a) and vorticity contours (b) of Koutsou et al. study [9]. .....	152
Figure 5-11 Solution domain and computational grid for the curved channel in Ranade and Kumar study [10]. .....	152
Figure 5-12 Turbulent kinetic energy distribution at an inlet velocity equals to (a) 0.5 m/s; (b) 1.0 m/s; (c) 2.0 m/s — two opposing cylinders reported by Cao, Z. et al. [12].....	153
Figure 5-13 Configurations of the zigzag spacer and saw-tooth spacer [11]. .....	154
Figure 5-14 The geometrical characteristics of the modified feed. ....	156
Figure 5-15 A view of the representative computational domain, for a stack of flat-sheet membranes, which includes half a retentate and permeate channel with a desalination membrane in-between [14]. .....	157
Figure 5-16 The geometry of the 3D-simulation in Koutsou et al. study [16]. .....	158

Figure 5-17 90 <sup>0</sup> and 45 <sup>0</sup> orientation of the non-woven spacer filament mesh of Fimbres-Weihs et al. study [15].	158
Figure 5-18 Steady-state fluid particle path lines in Koutsou et al. study [17].	159
Figure 5-19 Flow path under different Reynold numbers [18].	161
Figure 5-20 CT scans of commercial spacers. The acronyms refer to the spacer manufacturer: Conwed (CON-1, CON-2), LANXESS (LXS-ASD), Hydranautics (HYD) and Dow Chemical (DOW) [19].	161
Figure 5-21 Channel spacer reported by Da Costa, A. R. et al. [20].	162
Figure 5-22 Schematic of a 3D flow domain depicting the locations of the different boundary conditions reported by Fimbres-Weihs, G. A. et al.[21].	162
Figure 5-23 Solution domain and computational grid for intersection of spacers [10].	163
Figure 5-24 CFD (computational fluid dynamics) model setting.	165
Figure 5-25 Mesh dependence analysis and the adopted mesh for this study.	168
Figure 5-26 (A) Contour plot ( $L/D = 12$ ) of the average wall shear stress ( $\tau$ ) profile on the upper membrane and lower membrane generated by the spacer; flow was from up to down in case A and flow was from left to right in case B (red: High, blue: Low, unit: Pa); (B) streamline of velocity in case A and case B ( $L/D = 12$ , $U_{sup} = 0.06 \text{ m s}^{-1}$ ).	170
Figure 5-27 Contour plot of velocity in case A ( $L/D = 12$ , $U_{sup} = 0.06 \text{ m s}^{-1}$ ).	172
Figure 5-28 Velocity vectors in case A and case B ( $L/D = 12$ , $U_{sup} = 0.06 \text{ m s}^{-1}$ ; in (case A), the main flow was from up to down, and in (case B), the main flow was from right to left for (A) $0.95h_f$ , (B) $0.50h_f$ , and (C) $0.05h_f$ .	177

Figure 5-29 The pressure drop for case A, associated with the element length, as a function of the flow rate and average velocity. ....	180
Figure 5-30 The pressure drop for case B, associated with the element length, as a function of the flow rate and average velocity .....	181
Figure 5-31 The pressure drop gradient of (A) main flow was vertical to arched filament and (B) main flow was vertical to zigzaccg filament, associated with the element length, as a function of the Reynolds number. ....	181
Figure 5-32 Comparison with the friction factor result of Haaksman et al. [9] as a function of Reynolds number. ....	184
Figure 5-33 Comparison with the result of Haaksman et al. [9] in the commercial spacer simulation for the modified friction factor as a function of the dimensionless power number. ....	186

# I

## **Introduction**

*This chapter provides an introduction to membrane technology and to this dissertation. In the first section, important background information and motivation factors are presented (Section 1.1). Next, the goals and objectives of this research are discussed (Section 1.2). In the final section, the structure of this dissertation is outlined (Section 1.3).*

### **1.1 Background and motivation**

The increased water demand is caused by increased population, industrial expansion, tourism, and agriculture development urge augmenting the water supply in many water-stressed or arid regions or countries [1]. Reverse osmosis (RO) as a desalination technology is accepted widely to purify water for drinking or other purposes for the reduction in desalination cost through significant technological advances [2,3]. In membrane technology, the two most used configurations of commercial membrane elements are spiral-wound and hollow-fiber. Spiral wound modules (SWM) wrap a leaf around a tube for perforated permeate collection to create a compact structure. Two flat membranes sheets separated by a spacer to form a channel for feed flow are assembled into a leaf [4].

Concentration polarization and fouling are the inevitable phenomena which are the prime reason to flux reduction in commercial water treatment process [5]. Avoiding fouling membrane materials selection, pretreatment in feed flow and so on were taken into

consideration by many researchers. Spacer as an essential part of SWM not only create feed channel but also promote mixing of feed fluid at the same time which affected the flow pattern near membrane surface related to fouling trend and concentration gradient.

The performance of conventional spacer woven and non-woven used to enhance mass transfer has been investigated by extensive works. Spacer geometry and the dead zone behind spacer were focused on through many numerical and experimental studies. Boram Gu et al. reported the effect of feed spacer geometry on membrane performance and concentration polarization based on CFD simulation [6]. In their study, four types of feed spacer configurations nonwoven, partially woven, middle layer and fully woven spacers were investigated through three-dimensional simulations. Their numerical simulation results indicated that fully woven spacers showed better performance than other configurations in mitigating concentration polarization and delivering water flux by mesh angle of  $60^{\circ}$ , but higher pressure drop was caused than their nonwoven counterpart. Sablani et al. found [7] experimentally a decrease in flux with decreasing spacer thickness, but for the intermediate spacer, thickness maximum permeate flow was generated. Radu et al. reported that substrates rejection due to concentration polarization increased with biofilm thickness, and biofilm remove depended on velocity variation and shear stress [8].

Spacer study is a direct method to improve flow patterns to deduce fouling. In previous studies, three kinds of configurations zigzag, submerge and cavity are focused on in 2-dimensional configuration simulation for classic spacer geometry. Compared the other two zigzag configurations is the most efficient spacer type for a spiral-wound membrane module. But in the open channel, the highest axial pressure drop is the submerge



configuration. From these works, mixing improvement is one of the key methods to optimize flux in the separation process. Spacer configuration can be characterized by the distance between spacer filaments, the angle between the spacer filaments  $\beta$  and the flow attack angle  $\alpha$ . The distance between spacer filaments defines the porosity of the feed channel, and angles define the flow regime and drag force from the spacer.

In typical net-like feed spacer woven and non-woven the flow in feed channel is always divide into boundary region and bulk flow region. In the boundary region, concentration polarization is easily constructed by the undisturbed condition. Mixing two region feed flow is one way to reduce the phenomenon of concentration polarization by spacer configuration in spacer design. Structure improvement for promoting vortexes is a method to enhance the efficiency of heat transfer is similar to mass transfer. Cao et al. reported that enhancement of mass transfer is closely related to the high shear stress value, velocity fluctuation and eddy formation, location and inter-filament distance of the spacers constrain shear stress distribution, mass transfer coefficients and pressure inside the channel [9].

The pressure decrease along the channel and the flux improvement are closely related to the flow pattern, especially the eddy promotion from the feed spacer. Radu et al. [8] reported that substrates rejection due to concentration polarization increased with biofilm thickness, and that biofilm removal depended on the velocity variation and shear stress. To achieve further economic improvements to the operation, the consideration of flow pattern has led to the study of feed spacer geometry.

Extensive experimental and theoretical studies have sought a better understanding of spiral wound (SW) membrane mechanisms and the optimization of feed spacer geometric parameters. The studies have found the advantages of geometric configuration in the development of the feed spacer to promote high shear stresses and mass transfer rates. However, in the stagnant zone, which is behind the line contact filaments, a low flow velocity means fewer shear stresses, lower mass transfer rates, and a quicker membrane flux decline, which are caused by a simultaneous increase in fouling [10]. In early work, Pervov et al. [11] pointed out the influence of the feed spacer on the scale formation process in the SW membrane model, and details of the mineral precipitation in the contact zone of the spacer and membrane were described in this work. It was found that the transverse filaments determined the flow structure, as reported by Da Costa et al. [12] and Santos et al. [13].

## **1.2 Goals and objectives**

Two novel spacers were designed to improve the flow pattern in spiral wound modules. The pillar-like spacer was designed to optimize feed spacer geometry. Compared with the conventional spacer, the contact method of the pillar-like spacer with the membrane changed with the area contact. Hence, it was possible that the diameter of the connecting filaments (transverse filament) had decreased to maximize the channel porosity. The energy consumption and shear stress were analyzed using a numerical method, and the results were compared to those of commercial spacers studied in previous works. The arc-like spacer was designed to enhance the mixing ability, which was constructed with arched filaments and zigzag filaments. In this arc-like spacer design, the filament, which was

parallel to the flow direction, was set as the zigzag configuration, and the transverse filament facing the flow direction was set as the arched filament in order to enhance the mixing between the fluid bulk and fluid elements adjacent to the membrane surface. Furthermore, the conjunction between the arched filament and zigzag filament had a small area of contact with the membrane, which reduced the dead zone caused by the shadow of the filament. The arched filament in the middle of the feed channel enabled the disruption of the solute concentration boundary layer.

### **1.3 Organization of this dissertation**

Membrane technology is a wide and varied field, feed spacer play an important role in separating process, therefore this thesis concentrates on two different novel spacers design to enhance the performance of SWM.

In Chapter 2, a review of the important literature on membrane separation methods, kinds of membrane modules, the parts of SWM and the basic concepts in SWM simulation. Previous studies aiming at the different geometry of spacer and basic concepts applied in this thesis were mentioned in this chapter.

Next, in Chapter 3, CFD as a widely accepted method was introduced. The basic theory of commercial CFD software is also discussed. ANSYS-CFX which was used in the novel spacers design was explained in details.

The design of the novel spacers was considered in Chapter 4 and Chapter 5. The advantages were investigated through CFD simulation. The results show the agreement of the inclination compared with previous studies. The structure improvement of spacer

showed the possibility of enhancing the performance of SWM process though optimizing the flow pattern in the spacer-filled channel.

Finally, in Chapter 6, conclusions are presented and possible directions for future work are discussed.

## Reference

1. Shenvi, S. S.; Isloor, A. M.; Ismail, A. F. A review on RO membrane technology: Developments and challenges. *Desalination* **2015**, *368*, 10–26, doi:10.1016/j.desal.2014.12.042.
2. Williams, M. E. A Brief Review of Reverse Osmosis Membrane Technology. *Engineering* **2003**, 1–29, doi:dx.doi.org/10.1021/cr200190s.
3. Voutchkov, N. Seawater Desalination-Costs and Technology Trends. *Encycl. Membr. Sci. Technol.* **2013**, doi:10.1002/9781118522318.emst115.
4. Cheremisinoff, N. P. *Handbook of water and wastewater treatment technologies*; 2002; ISBN 0750674989.
5. Lipnizki, J.; Jonsson, G. Flow dynamics and concentration polarisation in spacer-filled channels. *Desalination* **2002**, *146*, 213–217, doi:10.1016/S0011-9164(02)00474-5.
6. Gu, B.; Adjiman, C. S.; Xu, X. Y. The effect of feed spacer geometry on membrane performance and concentration polarisation based on 3D CFD simulations. *J. Membr. Sci.* **2017**, *527*, 78–91, doi:10.1016/j.memsci.2016.12.058.
7. Sablani, S. S.; Goosen, M. F. A.; Al-Belushi, R.; Gerardos, V. Influence of spacer thickness on permeate flux in spiral-wound seawater reverse osmosis systems. *Desalination* **2002**, *146*, 225–230, doi:10.1016/S0011-9164(02)00477-0.
8. Radu, A. I.; Vrouwenvelder, J. S.; van Loosdrecht, M. C. M.; Picioreanu, C.; Posadzy-Malaczyńska, A.; Kosch, M.; Hausberg, M.; Rahn, K. H.; Stanisic, G.; Malaczynski, P.; Gluszek, J.; Tykarski, A.; Radu, A. I.; Vrouwenvelder, J. S.; van

- Loosdrecht, M. C. M.; Picioreanu, C. Effect of flow velocity, substrate concentration and hydraulic cleaning on biofouling of reverse osmosis feed channels. *Chem. Eng. J.* **2012**, *188*, 30–39, doi:10.1016/j.cej.2012.01.133.
9. Cao, Z.; Wiley, D. E.; Fane, A. G. CFD simulations of net-type turbulence promoters in a narrow channel. *J. Memb. Sci.* **2001**, *185*, 157–176, doi:10.1016/S0376-7388(00)00643-8.
  10. Radu, A. I.; Bergwerff, L.; van Loosdrecht, M. C. M.; Picioreanu, C. Combined biofouling and scaling in membrane feed channels: a new modeling approach. *Biofouling* **2015**, *31*, 83–100, doi:10.1080/08927014.2014.996750.
  11. Pervov, A. G. Scale formation prognosis and cleaning procedure schedules in reverse osmosis systems operation. *Desalination* **1991**, *83*, 77–118, doi:10.1016/0011-9164(91)85087-B.
  12. Da Costa, A. R.; Fane, A. G. Net-Type Spacers: Effect of Configuration on Fluid Flow Path and Ultrafiltration Flux. *Ind. Eng. Chem. Res.* **1994**, *33*, 1845–1851, doi:10.1021/ie00031a026.
  13. Santos, J. L. C.; Geraldés, V.; Velizarov, S.; Crespo, J. G. Investigation of flow patterns and mass transfer in membrane module channels filled with flow-aligned spacers using computational fluid dynamics (CFD). *J. Memb. Sci.* **2007**, *305*, 103–117, doi:10.1016/j.memsci.2007.07.036.

## Literature Survey

*This chapter presents a critical review of the membrane separation process and membrane modules. The review details the effect of feed spacer and the research method in the published literature.*

### 2.1 Introduction

Pressure-driven membrane processes are used for desalination of seawater and brackish water, potable water production, and for treating industrial effluents. However, as widely accepted the transferring membrane science from the lab to commercial reality was since 1960. But the first recorded study of membrane phenomena appears to 1748 by the French man Abbe Nollet. An animal bladder was used for making the spirit of wine demonstrating semi-permeability for the first time. Dutrechet introduced the term `osmosis` in the 1820s to characterize the spontaneous flow of liquid across a permeable barrier. In 1855 the first synthetic membrane made from nitrocellulose was prepared by Fick. Graham reported the first dialysis experiments with synthetic membranes in 1861. Bechold coined the term `ultrafiltration` in 1906, and Michaels pioneered modern ultrafiltration (UF) in the 1960s. Zigmody developed the microporous filters. In 1927 membrane filters was first commercialized by the Sartorius Company in Germany using the Zigmody process. Reverse osmosis (RO) was first studied in the 1920s. **Table 2-1** shown the membrane milestones.

**Table 2-1** Major milestones in the development of membranes for industrial separations.

<i>Period of years</i>	<i>Advances</i>
1900–1920	Development of first ultrafiltration and microfiltration membranes made from nitrocellulose (Bechhold, Zsigmondy, Bachmann).
1920–1940	Empirical studies on formation of phase inversion membranes (Bjerrum, Manegold, Elford). Development of cellulose acetate ultrafiltration membranes (Dobry, Duclaux).
1940–1960	Development of integrally-skinned asymmetric cellulose acetate membranes for water desalination by reverse osmosis (Loeb and Sourirajan).
1960–1970	Commercialization of reverse osmosis, ultrafiltration, microfiltration, and dialysis membranes.
1970–1980	Development of thin-film composite membranes made by interfacial polymerization (Cadotte, Riley). Cellulose acetate gas separation membranes (Schell).
1980–1990	Commercialization of gas separation and pervaporation membranes (Henis and Tripodi, Tusel, Bruschke).
1990–2000	Development of inorganic membranes for gas separation and pervaporation.
The next millennium	Commercialization of inorganic membranes.

Feed, permeate and reject are consisted of continuous steady-state operation. The semipermeable barrier allows the solvent leakage and various solute molecules through the membrane (permeate) but rejects others. Hence, on the feed side of the membrane, the rejected components generated a concentrated retentate. Furthermore, owing to the product requirement and the characters of the membrane the suitable membrane process was selected for realizing different purposes. Between the intrinsic membrane characteristics and its performance in a particular application, the clear distinction was defined.

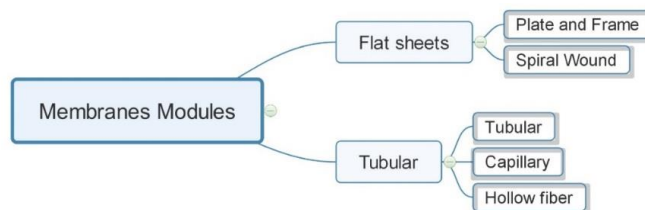
According to the particle size of the solute, and consequently to membrane structure, the pressure-driven membrane processes can be classified in Microfiltration (MF), Ultrafiltration (UF), Nanofiltration (NF) and Reverse Osmosis (RO). When going from microfiltration to reverse osmosis, the size of species or molecules retained diminishes and therefore the pore sizes of the membrane must be smaller. This means that membrane resistance intensifies and consequently the driving pressure applied has to be increased to obtain the same permeation flux.

## 2.2 Membrane modules



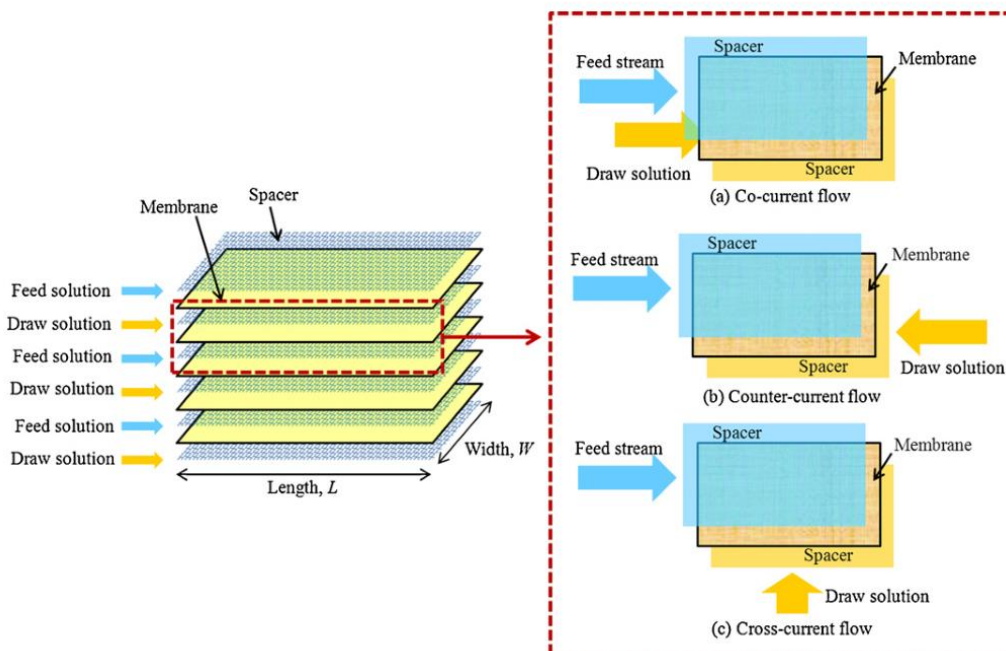
The large membrane area required for commercial separations is tightly packaged into membrane modules. A number of different membrane geometries have been developed for this purpose, but the same design criteria apply in each case. Firstly, for efficient mass transfer, it is essential that there is good contact between the membrane and the fluids flowing through the module. Secondly, to minimize capital costs and plant size, the module must provide as much membrane area per unit volume as. Other important aspects include the cost of manufacture, the fluid-dynamics inside the module, ease of cleaning, and the cost of replacing the membrane.

Four types of membrane module are in common use in the process industries: plate-and-frame modules, tubular modules, hollow-fiber modules, and spiral-wound modules, shown in **Figure 2-1**. Plate-and-frame and Tubular membrane modules were used extensively in the past, but due to the inefficiency, complications associated with their configuration and high cost, they are replaced effectively by the hollow-fiber and spiral wound modules. These configurations now dominate most commercial membrane processes, accounting for almost all new reverse osmosis systems. This is primarily because they offer much larger mass transfer areas than those provided by either tubular or plate-and-frame modules. A brief description of the modules discussed above is given below.



**Figure 2-1** Types of membrane modules.

### 2.2.1 Plate-and-frame module

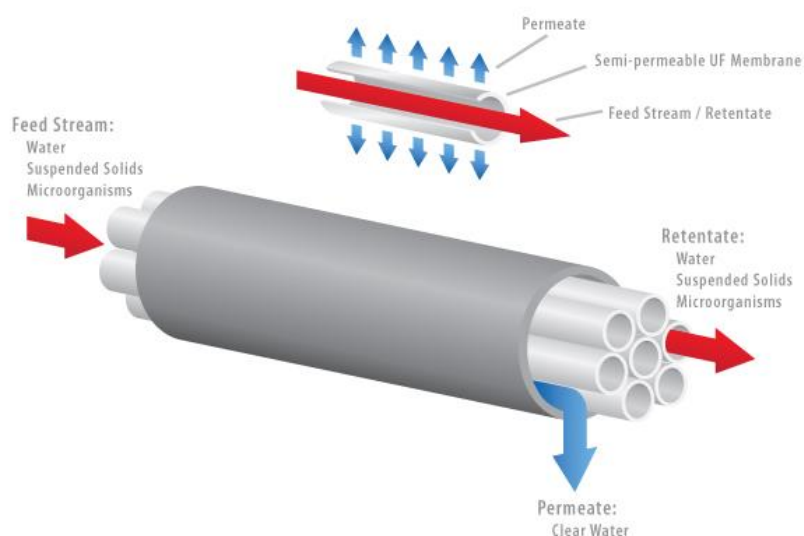


**Figure 2-2** A schematic view of plate-and-frame module [1].

Design of these modules is principally based on a conventional filter press. Plate and frame modules were amongst the earlier design and are now limited small to moderate scale operations [1]. Usually, these modules consist of flat membrane sheets which sit on rectangular plates. The modules are easy to fabricate and use and the areas of the membranes are well defined. The flow channels are made by inserting mesh-like spacers. A number of plates are stacked in parallel or in series. To bear the pressure these modules are equipped with heavy duty end plates. The simplest design consists of several sets of alternating frames. These frames are meant to support the membranes on the permeate side and separate them at the feed side. The assembly is pressed between two end plates and held together with tie rods. Flow enters through one and exits at the other end as shown in **Figure 2-2**. Some alternations to the basic design are also available which use the disc or

elliptical plates instead of rectangular ones and feed flows radially or from one side of the elliptical disc to the other. The major drawback of this type is the very small membrane area per unit separator volume. Packing densities for these modules vary from 100 to 400  $\text{m}^2/\text{m}^3$ . Flat sheet systems offer a very robust and compact design, but for a price. Modern flat sheet systems are built to tolerate very high pressure, in excess of 100 bar. Plate-and-frame modules are still commonly used for pervaporation.

### 2.2.2 Tubular membrane module

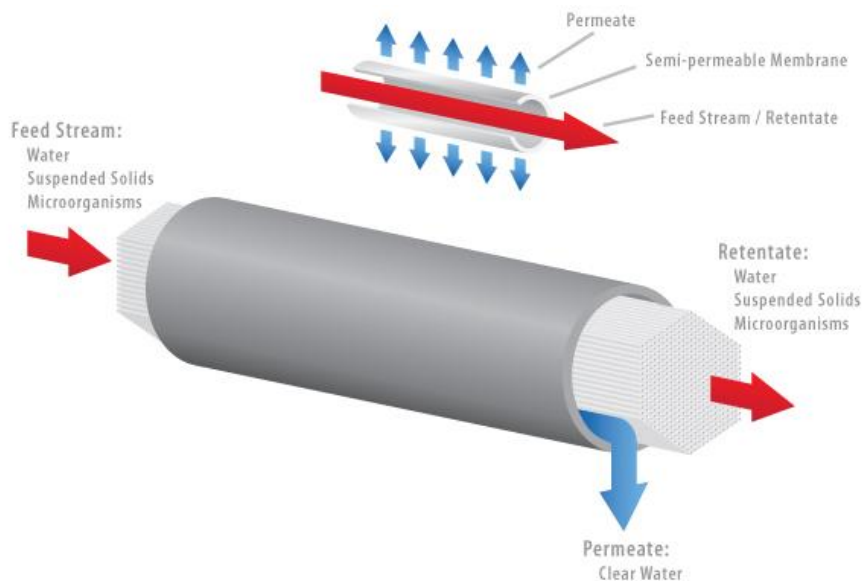


**Figure 2-3** A schematic view of tubular membrane module [2].

Tubular membranes have been around for a long time. The design is simple and easy to understand. These modules are similar to shell and tube heat exchangers and are designed by casting membranes on porous supporting tubes having diameters in the range of 0.125 to 1.0 inch. These tubes must be strong enough to bear the feed stream pressure and usually made up of stainless steel, fiberglass, carbon, ceramics, and porous plastics. These tubes are pressed against tube sheets at each end and are housed in a low-pressure

jacket. As the recovery per tube length is very low so the tubes are connected in series by external U-shaped connections in order to achieve desired recoveries. High-pressure feed is allowed to enter the tube bore and the permeate passes through the membrane and the porous support structure and enters the low-pressure jacket from where it is removed through the permeate ports. The feed gets concentrated along the flow direction until the flow reaches the other end of the tube. Its direction is then reversed and allowed to pass through additional tubes to get the required recovery. The advantages of these modules are, they can be operated at high pressures, membranes can be removed and reformed, low fouling tendency, easy to clean, can achieve high flow velocities and the large and well-defined flow passage. The disadvantages are they are expensive to maintain and operate, such membranes are complex to produce, minimum choice of membrane materials and low membrane surface area to volume ratio restrict their use to moderate scale operations.

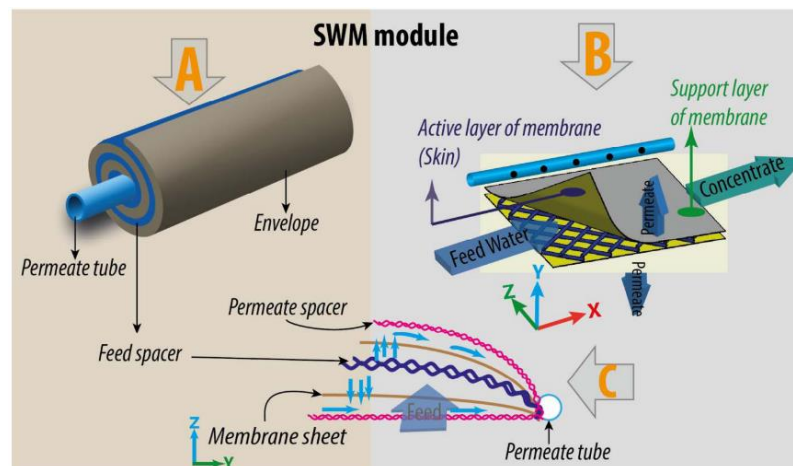
### 2.2.3 Hollow-fiber module



**Figure 2-4** A schematic view of the hollow fiber module [3].

The design of these modules is similar to tubular but the fiber systems are always unsupported. The fiber systems are mechanically weak. Depending upon the fiber dimensions, support mechanism and membrane materials they can be operated with either shell side or lumen side feed. The walls of the fibers need to withstand high pressure to avoid collapse or bursting, depending on the feed introduction mode or method. The outer diameters are usually in the range of 0.5 to 1.0mm, whereas the inner (lumen) diameters are in the range of 0.3 to 0.8mm. These modules contain thousands of fibers arranged in a bundle and potted with special epoxy resins in an outer shell as shown in **Figure 2-4**. The fibers are subjected to high external pressure in case of shell side feed arrangement and can withstand high pressure (10Mpa) required for seawater desalination utilizing reverse osmosis principle.

#### 2.2.4 Spiral wound module



**Figure 2-5** A schematic view of SWM module out of the pressure vessel (A), the unwrapped situation with only two envelopes (B) and side view of the feed channel (C)

[4].

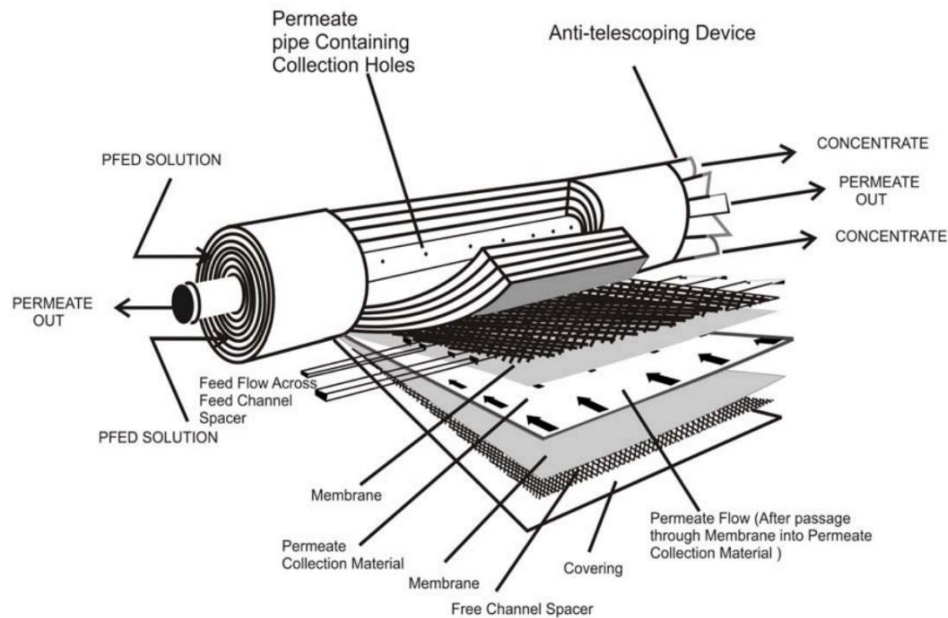
Spiral wound configuration is one of the most popular modules commercially used due to moderate to large surface area per unit volume. They are made up of flat membrane sheets which are glued together at three sides and contains permeate spacer between them. This arrangement referred to as membrane envelop is connected at the fourth open side to a central perforated tube called permeate collection tube. Between two consecutive membrane envelops feed spacer is inserted and the assembly is wound tightly around the central perforated permeate tube. This tight spiral coil is then housed in an outer casing. The function of the permeate spacer is to support the membranes without collapsing under high pressure and also to conduct permeate to the inner perforated central permeate tube.

Design and the flow path through SWM are shown in **Figure 2-6 (A & B)**. **Figure 2-6 (A)** shows the feed stream entering and permeate stream leaving the module in a 15 partial unwound state. It also shows the assembly of membrane envelops by gluing three sides of two flat sheet membranes. Pressurized feed is allowed to pass through narrow feed spacer filled channels. Liquid permeating radially through the membrane surface enters the membrane envelop and guided by the permeate spacer to follow a spiral path to the central perforated permeate collection tube and eventually removed through a permeate port. **Figure 2-6 (B)** represents the end view of SWM and shows the paths followed by the feed and permeate streams. The axial pressure losses over the length of the leaf, due to the presence of feed side spacers and the radial pressure losses over the width of the leaf, due to the presence of permeate spacer produce a distribution of transmembrane pressure drop. SWM is available commercially in 2.5, 4 and 8 inches. These modules are fitted in standard

pressure vessels which can connect several elements in series with O-ring seals in order to prevent feed to permeate flow and bypassing. The individual geometry of SWM is characterized by the number of leaves, length, and width of the leaves. The feed and permeate channel heights are described by the individual feed side and permeate side spacers respectively. The filaments are further described by the porosity, hydraulic diameter, thickness, orientation with respect to each other and with the flow direction and also by the filament mesh and respective shapes.

Major challenges for SWM are concentration polarization, fouling, and high-pressure loss. The performance of SWM is affected by the following main factors [6]: (1) The geometry of the membrane leaves wound spirally to the central tube. This may include the length, width and the number of leaves used. (2) Feed side and permeate side channel heights, which is the direct representation of the feed and permeate side filament thickness. (3) Spacer's orientation, shape, dimensions, and mesh. Since the feed spacer is meant to induce secondary flow patterns to enhance mass transport of the solute away from membrane walls, but at the same time may lead to higher pressure losses. (4) Fouling tendency and cleaning ability. (5) Operating conditions, especially, feed concentration and pressure, percentage permeate recovery and nature of feed pre-treatment.

### **2.3 The parts of SWM**



**Figure 2-6** The parts of spiral wound modules.

### 2.3.1 Collection tube

Permeate collection tube is the central part of the element with perforations. Membrane envelopes are connected to the tube at the fourth (unglued) side. The membrane envelopes having permeated side spacer inside and feed side spacers in between the consecutive envelopes are all wound spirally around this central tube. During the normal course of operation, the permeate flows through the membrane and adopts a spiral flow pattern due to the packing design and presence of permeate spacer, and get collected. Apart from collecting permeate it also provides structural strength to the element [39].

### 2.3.2 Permeate spacer

Permeate spacer is inserted in the membrane envelope and faces the non-active side of the membranes. The permeate flow is guided to the central perforated tube in a



spiral pattern and also serves the purpose of bearing the operational pressure and prevent the membrane from collapsing and hence prevent blockage of the flow path [5]. In other words, their presence is necessary at the permeate side to minimize the membrane compaction. The thickness of permeate spacer normally used in SWM lies in the range of 0.2 to 0.4 mm, which is significantly lower than that for the feed spacer and the porosity is also on the lower side compared to feed spacer. Usually the permeate spacer is made up of tricot material, generally described as epoxy or melamine coated polyester that has been woven.

### **2.3.3 Feed spacer**

Spacer used in feed channel is a net-type sheet made up of low-density polypropylene filaments. The arrangement of the spacer is such that one set of parallel filaments are placed on the top of another set of parallel spacers. Usually, the thickness of the feed spacer is in the range of 28 mils to 34 mils. Filaments that constitute the feed spacer usually have a thickness less than 1mm. The height of the feed channel is defined by the feed spacer thickness [39, 42]. The porosity for the feed spacer is significantly higher than that of the permeate spacer.

Since spiral wound membranes have tightly wrapped structures which cannot be opened easily for chemical cleaning or cannot be backflushed by operating in reverse direction. So the fouling control methods for SWM are limited to hydrodynamics, pretreatment of the feed and operational controls [26]. The fouling issues can be addressed to a larger extent by varying the hydrodynamic conditions prevailing in spiral wound membrane. The feed spacers can be oriented to generate high crossflow velocities or

secondary flow patterns which can develop higher scouring forces on the membrane surface to reduce fouling and concentration polarization. However, this approach will require higher pumping energy to compensate losses within the membrane module. Hence the feed spacers must be optimized to reduce the buildup on the membrane surface with moderate energy loss.

Various types of feed spacer are being used by different manufacturers depending on the feed and operational conditions, such as suspended solids, viscosity, temperature, the presence of fouling species, precipitation or crystal formation propensity are a few to name. Generally, the spacers are available in diamond or ladder array with the mesh size of 4 to 5 mm [39].

#### **2.3.4 Anti-telescoping devices**

To prevent the telescoping potential of the elements, Anti telescoping devices are used at feed and concentrate end of the cartridge. They provide an open flow path as well as a structural sport to the cartridge. At the upstream side or feed end they are meant to carry the brine seal which prevent the feed to by-pass the membrane and at the downstream side or the concentrate end they are meant to support the back face of the element and prevent the membrane leaves to elongate longitudinally due to pressure differential across the element.

#### **2.3.5 Module interconnection**

Module interconnector or interconnector adapter are used to connect modules with each other. These interconnectors have O-rings at both the ends to ensure a tight seal

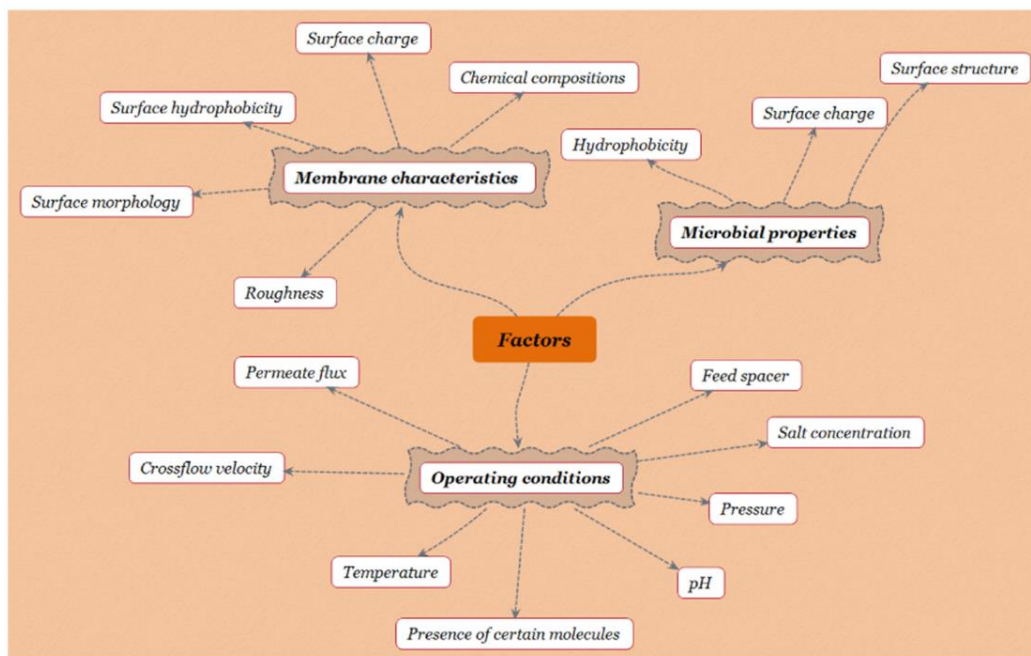
with the module anti-telescoping devices. While connecting the modules using standard anti-telescoping devices end caps having O-rings, there are chances that the O-rings may roll into the membrane module consequently allowing feed and permeate to mix and affecting the process adversely. So while connecting the modules great care must be exercised to prevent rolling of the O-Rings. At time lubrication may minimize the friction and rolling potential of the O-Rings. The anti-telescoping devices end cap comes with an integral O-ring which cannot be rolled or pinched during installation. They also claim that the water hammer cannot wear on the O-Ring as it does on conventional interconnector's O-Ring, which consequently minimizes the feed water leakage propensity to the permeate.

### **2.3.6 Pressure vessel**

SWM are connected in series and placed in the external pressure vessel for use. Depending upon the operational requirement they are available in various pressure ratings. A variety of pressure vessels are available to accommodate 2.5 inches to 18 inches diameter industrial modules. Their length can be as short as to accommodate only one module and they can be as long to accommodate seven modules in series. To facilitate the module replacement in the pressure vessel, the vessels with side-entry and exit for feed and concentrate are preferred over end-entry configuration. This is because in the former case the amount of piping that has to be disconnected to facilitate module replacement is considerably minimized i.e., only the permeate piping has to be disconnected.

## **2.4 Basic definitions and concepts**

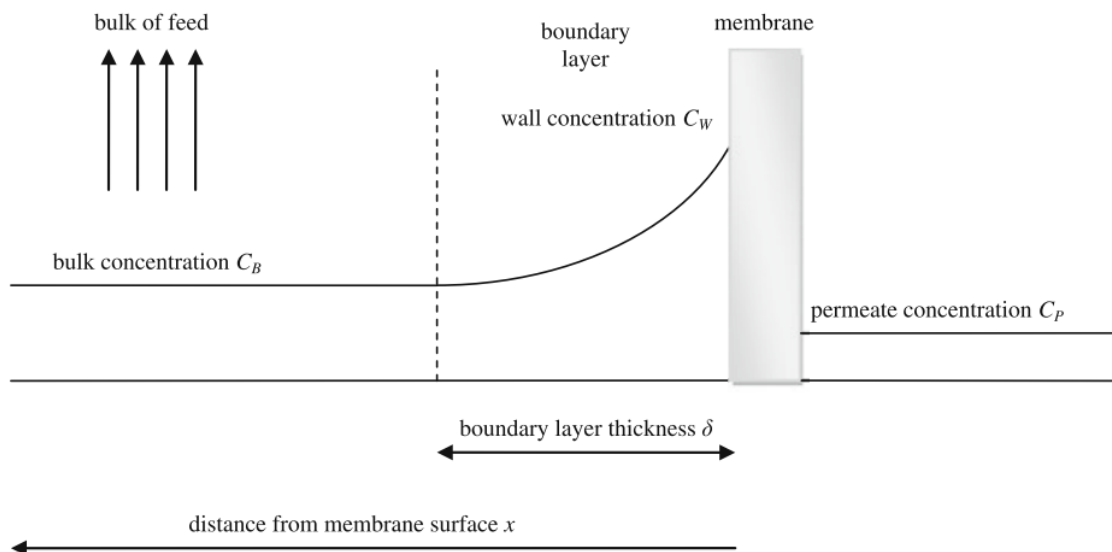
### **2.4.1 Fouling**



**Figure 2-7** Factors affecting bacteria attachment to membrane surface [6].

Membrane fouling is due to the presence of substances in wastewater supply which can interact with it, getting adsorbed and/or precipitating on the surface [6–8]. There can also be substances that penetrate in the interior of the membrane, in which case they are adsorbed on the walls of the pores reducing the pore size [9]. The consequence of contamination is a lower permeate flow due to increased resistance of the membrane. A progressive increase of transmembrane pressure difference, in order to keep the permeate flow, normally accelerates the fouling process reaching a state of irreversible clogging of the membrane, which would require replacement [10]. Plenty of previous studies contributed to understanding the characters of fouling including experimental method and numerical method (2D and 3D) [11,12]. Beside pH, pretreatment, back washing, et al., spacer play an important role on fouling because it defines the flow pattern near the membrane surface shown in **Figure 2-7**.

## 2.4.2 Concentration polarization (CP)



**Figure 2-8** Typical crossflow membrane filtration showing concentration polarization layer formation [13].

It takes place in those processes operating in cross-flow filtration, such as reverse osmosis and ultrafiltration. In the working conditions of these processes, it is difficult to prevent feed rejected components accumulation on the membrane surface. The result is the creation of concentration gradients (concentration polarization) on the supply side, which can hinder the separation efficiency of the membrane and permeate flow. **Figure 2-8** shows a situation where components in the feed, which is rejected by the membrane, gets accumulated on the surface, creating a concentration gradient located in a  $\delta$  thickness film, next to the membrane.

A high polarization level also increases the osmotic pressure in the supply side, which would also contribute to a reduction of permeate flow. Also, if the concentration is high, diffusion components through the membrane will be favored, which leads to a lower

rejection coefficient. Thus, malfunction of the membrane depends on the operating conditions more than membrane using time. The simplest way to avoid polarization is increasing the feed flow velocity rate which is closely related to spacer geometry [14] so that the generated turbulence can remove substances deposited on the surface of the membrane. Wardeh et al. studied the effect of spacer on concentration polarization through 2D numerical method [15].

### 2.4.3 Shear stress

Salt rejection of the RO membrane increases with pressure and decreases with salt concentration. In the study by Song et al., their results indicated that the salt concentrations in the regions adjacent to transverse filaments are very much higher than others [14]. Shear stress, as a key parameter, is defined by the velocity gradient, given that the shear stress on the membrane surface is believed to lower concentration polarization and enhance mass transfer. The modified friction factor employed to select the best feed spacer for mass transfer efficiency was used as a means to analyze shear stress on the membrane [16].

The modified friction factor for the area average shear stress is represented as [16]:

$$f_{wall} = \tau_{wall} \frac{Re^2}{\rho U_{ave}^2} = \tau_{wall} \frac{\rho D_H^2}{\mu^2} \quad (1)$$

where  $\tau_{wall}$  is the average shear stress on the membrane surface.

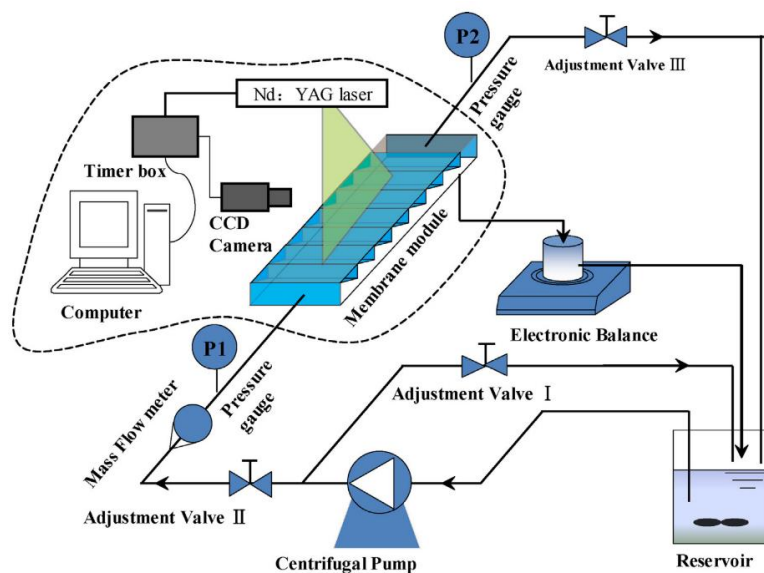
## 2.5 Studies aiming to the different geometry of the feed spacer in SWM modules

Spiral wound modules are widely used for commercial applications including desalination, water treatment, water reclamation, treatment of industrial wastewater, product treatment in the dairy industry and recovery of valuable products in the

pharmaceutical industry [17]. The major problems for SWM application are concentration polarization, fouling, and high-pressure loss. Spacer geometry greatly affects local mixing, mass transfer and pressure loss [18].

**Table 2-2** Selected experiments conducted on visualization of the flow around feed spacers [4].

Researcher	Visualization method	
Da Costa et al.	Injected air bubbles and dye for visualization of flow	[19]
In et al.	Implemented a camera and used ink in water for visualization of laminar flow around the spacers	[20]
Kim et al.	Ink is used as the tracer for visualization of the mass transfer in the 3D net-type promoter in electro dialysis	[21]
Geraldes et al.	An aqueous solution of bromophenol blue is used for the visualization of streams in a ladder-type spacer	[22]
Vrouwenvelde et al.	A solution of potassium permanganate ( $\text{KMnO}_4$ ) is used for visualization of the flow in a flow cell	[23]
Schulenburg et al.	Nuclear Magnetic Resonance Imaging (NMRI) is used to show the spatial distribution of the biofilm and mapping of the velocity field	[24]
Creber et al.	NMRI is used to show the effect of different chemicals on cleaning of RO and NF	[25]
Willems et al.	PIV is used to visualize the effects of two-phase flow in spacer-filled channels	[26]



**Figure 2-9** Experimental study by using PIV [31].

In spite of the numerous investigations to the effect of spacer on the performance of SWM through experimental methods have brought about shown in **Table 2-2**. For instance, 3D print technology application makes it possible that different geometry of spacer is tested directly. The particle image velocimetry (PIV) as a direct, non-invasive,

high-resolution experimental methods is applied in SWM simulation [27–30], showed in **Figure 2-9** [31]. But the local and time-dependent phenomena occurring inside membrane units are still not fully understood. In addition, traditional experimental techniques tend to alter the flow field when trying to make measurements close to the membrane wall, and present difficulties when trying to isolate the different enhancement mechanisms.

Therefore, a different approach is needed for obtaining further understanding of mass transfer enhancement in membrane separation systems. Computational techniques present the potential for improving the understanding of flow pattern in membrane separation systems [32,33]. They have the capability of providing information on flow conditions at any point of the geometry without disturbing the flow. Moreover, the use of numerical modeling significantly reduces the time, costs, and risks associated with running repeated experiments. The numerical technique used for simulating fluid flow is called Computational Fluid Dynamics (CFD) [34]. This section reviews the use and main contributions of CFD to the field of membrane science.

CFD has become a more widely used tool in the field of membrane science [32,35,36], with more and more research groups utilizing this technique in order to gain insight into the phenomena taking place inside membrane modules, to assist the design processes and improve the performance of these modules. Due to its simplicity and smaller computational demands, many researchers have opted for modeling spacer filled channels in two dimensions, as is evidenced by the amount of work undertaken in this area [37–55]. As a result, CFD is now accepted as a reliable tool, and gradually three-dimensional [56–



60] and transient flow studies [41,57,59,61] are beginning to emerge, most of them finding good agreement between predicted and experimental results.

In previous studies, many kinds of spacers were taken into consideration. Most of the commercial spacer was the conventional net-type spacers which were called as woven spacer and nonwoven spacer. Otherwise, ladder-like spacer, multi-layer spacer, and the other geometries were mentioned in numerical simulation. In order to clarify the insights into the mechanisms from the spacer, the mass transfer performance of SWM was focused on by 2D and 3D studies. **Table 2-3** and **Table 2-4** showed the previous studies modeling the unit of SWM.

**Table 2-3** Summary of results from numerical 2-D simulations of flow in channels with transverse filaments [62].

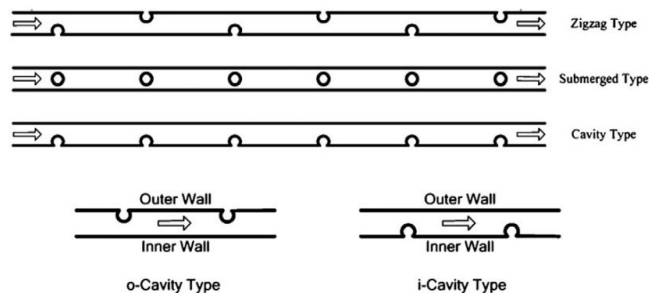
Authors	Simulations	Geometry	Significant Results
Kang and Chang [45]	2D, Steady State	- Zigzag - cavity	- Flow features description - Local Sh number calculation
Cao et al. [46]	2D, Transient k-ε Turbulence model	- cavity - zigzag - submerged	- Pressure drop - Overall mass transfer coefficients
Schwinge et al. [46]	2D, Transient	- single cylindrical filament adjacent to a membrane wall - single cylindrical filament placed at the center of membrane channel - cavity - zigzag - submerged	- Effect of spacer configuration on transition to unsteadiness
Schwinge et al. [48,49]	2D, Steady (?)	- single cylindrical filament adjacent to a membrane wall - single cylindrical filament placed at the center of membrane channel - cavity - zigzag - submerged	Effect of spacer geometry on pressure drop, eddy formation, wall-shear stresses, and mass transfer
Koutsou et al. [41]	2D, Transient, periodic boundary conditions	Submerged	- Temporal and spatial fluid flow description - Time-averaged local shear stress - Pressure drop correlation
Yu-Ling Li et al. [39,50]	2D, Steady State	- submerged - zigzag - i-cavity - o-cavity	Effect of curvature on pressure drop, shear stress and particle deposition

**Table 2-4** Summary of results from 3D in channels with spacer [62].

Authors	Simulations	Geometry	Significant results
Karode and Kumar [61]	3D, Steady-State	Various symmetric and asymmetric commercial spacers	- Total drag as a function of Re number - Average shear rate as a function of inlet velocity - Validation with experiments
Santos et al. [66]	3D, Transient	Ladder-type	- Friction factor as a function of Re and Pn numbers - Spatially averaged Sh number as a function of Pn number
Li et al. [67–69]	3D, periodic boundary conditions	$L/h = 2, 4, 6, 8, 10$ $\alpha = 0, 15, 30, 45^\circ$ $\beta = 60, 120^\circ$	- Sh number as a function of Pn - Pn as a function of Re number - Validation with experiments
Ranade et al. [70]	- 3D, Transient - Periodic BC - k- $\epsilon$ Turbulence model	Various commercial and novel spacers	- Contributions of viscous stress to the overall pressure drop - Drag coefficient as a function of Re number - Axial velocity profiles
Koutsou et al. [38,72]	- 3D, Transient - Periodic BC	$L/D = 6, 8, 10, 12$ $\beta = 90, 60, 120^\circ$	- Description of the temporal evolution of the flow field characteristics - Pressure drop dependence correlations on Re number - Sh number dependence correlations on Re and Sc numbers
Fimbres-Weihs and Wiley [73]	- 3D, Steady State - Periodic BC	$L/D = 6.67$ $\alpha = 45, 90^\circ$ $\beta = 90^\circ$	- Dependence of friction factor on Re number - Overall Sh dependence on Re number - Dependence of energy losses due to form drag on Reynolds number - Dependence of energy losses due to viscous drag on Reynolds number
Shakaib et al. [74,75]	- 3D, steady state - Periodic BC	Diamond shaped -submerged	- Pressure drop and Sh numbers for various spacer configurations

### 2.5.1 Woven and Unwoven spacer

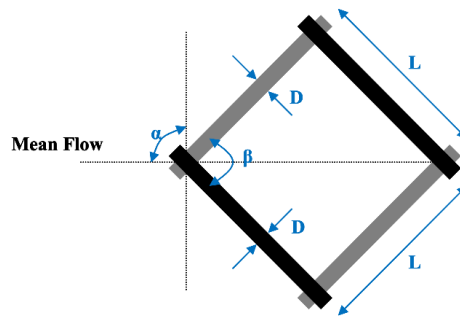
Most of the commercial spacers mentioned in previous studies can be separated as the woven and unwoven spacer. In 2D numerical simulation zigzag, submerged and cavity configuration was focused on showing in **Table 2-4**.



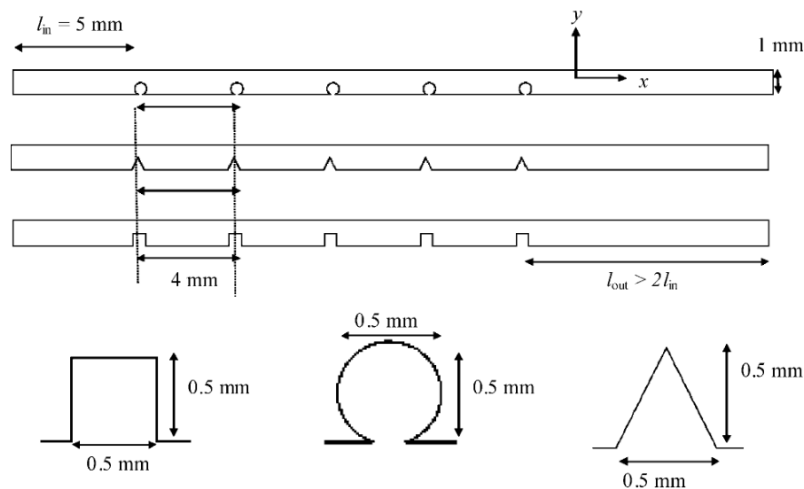
**Figure 2-10** Spacer filament arrangements in 2D channel [63,64].

As concluded by Karabelas et al. [62], the spacer geometry considered in 3D simulations[65–68] is an approximation of the narrow channels with spacers which are encountered in spiral wound elements at the retentate side. The flow field geometry is determined by the net-type filament spacer, which is formed by two layers of straight cylindrical filaments. In each layer the filaments are parallel, having a different orientation, and intersect at a characteristic angle  $\beta$ , as shown in **Figure 2-11**. In general, the geometric

characteristics of such spacers are as follows: (1) Diameter of the top filament,  $D_1$ . (2) Diameter of the bottom filament,  $D_2$ . (3) Distance between the top cylindrical filaments,  $L_1$ . (4) Distance between the bottom cylindrical filaments,  $L_2$ . (5) Angle between crossing filaments,  $\beta$ . (6) Flow attack angle,  $\alpha$ .



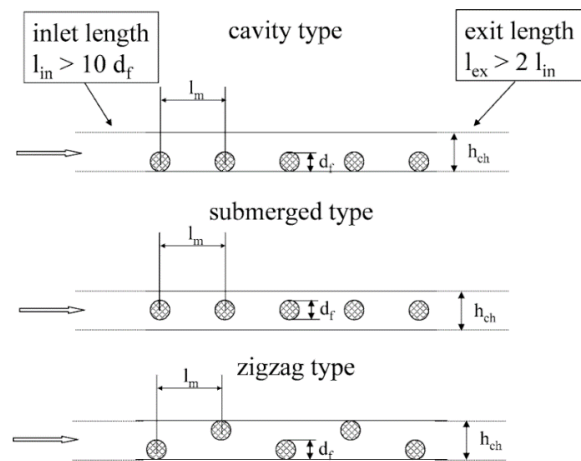
**Figure 2-11** Geometrical characteristics of retentate spacers [62,66].



**Figure 2-12** Dimension for spacer filaments and simulation domain [42].

Ahmad, A. L. et al. reported fluid flow condition adjacent to the membrane interface plays a vital role in controlling mass transfer and concentration polarization mechanism across the membrane [42]. Thus, optimized design of spacer is crucial to deter the formation of concentration polarization layer while maintaining a certain degree of pressure drop. In the paper, turbulence model has been integrated into the solution of time-

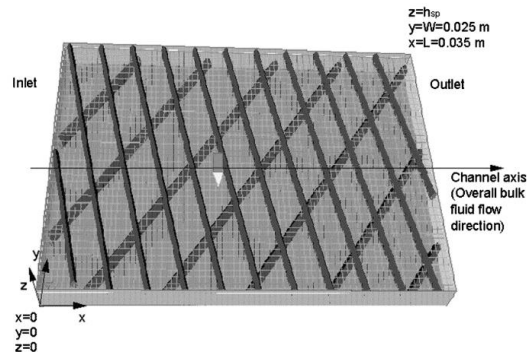
averaged incompressible flow equations. Different types of spacer filament geometries have been analyzed and evaluated to determine their ability to controlling concentration polarization and pressure drop. This study has also demonstrated the dependency of filament geometries performance on feed Reynolds number. This method potentially offers a faster approach to determine the optimum geometries of spacer filament in the narrow membrane channel if compared with experimental methods.



**Figure 2-13** Transverse filament configurations investigated by Schwinge et al.[37].

Schwinge et al. [37,49,69] solved the time-dependent Navier-Stokes equations. They varied the distance between spacers and the diameter of the filaments. For the steady laminar flow conditions, they found that the zigzag geometry performed better than both the cavity and submerged configurations when taking both mass transfer enhancement and pressure loss characteristics into account. They also found that the onset of vortex shedding occurred at a hydraulic Reynolds number between 200 and 400 for the submerged geometry, and between 400 and 800 for the cavity and zigzag configurations. Evidence of vortex shedding for the zigzag geometry is shown in **Figure 2-13** and agrees with the

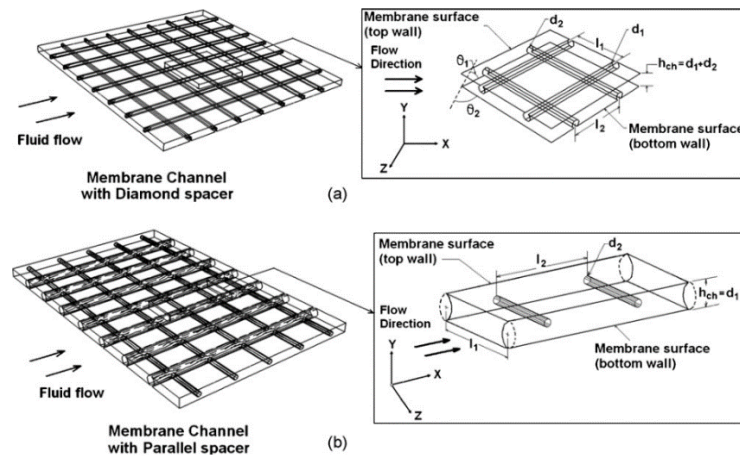
experimental findings of Kang and Chang [20], who found that the flow becomes unsteady at a hydraulic Reynolds number between 455 and 545 for the zigzag and cavity spacers.



**Figure 2-14** Schematic of the rectangular test cell of Karode and Kumar study [58].

Karode and Kumar [58] carried out steady-state three-dimensional simulations of laminar fluid flow without mass transfer in a test cell filled with non-woven net type spacers. The spacers were simulated as cylindrical rods, whose geometric characteristics (diameter, angle, etc.) were taken from commercially available spacers for membrane modules. They modeled the whole test cell with a flat velocity profile at the cell entrance and constant pressure at the outlet. Depending on the characteristics of the spacers, between 8 and 12 filaments were placed in the flow domain. They concluded that a higher degree of mixing in the bulk does not necessarily translate to higher shear at the membrane walls. Their simulations showed a similar zigzag path of the bulk of the fluid to the one observed experimentally by Da Costa et al [19], but only for spacers with large inter-filament distance to filament diameter ratios, which agrees with the results of Shakaib et al. [70]. However, for spacers with low inter-filament distance to filament diameter ratio, they noticed that the bulk of the fluid flows parallel to the spacer filaments, changing direction only when the flow reaches the lateral walls of the test cell. In this latter case, they found

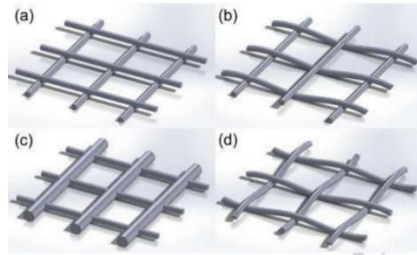
that most of the pressure drop across the channel was due to the shear between the top and bottom layers of fluid moving in different directions.



**Figure 2-15** Schematics and computational domains of Shakaib et al. study [70].

Shakaib et al. [70] reported three-dimensional CFD study is carried out for spacer-obstructed feed channels of membrane elements using FLUENT. The fluid flow behavior is studied by varying geometric parameters of diamond and parallel type spacers. The velocity profiles and hence the average shear stress values significantly depend on the parameters such as transverse filament spacing and filament thickness whereas the effect of axial filament spacing in altering the velocity profiles and shear rates is not that significant. The effect of spacer filament thickness is more pronounced on pressure drop as compared to the effect of spacing between the filaments. The local and average shear stress values also depend on the flow attack angle. When filament spacing and flow attack angles are small, the average shear stress values are high. The shear stress distribution is more uniform in diamond spacers when the flow attack angle is high and in parallel spacers when transverse filament thickness is small. The spacer dimensions can cause unsteadiness

in flow that depends on the channel Reynolds number. The value of critical Reynolds number at which flow becomes unsteady can be as low as 75 when filament spacing and flow attack angles are small and it can be more than 200 for larger flow attack angles.

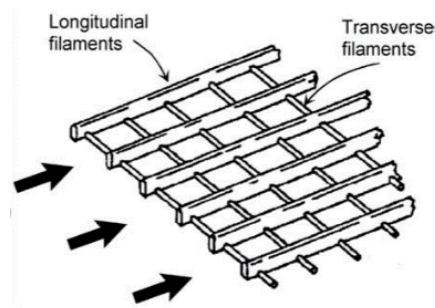


**Figure 2-16** Spacer configuration of Gu et al. study [71].

Gu et al. [71] reported Feed spacers are used in spiral wound reverse osmosis membrane modules to keep the membrane sheets apart as well as to enhance mixing. They are beneficial to membrane performance but at the expense of additional pressure loss. In this study, four types of feed spacer configurations are investigated, with a total of 20 geometric variations based on commercially available spacers and selected filament angles. Numerical simulation results show that for the operating and geometric conditions examined, fully woven spacers outperform other spacer configurations in mitigating concentration polarization. When designed with a mesh angle of  $60^{\circ}$ , fully woven spacers also deliver the highest water flux, although the associated pressure drops are slightly higher than their nonwoven counterparts. Middle layer geometries with a mesh angle of  $30^{\circ}$  produce the lowest water flux. On the other hand, spacers with a mesh angle of  $90^{\circ}$  show the lowest pressure drop among all the filament arrangements examined.

### 2.5.2 Ladder-type spacer

Geraldes et al.[53] investigated flow in spiral wound modules with ladder-type spacers, shown in **Figure 2-17**. In their study, the incompressible laminar and two-dimensional flow in narrow rectangular channels filled with ladder-type spacers that have the transverse filaments adjacent to a semi-permeable wall was investigated in order to have insight on the feed flow in a spiral wound module. Ladder-type spacers with inter-filament distances/channel height ratios ( $L_f$ ) and the ratio ( $P_f$ ) between the transverse filaments height and channel height was investigated in the numerical study and the experiments. The results show that for increasing inter-filament distances the transition critical Reynolds number decreases from 300 to 150. The numerical simulations show that the flow structures are associated with the occurrence of recirculation zones downstream each transverse filament. For low values of the Reynolds number and  $P_f$  and high values of  $L_f$ , the recirculation region does not reach the second filament, while for high values of the Reynolds number and  $P_f$  and low values of  $L_f$  the recirculation region inside the main recirculation region. Each of these situations is associated to different patterns of concentration boundary extends from the first to the second filament.

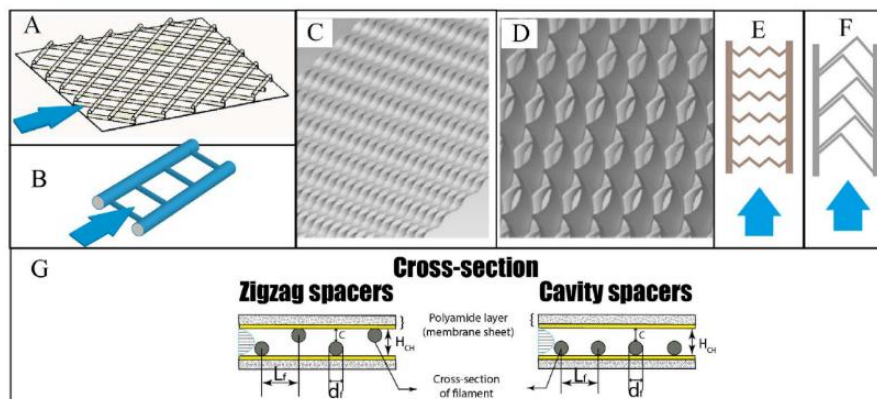


**Figure 2-17** Scheme of ladder-type spacer from [53].

Santos et al. [47] modeled the flow and concentration patterns in spiral wound membrane modules with ladder-type spacers. The results show that for low Reynolds



numbers steady flows are obtained and large recirculation regions are formed after and before the downstream and upstream filaments, respectively. Above a critical Reynolds number, the flow becomes unstable, and vortex shedding occurs, which sweeps the bottom wall surface, breaking down the recirculation regions. As expected, the calculated concentration profiles indicate that concentration polarization will occur in the recirculation regions and at the boundary layer adjacent to the upper and bottom walls. When the flow becomes unsteady, the sweeping effect caused by vortex shedding will disrupt the boundary layers and consequently minimize the concentration polarization.



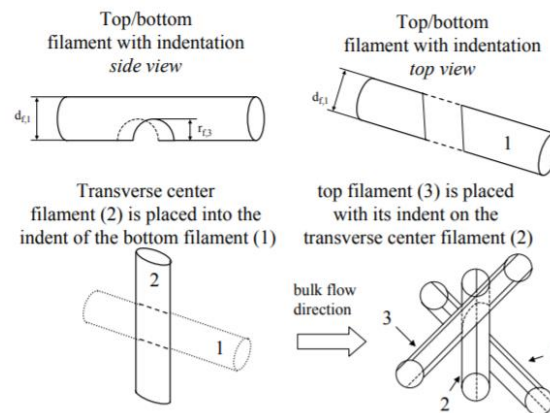
**Figure 2-18** Ladder-type spacer study comparing with other types of spacer [4].

Haidari et al. [4] reviewed the role of the feed spacer in SWM modules and provides an overview of studies conducted in narrow spacer-filled channels to determine the effect of different geometric characteristics of the feed spacer on hydraulic conditions, as shown in **Figure 2-18**. 6 kinds of spacers including ladder-type were taken into consideration in the comparison.

### 2.5.3 Multi-spacer

Schwinge et al. [72] investigated an advanced 3-layer spacer developed with superior mass transfer characteristics and less fouling propensity when compared with

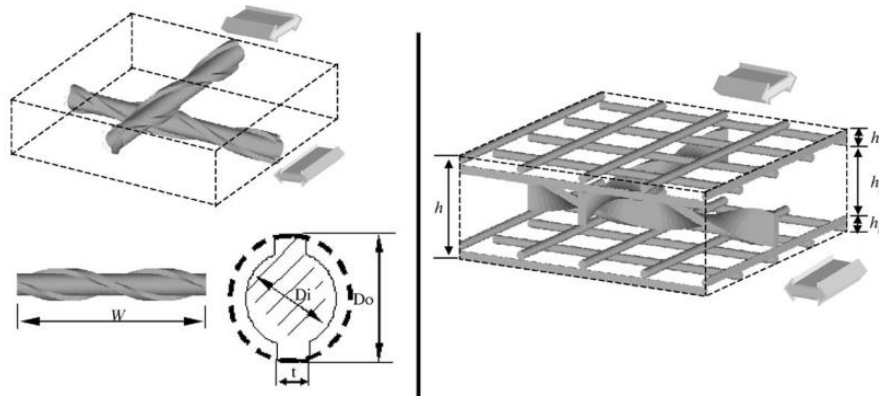
conventional 2-layer spacers. For conventional 2-layer feed spacers, a reduction of the mesh length first increases flux and then flux decreases beyond some optimum mesh length while pressure loss increases continuously with a decrease of the mesh length. The 3-layer spacer improves flux without covering additional membrane area by filaments adjacent to the membrane wall under both fouling and non-fouling conditions. However, the current 3-layer design also increases the pressure loss.



**Figure 2-19** The multi-layer spacer investigated by Schwinge et al.[72].

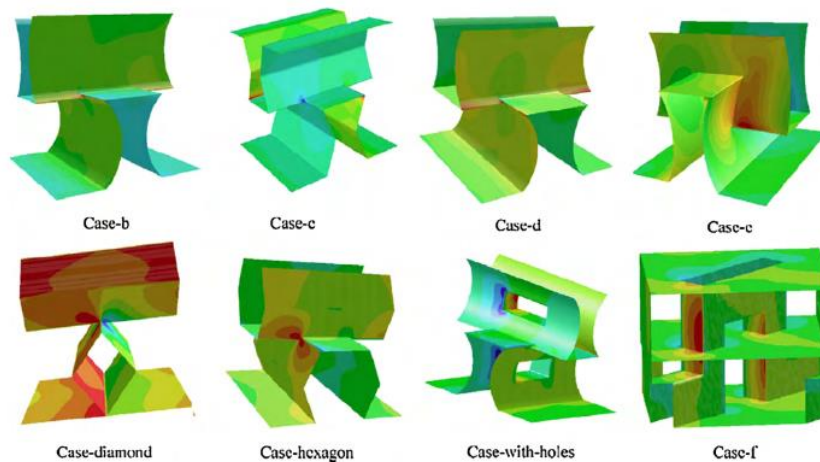
Li et al. [73] reported a novel modified spacer for enhancing the performance of SWM. The mass transfer enhancement of spacers with modified filaments, twisted tapes and multi-layer structures, which were expected to generate these flow patterns, was investigated experimentally. The results indicate that the performance of spacers with modified filaments and twisted tapes is generally worse while the performance of spacers with multi-layer structure is generally better than that of the optimal non-woven net spacer. An optimal multi-layer spacer was designed with optimal non-woven nets in the outer layers and twisted tapes in the middle layer. Its average Sherwood number is about 30% higher than the Sherwood number of the optimal non-woven spacer at the same cross-flow

power consumption whereas the cross-flow power consumption is only about 40% of the consumption of the optimal non-woven spacer at the same Sherwood number.



**Figure 2-20** The twisted tapes spacer with multi-layer designed by Li et al.[73].

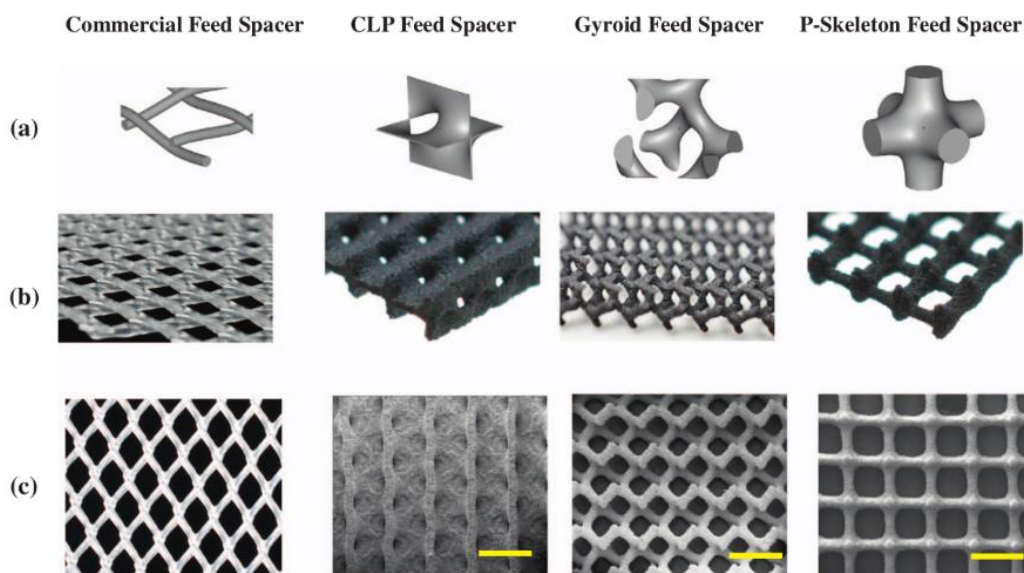
#### 2.5.4 Others



**Figure 2-21** Different shapes of spacer studied by Ranade et al. [59].

Ranade et al. [59] investigated the shape of the spacers used in membrane modules strongly influences the resulting flow and therefore performance of the module. In their study fluid dynamics of rectangular channels similar to membrane modules and containing different spacers was simulated using a three-dimensional CFD model. A 'unit cell' approach was evaluated and used for this purpose. The validated CFD model was used to

evaluate the performance of different spacer shapes and understand the role of spacer shape and resulting fluid dynamics. The models were extended for the first time to simulate flow in spacer filled curvilinear channels, which could be useful in understanding the fluid behavior in spiral modules. The results were compared with those obtained with the flat channel. The approach and results presented in this work will have significant implications for identifying improved spacers with higher propensities to reduce fouling in membrane modules.



**Figure 2-22** 3D printed spacer investigated by Sreedhar et al.[74].

Sreedhar et al. [74] applied 3D print technology to study feed spacers with complex geometries based on triply periodic minimal surfaces (TPMS) were designed and tested in reverse osmosis (RO) and ultrafiltration (UF) processes. The spacers showed a flux enhancement of 15.5% and 38% in brackish water RO and UF tests with the sodium alginate solution, respectively, in comparison to a commercial feed spacer. Moreover, lower feed channel pressure drop was also observed for the TPMS spacers. Biofouling tests

were performed and the membranes were characterized using total organic carbon (TOC) and fluorescence microscopy. The TPMS spacers yielded a reduction in biofouling when compared to commercial feed spacers. Fouling patterns on the membranes were visualized for the different spacers using crystal violet stain, which also revealed a significantly reduced biofilm deposition using the TPMS spacers. The TPMS-based feed spacers have shown great promise in enhancing both RO and UF membrane processes, both in terms of flux enhancement and fouling reduction.

## Reference

1. Gu, B.; Kim, D. Y.; Kim, J. H.; Yang, D. R. Mathematical model of flat sheet membrane modules for FO process: Plate-and-frame module and spiral-wound module. *J. Memb. Sci.* **2011**, *379*, 403–415, doi:10.1016/j.memsci.2011.06.012.
2. PCI Membranes Tubular membranes. *Prod. Tech. Showc.* **2012**.
3. Microfiltration Hollow Fiber Membranes.
4. Haidari, A. H.; Heijman, S. G. J.; van der Meer, W. G. J. Optimal design of spacers in reverse osmosis. *Sep. Purif. Technol.* **2018**, *192*, 441–456, doi:10.1016/j.seppur.2017.10.042.
5. Koutsou, C. P.; Karabelas, A. J.; Goudoulas, T. B. Characteristics of permeate-side spacers of spiral wound membrane modules. *Desalination* **2013**, *322*, 131–136, doi:10.1016/j.desal.2013.05.015.
6. Jiang, S.; Li, Y.; Ladewig, B. P. A review of reverse osmosis membrane fouling and control strategies. *Sci. Total Environ.* **2017**, *595*, 567–583, doi:10.1016/j.scitotenv.2017.03.235.
7. Staal, M.; Farhat, N.; van Loosdrecht, M.; Vrouwenvelder, J. Biofouling patterns in spacer filled channels: High resolution imaging for characterization of heterogeneous biofilms. *Desalin. WATER Treat.* **2017**, *80*, 1–10, doi:10.5004/dwt.2017.20863.
8. Bucs, S. S.; Radu, A. I.; Lavric, V.; Vrouwenvelder, J. S.; Picioreanu, C. Effect of different commercial feed spacers on biofouling of reverse osmosis membrane systems: A numerical study. *Desalination* **2014**, *343*, 26–37,

doi:10.1016/j.desal.2013.11.007.

9. Bu-Ali, Q.; Al-Aseeri, M.; Al-Bastaki, N. An experimental study of performance parameters and ion concentration along a reverse osmosis membrane. *Chem. Eng. Process. Process Intensif.* **2007**, *46*, 323–328, doi:10.1016/j.cep.2006.07.001.
10. Radu, A. I.; Bergwerff, L.; van Loosdrecht, M. C. M.; Picioreanu, C. A two-dimensional mechanistic model for scaling in spiral wound membrane systems. *Chem. Eng. J.* **2014**, *241*, 77–91, doi:10.1016/j.cej.2013.12.021.
11. Van Loosdrecht, M. C. M.; Bereschenko, L.; Radu, A.; Kruithof, J. C.; Picioreanu, C.; Johns, M. L.; Vrouwenvelder, H. S. New approaches to characterizing and understanding biofouling of spiral wound membrane systems. *Water Sci. Technol.* **2012**, *66*, 88–94.
12. Picioreanu, C.; Vrouwenvelder, J. S.; van Loosdrecht, M. C. M. Three-dimensional modeling of biofouling and fluid dynamics in feed spacer channels of membrane devices. *J. Memb. Sci.* **2009**, *345*, 340–354, doi:10.1016/j.memsci.2009.09.024.
13. Keir, G.; Jegatheesan, V. A review of computational fluid dynamics applications in pressure-driven membrane filtration. *Rev. Environ. Sci. Biotechnol.* **2014**, *13*, 183–201, doi:10.1007/s11157-013-9327-x.
14. Song, L.; Ma, S. Numerical studies of the impact of spacer geometry on concentration polarization in spiral wound membrane modules. *Ind. Eng. Chem. Res.* **2005**, *44*, 7638–7645, doi:10.1021/ie048795w.
15. Wardeh, S.; Morvan, H. P. CFD simulations of flow and concentration polarization in spacer-filled channels for application to water desalination. *Chem. Eng. Res. Des.*

- 2008**, *86*, 1107–1116, doi:10.1016/j.cherd.2008.04.010.
16. Santos, J. L. C.; Geraldés, V.; Velizarov, S.; Crespo, J. G. Investigation of flow patterns and mass transfer in membrane module channels filled with flow-aligned spacers using computational fluid dynamics (CFD). *J. Memb. Sci.* **2007**, *305*, 103–117, doi:10.1016/j.memsci.2007.07.036.
  17. Lightfoot, E. N. Membrane separations technology: Principles and applications. *Chem. Eng. Sci.* **1996**, *51*, 325–326, doi:10.1016/S0009-2509(96)90039-1.
  18. Schock, G.; Miquel, A. Mass transfer and pressure loss in spiral wound modules. *Desalination* **1987**, *64*, 339–352, doi:10.1016/0011-9164(87)90107-X.
  19. Da Costa, A. R.; Fane, A. G.; Wiley, D. E. Spacer characterization and pressure drop modelling in spacer-filled channels for ultrafiltration. *J. Memb. Sci.* **1994**, *87*, 79–98, doi:10.1016/0376-7388(93)E0076-P.
  20. In Seok Kang; Ho Nam Chang The effect of turbulence promoters on mass transfer-numerical analysis and flow visualization. *Int. J. Heat Mass Transf.* **1982**, *25*, 1167–1181, doi:10.1016/0017-9310(82)90211-3.
  21. Kim, W. S.; Park, J. K.; Chang, H. N. Mass transfer in a three-dimensional net-type turbulence promoter. *Int. J. Heat Mass Transf.* **1987**, *30*, 1183–1192, doi:10.1016/0017-9310(87)90047-0.
  22. Geraldés, V.; Semião, V.; De Pinho, M. N. The effect of the ladder-type spacers configuration in NF spiral-wound modules on the concentration boundary layers disruption. *Desalination* **2002**, *146*, 187–194, doi:10.1016/S0011-9164(02)00467-8.



23. Vrouwenvelder, J. S. S.; van Paassen, J. A. M. A. M.; Wessels, L. P. P.; van Dam, A. F. F.; Bakker, S. M. M. The Membrane Fouling Simulator: A practical tool for fouling prediction and control. *J. Memb. Sci.* **2006**, *281*, 316–324, doi:10.1016/j.memsci.2006.03.046.
24. Graf von der Schulenburg, D. A. A.; Vrouwenvelder, J. S. S.; Creber, S. A. A.; van Loosdrecht, M. C. M. C. M.; Johns, M. L. L. Nuclear magnetic resonance microscopy studies of membrane biofouling. *J. Memb. Sci.* **2008**, *323*, 37–44, doi:10.1016/j.memsci.2008.06.012.
25. Creber, S. A. A.; Vrouwenvelder, J. S. S.; van Loosdrecht, M. C. M. C. M.; Johns, M. L. L. Chemical cleaning of biofouling in reverse osmosis membranes evaluated using magnetic resonance imaging. *J. Memb. Sci.* **2010**, *362*, 202–210, doi:10.1016/j.memsci.2010.06.052.
26. Willems, P.; Deen, N. G. G.; Kemperman, A. J. B. J. B.; Lammertink, R. G. H. G. H.; Wessling, M.; van Sint Annaland, M.; Kuipers, J. A. M. A. M.; van der Meer, W. G. J. G. J. Use of Particle Imaging Velocimetry to measure liquid velocity profiles in liquid and liquid/gas flows through spacer filled channels. *J. Memb. Sci.* **2010**, *362*, 143–153, doi:10.1016/j.memsci.2010.06.029.
27. Haidari, A. H.; Heijman, S. G. J.; van der Meer, W. G. J. Effect of spacer configuration on hydraulic conditions using PIV. *Sep. Purif. Technol.* **2018**, *199*, 9–19, doi:10.1016/j.seppur.2018.01.022.
28. Haidari, A. H.; Heijman, S. G. J.; van der Meer, W. G. J. Visualization of hydraulic conditions inside the feed channel of Reverse Osmosis: A practical comparison of

- velocity between empty and spacer-filled channel. *Water Res.* **2016**, *106*, 232–241, doi:10.1016/j.watres.2016.10.012.
29. Bucs, S. S.; Valladares Linares, R.; Marston, J. O.; Radu, A. I.; Vrouwenvelder, J. S.; Piciooreanu, C. Experimental and numerical characterization of the water flow in spacer-filled channels of spiral-wound membranes. *Water Res.* **2015**, *87*, 299–310, doi:10.1016/j.watres.2015.09.036.
30. Cabassud, C.; Laborie, S.; Durand-Bourlier, L.; Lainé, J. M. Air sparging in ultrafiltration hollow fibers: Relationship between flux enhancement, cake characteristics and hydrodynamic parameters. In *Journal of Membrane Science*; 2001; Vol. 181, pp. 57–69.
31. Liu, J.; Liu, Z.; Xu, X.; Liu, F. Saw-tooth spacer for membrane filtration: Hydrodynamic investigation by PIV and filtration experiment validation. *Chem. Eng. Process. Process Intensif.* **2015**, *91*, 23–34, doi:10.1016/j.cep.2015.03.013.
32. Soukane, S.; Naceur, M. W.; Francis, L.; Alsaadi, A.; Ghaffour, N. Effect of feed flow pattern on the distribution of permeate fluxes in desalination by direct contact membrane distillation. *Desalination* **2017**, *418*, 43–59, doi:10.1016/j.desal.2017.05.028.
33. Al-Sharif, S.; Albeirutty, M.; Cipollina, A.; Micale, G. Modelling flow and heat transfer in spacer-filled membrane distillation channels using open source CFD code. *Desalination* **2013**, *311*, 103–112, doi:10.1016/j.desal.2012.11.005.
34. Versteeg, H.; Malalasekera, W. *An introduction to computational fluid dynamics: the finite volume method*; 2007;

35. Ghidossi, R.; Veyret, D.; Moulin, P. Computational fluid dynamics applied to membranes: State of the art and opportunities. *Chem. Eng. Process. Process Intensif.* **2006**, *45*, 437–454, doi:10.1016/j.cep.2005.11.002.
36. Schwinge, J.; Wiley, D. E.; Fletcher, D. F. A CFD study of unsteady flow in narrow spacer-filled channels for spiral-wound membrane modules. *Desalination* **2002**, *146*, 195–201, doi:10.1016/S0011-9164(02)00470-8.
37. Schwinge, J.; Wiley, D. E.; Fletcher, D. F. Simulation of unsteady flow and vortex shedding for narrow spacer-filled channels. *Ind. Eng. Chem. Res.* **2003**, *42*, 4962–4977, doi:10.1021/ie030211n.
38. Pellerin, E.; Michelitsch, E.; Darcovich, K.; Lin, S.; Tam, C. M. Turbulent transport in membrane modules by CFD simulation in two dimensions. *J. Memb. Sci.* **1995**, *100*, 139–153, doi:10.1016/0376-7388(94)00250-3.
39. Wiley, D. E.; Fletcher, D. F. Techniques for computational fluid dynamics modelling of flow in membrane channels. *J. Memb. Sci.* **2003**, *211*, 127–137, doi:10.1016/S0376-7388(02)00412-X.
40. Fletcher, D. F.; Wiley, D. E. A computational fluids dynamics study of buoyancy effects in reverse osmosis. *J. Memb. Sci.* **2004**, *245*, 175–181, doi:10.1016/j.memsci.2004.07.023.
41. Koutsou, C. P.; Yiantsios, S. G.; Karabelas, A. J. Numerical simulation of the flow in a plane-channel containing a periodic array of cylindrical turbulence promoters. *J. Memb. Sci.* **2004**, *231*, 81–90, doi:10.1016/j.memsci.2003.11.005.
42. Ahmad, A. L.; Lau, K. K.; Abu Bakar, M. Z. Impact of different spacer filament

- geometries on concentration polarization control in narrow membrane channel. *J. Memb. Sci.* **2005**, *262*, 138–152, doi:10.1016/j.memsci.2005.06.056.
43. Ahmad, A. L.; Lau, K. K.; Bakar, M. Z. A.; Shukor, S. R. A. Integrated CFD simulation of concentration polarization in narrow membrane channel. *Comput. Chem. Eng.* **2005**, *29*, 2087–2095, doi:10.1016/j.compchemeng.2005.06.001.
44. Subramani, A.; Kim, S.; Hoek, E. M. V Pressure, flow, and concentration profiles in open and spacer-filled membrane channels. *J. Memb. Sci.* **2006**, *277*, 7–17, doi:10.1016/j.memsci.2005.10.021.
45. Alexiadis, A.; Bao, J.; Fletcher, D. F.; Wiley, D. E.; Clements, D. J. Analysis of the dynamic response of a reverse osmosis membrane to time-dependent transmembrane pressure variation. *Ind. Eng. Chem. Res.* **2005**, *44*, 7823–7834, doi:10.1021/ie050290y.
46. Alexiadis, A.; Bao, J.; Fletcher, D. F.; Wiley, D. E.; Clements, D. J. Dynamic response of a high-pressure reverse osmosis membrane simulation to time dependent disturbances. *Desalination* **2006**, *191*, 397–403, doi:10.1016/j.desal.2005.07.031.
47. Santos, J. L. C.; Geraldes, V.; Velizarov, S.; Crespo, J. G. Modelling of flow and concentration patterns in spiral wound membrane modules with ladder-type spacers. *Desalination* **2006**, *200*, 395–396, doi:10.1016/j.desal.2006.03.345.
48. Cao, Z.; Wiley, D. E.; Fane, A. G. CFD simulations of net-type turbulence promoters in a narrow channel. *J. Memb. Sci.* **2001**, *185*, 157–176, doi:10.1016/S0376-7388(00)00643-8.
49. Schwinge, J.; Wiley, D. E.; Fletcher, D. F. Simulation of the Flow around Spacer

- Filaments between Channel Walls. 2. Mass-Transfer Enhancement. *Ind. Eng. Chem. Res.* **2002**, *41*, 4879–4888, doi:10.1021/ie011015o.
50. Geraldes, V.; Semião, V.; De Pinho, M. N. Flow and mass transfer modelling of nanofiltration. *J. Memb. Sci.* **2001**, *191*, 109–128, doi:10.1016/S0376-7388(01)00458-6.
51. Geraldes, V.; Semiao, V.; Norberta De Pinho, M. The effect on mass transfer of momentum and concentration boundary layers at the entrance region of a slit with a nanofiltration membrane wall. *Chem. Eng. Sci.* **2002**, *57*, 735–748, doi:10.1016/S0009-2509(01)00441-9.
52. De Pinho, M. N.; Semião, V.; Geraldes, V. V. Integrated modeling of transport processes in fluid/nanofiltration membrane systems. *J. Memb. Sci.* **2002**, *206*, 189–200, doi:10.1016/S0376-7388(01)00761-X.
53. Geraldes, V.; Semião, V.; De Pinho, M. N. Flow management in nanofiltration spiral wound modules with ladder-type spacers. *J. Memb. Sci.* **2002**, *203*, 87–102, doi:10.1016/S0376-7388(01)00753-0.
54. Geraldes, V.; Semiao, V.; Pinho, M. N. Hydrodynamics and concentration polarization in NF/RO spiral-wound modules with ladder-type spacers. *Desalination* **2003**, *157*, 395–402, doi:10.1016/S0011-9164(03)00422-3.
55. Geraldes, V.; Semiao, V.; De Pinho, M. N. Concentration polarisation and flow structure within nanofiltration spiral-wound modules with ladder-type spacers. *Comput. Struct.* **2004**, *82*, 1561–1568, doi:10.1016/j.compstruc.2004.03.052.
56. Li, F.; Meindersma, W.; De Haan, A. B.; Reith, T. Optimization of commercial net

- spacers in spiral wound membrane modules. *J. Memb. Sci.* **2002**, *208*, 289–302, doi:10.1016/S0376-7388(02)00307-1.
57. Koutsou, C. P.; Yiantsios, S. G.; Karabelas, A. J. Direct numerical simulation of flow in spacer-filled channels: Effect of spacer geometrical characteristics. *J. Memb. Sci.* **2007**, *291*, 53–69, doi:10.1016/j.memsci.2006.12.032.
58. Sandeep, K.; Karode, S. K.; Kumar, A. Flow visualization through spacer filled channels by computational fluid dynamics I. Pressure drop and shear rate calculations for flat sheet geometry. *J. Memb. Sci.* **2001**, *193*, 69–84, doi:10.1016/S0376-7388(01)00494-X.
59. Ranade, V. V.; Kumar, A. Fluid dynamics of spacer filled rectangular and curvilinear channels. *J. Memb. Sci.* **2006**, *271*, 1–15, doi:10.1016/j.memsci.2005.07.013.
60. Asadi Tashvigh, A.; Fouladitajar, A.; Zokaee Ashtiani, F. Modeling concentration polarization in crossflow microfiltration of oil-in-water emulsion using shear-induced diffusion; CFD and experimental studies. *Desalination* **2015**, *357*, 225–232, doi:10.1016/j.desal.2014.12.001.
61. Yang, K. Numerical Investigation of Instability and Transition in an Obstructed Channel Flow. *AIAA J.* **2000**, *38*.
62. Karabelas, A. J.; Kostoglou, M.; Koutsou, C. P. Modeling of spiral wound membrane desalination modules and plants - review and research priorities. *Desalination* **2015**, *356*, 165–186, doi:10.1016/j.desal.2014.10.002.
63. Li, Y. L.; Tung, K. L. The effect of curvature of a spacer-filled channel on fluid flow

- in spiral-wound membrane modules. *J. Memb. Sci.* **2008**, *319*, 286–297, doi:10.1016/j.memsci.2008.03.069.
64. Li, Y. L.; Tung, K. L.; Chen, Y. S.; Hwang, K. J. CFD analysis of the initial stages of particle deposition in spiral-wound membrane modules. *Desalination* **2012**, *287*, 200–208, doi:10.1016/j.desal.2011.10.001.
65. Lau, K. K.; Abu Bakar, M. Z.; Ahmad, A. L.; Murugesan, T. Feed spacer mesh angle: 3D modeling, simulation and optimization based on unsteady hydrodynamic in spiral wound membrane channel. *J. Memb. Sci.* **2009**, *343*, 16–33, doi:10.1542/peds.2006-2759.
66. Saeed, A.; Vuthaluru, R.; Yang, Y.; Vuthaluru, H. B. Effect of feed spacer arrangement on flow dynamics through spacer filled membranes. *Desalination* **2012**, *285*, 163–169, doi:10.1016/j.desal.2011.09.050.
67. Koutsou, C. P.; Karabelas, a. J. Towards optimization of spacer geometrical characteristics for spiral wound membrane modules. *Desalin. Water Treat.* **2010**, *18*, 139–150, doi:10.5004/dwt.2010.1382.
68. Tamburini, A.; La Barbera, G.; Cipollina, A.; Ciofalo, M.; Micale, G. CFD simulation of channels for direct and reverse electrodialysis. *Desalin. Water Treat.* **2012**, *48*, 370–389, doi:10.1080/19443994.2012.705084.
69. Schwinge, J.; Wiley, D. E.; Fletcher, D. F. Simulation of the flow around spacer filaments between narrow channel walls. 1. Hydrodynamics. *Ind. Eng. Chem. Res.* **2002**, *41*, 2977–2987, doi:10.1021/ie010588y.
70. Shakaib, M.; Hasani, S. M. F.; Mahmood, M. Study on the effects of spacer

- geometry in membrane feed channels using three-dimensional computational flow modeling. *J. Memb. Sci.* **2007**, *297*, 74–89, doi:10.1016/j.memsci.2007.03.010.
71. Gu, B.; Adjiman, C. S.; Xu, X. Y. The effect of feed spacer geometry on membrane performance and concentration polarisation based on 3D CFD simulations. *J. Memb. Sci.* **2017**, *527*, 78–91, doi:10.1016/j.memsci.2016.12.058.
72. Schwinge, J.; Wiley, D. E.; Fane, A. G. Novel spacer design improves observed flux. *J. Memb. Sci.* **2004**, *229*, 53–61, doi:10.1016/j.memsci.2003.09.015.
73. Li, F.; Meindersma, W.; De Haan, A. B.; Reith, T. Novel spacers for mass transfer enhancement in membrane separations. *J. Memb. Sci.* **2005**, *253*, 1–12, doi:10.1016/j.memsci.2004.12.019.
74. Sreedhar, N.; Thomas, N.; Al-Ketan, O.; Rowshan, R.; Hernandez, H.; Abu Al-Rub, R. K.; Arafat, H. A. 3D printed feed spacers based on triply periodic minimal surfaces for flux enhancement and biofouling mitigation in RO and UF. *Desalination* **2018**, *425*, 12–21, doi:10.1016/j.desal.2017.10.010.



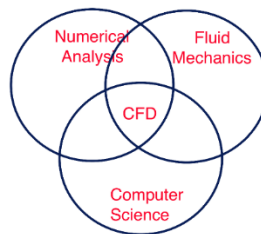
# I

## CFD

*This chapter presents the concepts and fundamentals behind Computational Fluid Dynamics (CFD), which is the main technique used for obtaining the data analyzed in this thesis. In addition, it explains the procedure used for transforming the partial differential equations that describe fluid dynamics into algebraic equations that can be solved via numerical methods in previous studies. Lastly, the methodology for ensuring that the results obtained are reliable and realistic is described in ANSYS CFX.*

### 3.1 CFD simulation

The history of Computational Fluid Dynamics, or CFD for short, started in the early 1970s. Around that time, it became an acronym for a combination of physics, numerical mathematics, and, to some extent, computer sciences employed to simulate fluid flows, showed in **Figure 3-1**.



**Figure 3-1** CFD structure.

Computational fluid dynamics (CFD) uses powerful computers and applied mathematics to model fluid flow situations. The yardstick of success is how well the results of numerical simulation agree with the experiment in cases where careful laboratory

experiments can be established, and how well the simulations can predict highly complex phenomena that cannot be isolated in the laboratory [1]. As a developing science, CFD has received extensive attention throughout the international community since the advent of the digital computer. Since the late 1960s, there has been considerable growth in the development and application of CFD to all aspects of fluid dynamics [2]. As a result, CFD has become an integral part of the engineering design and analysis environment of many companies because of its ability to predict the performance of new designs or processes before they are ever manufactured or implemented.

**Table 3-1** CFD application in various areas [3].

Industrial applications	Aerospace Architecture Automotive Biomedical Chemical and Process Combustion Electronics and computers Glass manufacturing HVAC (heat, ventilation and cooling) Petroleum Power Marine Mechanical Metallurgical Nuclear Train design Turbo machinery Water
Environmental applications	Atmospheric pollution Climate calculations Fire in buildings Oceanic flows Pollution of natural waters Safety
Physiological applications	Cardiovascular flows (heart, major vessels) Flow in lungs and breathing passages

CFD has grown from a mathematical curiosity to become an essential tool in almost every branch of fluid dynamics. It allows for a deep analysis of the fluid mechanics and local effects in a lot of equipment. Most of the CFD results will give improved performance, better reliability, more confident scale-up, improved product consistency,

and higher plant productivity. Some design engineers actually use CFD to analyze new systems before deciding which and how many validation tests need to be performed.

- It provides a detailed understanding of flow distribution, weight losses, mass and heat transfer, particulate separation.
- It makes it possible to evaluate geometric changes with much less time and cost that would be involved in laboratory testing.
- It is able to reduce scale-up problems because the models are based on fundamental physics and are scale independent.

CFD is a method to numerically analyze a fluid flow system which is able to associate with chemical reaction, fluid dynamics, heat and mass transfer [4]. CFD simulation applies the numerical analysis method which numerically approximates the mathematical model which governing the fluid flow phenomenon. As the nature of the numerical analysis, CFD is able to simplify the complicated model governing the membrane separation mechanism which enables the user to reduce the lead time in geometry model construction. With the capability of CFD in numerically solving the governing mathematical model, it enables the user to investigate the membrane separation phenomenon such as fluid flow [5,6]. Whenever the computing facilities are available, CFD is able to perform the almost unrestricted level of system details in the membrane separation and study the phenomenon where the controlled experiment is unable to be performed [4].

Many researchers are utilizing CFD technique to gain insight into various phenomena taking place within the membrane modules to improve its performance or to

provide valuable information for the design process. Moreover, many research groups have shifted their focus to CFD making it a widely used tool in the field of membrane science [7]. The advantage of CFD tool over the traditional experimental methods lies in the built-in flexibility to change operating conditions, fluid properties and geometric parameters of the flow channel. For instance, geometric parameters of the flow channel can be varied using appropriate CFD software and do not need the physical construction of the modified channel, to investigate the effects on parameters of interest. Similarly, fluid properties and operating conditions can be varied to investigate their impact on the parameters of interest without experimentations. Another important and interesting feature of the CFD is that the data can be reported anywhere in the computational domain at any time during the simulation without obstructing the flow itself.

### **3.1.1 Mathematical formulation**

#### **3.1.1.1 Governing equations**

The governing equations will be solved by numerical iteration until the solution is converged. The final result will be presented in the graphical user interface in post-process for the user in-depth analysis [4]. The governing equations in CFD which involves fluid flow and heat transfer are mathematically written from the conservation law of physics including the phenomenon of mass, momentum and energy.

The equations governing fluid motion are the three fundamental principles of mass, momentum, and energy conservation.

Continuity  $\frac{\partial \rho}{\partial t} + \nabla \cdot (\rho V) = 0$

$$\text{Momentum} \quad \rho \frac{DV}{Dt} = \nabla \cdot \tau_{ij} - \nabla p + \rho F$$

$$\text{Energy} \quad \rho \frac{De}{Dt} + p(\nabla \cdot V) = \frac{\partial Q}{\partial t} - \nabla \cdot q + \Phi$$

where  $\rho$  is the fluid density,  $V$  is the fluid velocity vector,  $\tau_{ij}$  is the viscous stress tensor,  $p$  is pressure,  $F$  is the body forces,  $e$  is the internal energy,  $Q$  is the heat source term,  $t$  is time,  $\Phi$  is the dissipation term, and  $\nabla \cdot q$  is the heat loss by conduction. Fourier's law for heat transfer by conduction can be used to describe  $q$  as:

$$q = -k\nabla T$$

where  $k$  is the coefficient of thermal conductivity, and  $T$  is the temperature. Depending on the nature of physics governing the fluid motion one or more terms might be negligible.

### 3.1.1.2 Boundary conditions

The governing equation of fluid motion are solved basing on the boundary conditions and the initial conditions are specified. Any partial differential equation depends on the equation itself require the form of the boundary conditions. Common boundary conditions are listed below:

1) Dirichlet boundary condition:

$$\phi = f_1(x, y, z)$$

Here the values of the variable  $\phi$  on the boundary are known as constants  $f_1$ . This allows a simple substitution to be made to fix the boundary value. For example, the flow velocity may be fixed at the boundary of the domain. Fro the no-slip and no-penetration conditions on the solid walls, the fluid velocity is the same as the velocity of the wall.

2) Neuman boundary condition:

$$\frac{\partial \phi}{\partial n} = f_2(x, y, z)$$

Here the derivatives of the variable  $\phi$  on the boundary are known  $f_2$ , and this gives an extra equation, which can be used to find the value at the boundary. For example, the velocity does not change downstream of the flow, the derivative of  $u$  is zero at that boundary.

3) Mixed type boundary condition:

$$a\phi + b \frac{\partial \phi}{\partial n} = f_3(x, y, z)$$

The physical boundary conditions that are commonly observed in the fluid problems are as follows:

- (a) Solid walls: Many boundaries within a fluid flow domain will be solid walls, and these can be either stationary or moving walls. When the flow is laminar then the velocity components can be set to be the velocity of the wall.
- (b) Inlets: At an inlet, fluid enters the domain and, therefore, its fluid velocity or pressure, or the mass flow rate may be known.
- (c) Symmetry boundaries: When the flow is symmetrical about some plane there is no flow through the boundary and the derivatives of the variables normal to the boundary are zero.
- (d) Cyclic or periodic boundaries: These boundaries come in pairs and are used to specify that the flow has the same values of the variables at equivalent positions on both of the boundaries.
- (e) Pressure boundary conditions: The ability to specify a pressure condition at one or more boundaries of a computational region is an important and useful computational tool.

(f) Outflow boundary conditions: In many simulations, there is a need to have fluid flow out of one or more boundaries of the computational region.

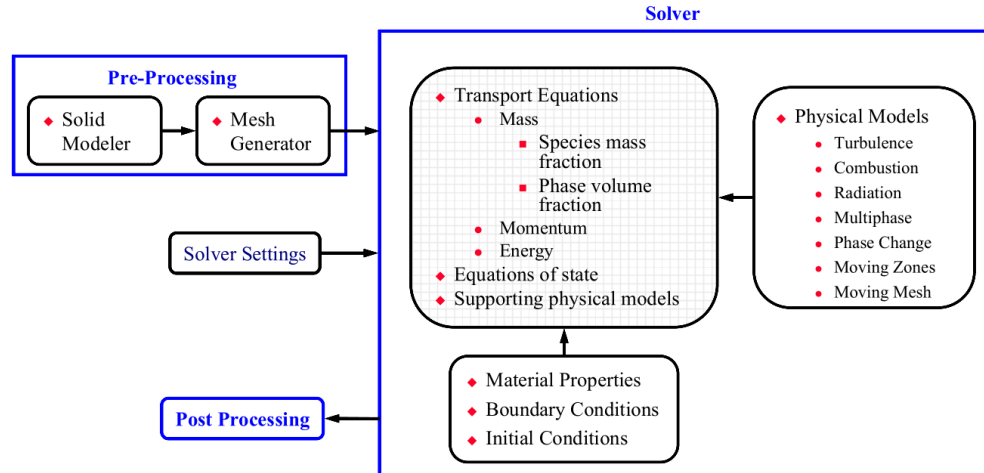
(g) Opening boundary conditions: When the fluid flow crosses the boundary surface in either direction an opening boundary condition needs to be utilized.

(h) Free surfaces and interfaces: When the fluid has a free surface, then the surface tension forces need to be considered. This requires utilization of the Laplace's equation which specifies the surface tension-induced jump in the normal stress  $p_s$  across the interface:

$$p_s = \sigma k$$

where  $\sigma$  represents the liquid-air surface tension and  $\kappa$  the total curvature of the interface.

### 3.1.2 CFD modeling



**Figure 3-2** CFD modeling.

All CFD codes contain three main elements: (1) A pre-processor, before simulating the problem geometry, generate the grid, and define the flow parameter and the boundary conditions to the code are input here. (2) A flow solver, there are four different methods used as a flow solver: finite difference method; finite element method, finite

volume method, and spectral method that are used in solving the governing equation of the flow subject. (3) A post-processor, after simulating the data and show the results are show in graphical and easy to read format.

### **3.1.2.1 Pre-processing**

Function of a pre-processor is to provide flow problem inputs to CFD program by means of a user-friendly interface and to convert the input provided in a form suitable to be used by the solver. At the stage of pre-processing following user activities are involved [4]:

- Defining computational domain i.e., geometry creation of the specific region of interest.
- Grid generation or meshing, by dividing the main computational domain into a number of smaller and non-overlapping sub-domains by means of a grid of cells. This yield small control volumes or elements.
- Selecting chemical and physical phenomena that are needed to be modeled.
- Defining fluid properties.
- Defining or specifying appropriate boundary conditions at the cells coinciding with domain boundary.

In CFD the solution of the flow problem is defined at nodes inside each cell. The accuracy of the solution depends on the number of cells in the grid. Generally speaking, solution will be more accurate for grids involving a larger number of cells. The accuracy of the solution along with the computational both largely depends on the grid fineness. To reduce computational cost without having an adverse impact on the accuracy of the solution



often non-uniform grids are used. These grids are finer in the regions where the variations are higher from point to point and coarser in the area where the variations are on a relatively lower side. To date no CFD commercial code is equipped with robust self-adapting meshing capabilities, although efforts are being made in this direction.

### **3.1.2.2 Solver**

After making mesh on the geometry, using a computer to solve mathematical equations of fluid flow. In the process the software can solve the equations of state for each cell until an acceptable convergence is achieved. Many thousands of equations are solved in a very intensive process. In each case, the equations are integrated and the boundary conditions are applied to it. The equation discretization is applied to each individual cell of the mesh. Until a required accuracy is achieved this process is repeated in an iterative manner. This step can be a time-consuming process depending on the core of any CFD software package.

### **3.1.2.3 Post processing**

This part includes three parts: 1) Visualization of numerical results via contour maps, vector fields and streamlines, 2) Integration of numerical results, 3) Validation of the CFD solution.

The post-processing program is used to make the evaluation of the data generated by the CFD analysis. When the model has been solved, the results can be analyzed both numerically and graphically. Post-processing tools of the powerful CFD software can create visualization ranging from simple 2-D graphs to 3-D representations. Typical graphs

obtained with the post-processor might contain a section of the mesh together with vector plots of the velocity field or contour plots of scalar variables such as pressure. In such graphs, colors are used to differentiate between the different size of the values. When some results have been obtained, they must be analyzed, first to check that the solution is satisfactory and then to determine the actual flow data that is required from the simulation. Commercially available CFD codes use different numerical solution techniques. For instance, CFD codes including ANSYS FLUENT, CFX, PHOENICS and STAR-CD make use of finite volume method to solve fluid flow problems. Generally, the numerical algorithm follows the following three steps: 1) Governing equations of fluid flow are integrated over all the finite control volumes of the domain. 2) The resulting integral equations are converted to a system of algebraic equations, this step is also referred to as discretization. 3) An iterative method is employed to solve the algebraic equations.

Most of the leading commercial CFD packages are equipped with powerful data visualization and export tools, for instance: 1) Display of domain geometry and grid. The facility for generating different surfaces in different areas of interest. 2) Plotting vectors at various surfaces of interest. 3) Contour plots. 4) Two-dimensional and three-dimensional surface plots. 5) Particle tracking. 6) Manipulate the view (rotate, translate, scale etc.). 7) Animation for dynamic result display. 8) Data export facility to analyze the generated data outside the code.

The reliability of the fluid flow problem results generated by the CFD codes depend on the proper embedment of physical laws. At beginning the model a flow problem in 2D or 3D is the important decisions that should be made, to include or exclude the effect

of ambient temperature, assume constant density for the working fluid or incorporate the effect of pressure variations on the fluid density etc. The appropriateness of assumptions made in the process partly determines the quality of the results generated by the code.

To have successful simulation results defining the appropriate domain geometry and optimal grid generation are also important tasks. The most of using criteria for successful results are convergence and grid independence. It has been established earlier that the solution of the fluid flow problem using CFD codes is iterative in nature, which means that for a converged solution the residuals is very small. This aim can be met by the appropriate selection of relaxation factors. The important part that should be considered is the grid independent solution can be obtained by successive refinement of an initial coarse grid to the point when the key results do not change with further grid refinement.

### **3.1.3 Literature on CFD application**

In membrane separation modeling, the topics using CFD to study include spacer geometry, fouling, and concentration polarization. Fouling on the membrane surface is an inevitable phenomenon in the separating process. Fouling modeling, specifically concentration polarization and temperature polarization, have been considered by CFD using many years [8–10]. The hydrodynamic in feed channel can be clarified by CFD directly, and the geometry of spacer is close related with flow pattern [11,12]. **Table 3-2** listed the important contribution through using 3D CFD.

**Table 3-2** Summaries of important contributions to membrane studies utilizing 3D CFD [13].

Karode and Kumar [24]	PHOENICS (commercial)	Various common commercial spacer meshes	Steady laminar, $Re_b = 225-2225$	None, only hydrodynamics	Early 3D CFD study of hydrodynamics and pressure losses in membrane units.	Questionable spatial resolution.	[14]
Li et al. [26]	CFX-4 (commercial)	3D channel with circular filaments, ladder type spacer	Laminar steady and unsteady, $Re_b = 90-465$	Periodic unit cell, impermeable wall with constant concentration	Attempts to find optimum spacer mesh geometrical characteristics; proposes power number ( $P_n$ ).	Does not describe implementation of periodic boundary condition for solute.	[15]
Li et al. [85]	CFX-4 (commercial)	3D channel with circular, twisted and modified filaments, multi-layer spacer	Laminar steady and unsteady, $Re_b = 90-850$	Periodic unit cell, impermeable wall with constant concentration	Proposes and tests optimal multi-layer spacer designs.	Questionable spatial resolution for multi-layer spacers may be one cause for over-prediction of mass transfer enhancement by CFD results.	[16]
Ranade and Kumar [25]	FLUENT (commercial)	3D flat and curved channel, circular, concave and modified filaments, ladder type at 45° angle of attack	Steady laminar and turbulent, $k-\epsilon$ turbulence model, $Re_b = 50-1500$	None, only hydrodynamics, periodic unit cell	Effect of curvature, quantifies form and viscous drag, tests alternative filament designs.	Unclear implementation of periodicity condition; use of turbulence model for flow regime modeled is debatable.	[17]
Koutsou et al. [23]	FLUENT 6.2.16 (commercial)	3D channel with ladder type spacer at varying internal and attack angles	Unsteady laminar, $Re_b = 70-740$	None, only hydrodynamics, periodic unit cell	Effect of unsteady flow on wall shear rate and flow patterns.	Results using periodicity condition in transient simulations are only valid when time-averaged.	[18]
Koutsou et al. [54]	FLUENT 6.2.16 (commercial)	3D channel with ladder type spacer at varying internal and attack angles	Unsteady laminar, $Re_b = 70-740$	Fully developed concentration, impermeable wall with constant concentration.	Correlates Sherwood number to Reynolds number and spacer geometric parameters.	Validation of mass transport only qualitative, as different Schmidt numbers were used.	[19]
Santos et al. [86]	OpenFOAM (open source)	3D channel with rectangular filaments, ladder type spacer	Laminar steady and unsteady, $Re_b = 60-1000$	Developing concentration, impermeable wall with constant concentration	Effect of longitudinal filaments; proposes modified friction factor.	No mass transfer periodic wrapping; conditions not representative of whole membrane module.	[20]
Shakaib et al. [87]	FLUENT 6.2.16 (commercial)	3D channel with ladder type spacer at varying internal and attack angles	Laminar steady, $Re_b = 20-200$	None, only hydrodynamics, periodic unit cell	Analysis of wall shear patterns at low $Re$ , effect of mesh length $l_m$ , and determination of critical $Re$ at which flow becomes unsteady.	Modeled multiple unit cells in fluid domain, thus increasing computational demand without increase in relevant data.	[21]
Fimbres-Weihs and Wiley [7]	ANSYS CFX-10.0 (commercial)	3D channel with circular filaments, ladder type at 90° and 45° angle of attack	Laminar steady, $Re_b = 10-500$	Fully developed concentration, impermeable wall with constant concentration.	Effects of form and viscous drag on mass transfer; analysis of connection between 3D steady flow features and mass transfer enhancement.	Describes periodicity condition for solute transport in 3D. Study restricted to laminar steady flow regime.	[22]
Lau et al. [55]	FLUENT 6 (commercial)	3D channel with circular filaments, ladder type spacer at varying internal and attack angles	Laminar steady and unsteady, $Re_b = 331-1160$	Periodic unit cell with developing concentration, permeable wall	Uses permeable wall boundary condition in 3D. Attempts to find optimum ladder type spacer mesh geometrical characteristics.	Questionable periodicity boundary conditions, in particular velocity profiles.	[23]

### 3.2 CFD protocol

In the last few years, there has been continuous progress in the development of CFD codes. These codes can now cope with a high level of complexity in many research fields, which makes them attractive to use. However, CFD codes that are used in the membrane separation have not reached a relatively mature state, they still require to be improved in accuracy, ease of use, robustness and computational efficiency [13]. Of all the commercial CFD codes there are some codes for general purpose as well as for specific applications. Most of these commercial CFD codes can be supported on the platforms of UNIX on workstations and WINDOWS or LINUX on high-end Intel Pentium PCs. **Table 3-3** summarized the main commercial CFD codes. Some of the common commercial codes are described as follows.

**Table 3-3** Commercial CFD code list.

<b>CFD code</b>	<b>Company</b>	<b>Web site</b>
CFX	ANSYS	<a href="https://www.ansys.com/products/fluids/ansys-cfx">https://www.ansys.com/products/fluids/ansys-cfx</a>
FLUENT	ANSYS	<a href="https://www.ansys.com/products/fluids/ansys-fluent">https://www.ansys.com/products/fluids/ansys-fluent</a>
OpenFOAM	OpenCFD Ltd	<a href="https://www.openfoam.com/">https://www.openfoam.com/</a>
Matlab	MathWorks	<a href="https://uk.mathworks.com/products/matlab.html">https://uk.mathworks.com/products/matlab.html</a>
COMSOL	COMSOL Multiphysics	<a href="https://uk.mathworks.com/products/matlab.html">https://uk.mathworks.com/products/matlab.html</a>
PHOENIX	Phoenix Software International, Inc.	<a href="http://www.cham.co.uk/">http://www.cham.co.uk/</a>

### 3.2.1 The finite difference method

The finite difference method was among the first methods applied to the numerical solution of differential equations [24]. It was first utilized by Euler, probably in 1768. The finite difference method is directly applied to the differential form of the governing equations. The principle is to employ a Taylor series expansion for the discretization of the derivatives of the flow variables.

An important advantage of the finite difference methodology is its simplicity. Another advantage is the possibility to easily obtain high-order approximations, and hence to achieve high-order accuracy of the spatial discretization. On the other hand, because the method requires a structured grid, the range of application is clearly restricted. Furthermore, the finite difference method cannot be directly applied in body-fitted (curvilinear) coordinates, but the governing equations have to be first transformed into a Cartesian coordinate system or in other cords from the physical to the computational space. The problem herewith is that the Jacobian of coordinate transformation appears in the flow equations. This Jacobian has to be consistently discretized in order to avoid the introduction of additional numerical errors. Thus, the finite difference method can be applied only to rather simple geometries. Nowadays, it is sometimes utilized for the direct numerical

simulation of turbulence (DNS), but it is only very rarely used for industrial applications. More details to the finite difference method can be found for example in [41], or in textbooks on the solution of partial differential equations.

### **3.2.2 The finite volume method**

The finite volume method directly utilizes the conservation laws - the integral formulation of the Navier-Stokes/Euler equations [24]. It was first employed by McDonald 1421 for the simulation of 2D inviscid flows. The finite volume method discretizes the governing equations by first dividing the physical space into a number of arbitrary polyhedral control volumes.

The main advantage of the finite volume method is that the spatial discretization is carried out directly in the physical space. Thus, there are no problems with any transformation between coordinate systems, like in the case of the finite difference method. Compared to the finite differences, one further advantage of the finite volume method is that it is very flexible, it can be rather easily implemented on structure as well as on unstructured grids. This renders the finite volume method particularly suitable for the treatment of flows in complex geometries.

It is interesting to note that under certain conditions, the finite volume method can be shown to be equivalent to the finite difference method, or to a low-order finite element method.

### **3.2.3 The finite element method**

The finite element method was originally employed for structural analysis only [24]. It was first introduced by Turner et al. [43] in 1956. About ten years later, researchers started to use the finite element method also for the numerical solution of field equations in continuous media. However, only with the beginning of the 1990s, did the finite element method gain popularity in the solution of the Euler and the Navier-Stokes equations. A good introduction to the classical finite element methodology can be found in [44]. Applications to flow problems are described in [45], [46], and more recently in [47].

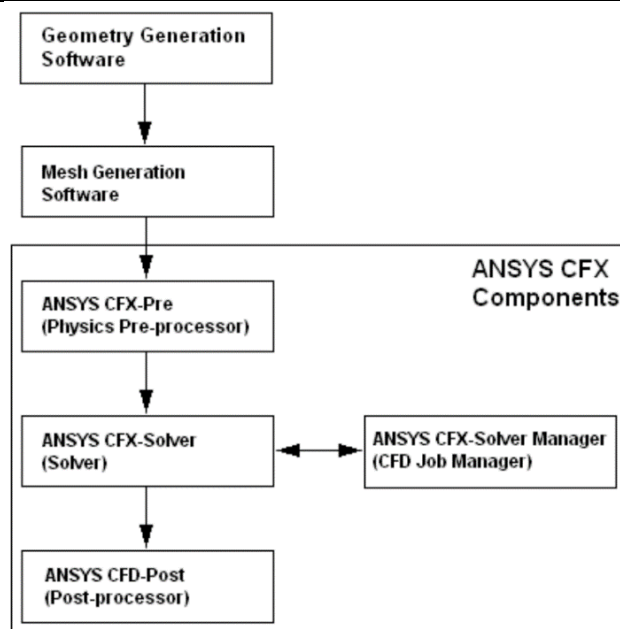
The finite element method, as it is in general applied to the solution of the Euler/Navier-Stokes equations, starts with a subdivision of the physical space into triangular (in 2D) or into tetrahedral (in 3D) elements. Thus, an unstructured grid has to be generated. Depending on the element type and the required accuracy, a certain number of points at the boundaries and/or inside an element is specified, where the solution of the flow problem has to be found. The total number of points multiplied with the number of unknowns determines the number of degrees of freedom. Furthermore, the so-called shape functions have to be defined, which represent the variation of the solution inside an element. In practical implementations, linear elements are usually employed, which use the grid nodes exclusively. The shape functions are then linear distributions, whose value is zero outside the corresponding element. This results in a second-order accurate representation of the solution on smooth grids.

From above the comparison of the three methods was listed in **Table 3-4**. The application of the Finite Volume Method for the solution of the Navier-Stokes equations

used in this study as employed by ANSYS CFX [ANSYS CFX, Release 18.1.] is described in the following sections. The structure of ANSYS CFX was shown in **Figure 3-3**.

**Table 3-4** Summary of characteristics of discretization methods [25].

Method	Formulation consideration	Mesh consideration	Boundary condition consideration
FDM	Conceptually easy to formulate	Meshes must be structured in two or three dimensions. Curvilinear meshes must be transformed to structured Cartesian coordinates. More difficult to accommodate complex geometries.	Neumann boundary conditions (derivatives of variables specified at boundaries) cannot be strictly enforced, only approximated.
FEM	Formulation less straight forward	Easier to accommodate complex geometries. Non-Cartesian coordinates and unstructured meshes possible	Neumann boundary conditions are exactly enforced
FVM	Can be formulated based on FEM or FDM	Depends on formulation (FEM or FDM)	Neumann boundary conditions are exactly enforced



**Figure 3-3** ANSYS CFX structure.

### 3.2.3.1 ANSYS CFX-Pre



The next-generation physics pre-processor, CFX-Pre, is used to define simulations. Multiple meshes may be imported, allowing each section of complex geometries to use the most appropriate mesh. Analyses, which consist of flow physics, boundary conditions, initial values, and solver parameters, are also specified. A full range of boundary conditions, including inlets, outlets and openings, together with boundary conditions for heat transfer models and periodicity, are all available in ANSYS CFX through CFX-Pre.

### **3.2.3.2 ANS'S CFX-Solver**

CFX-Solver solves all the solution variables for the simulation for the problem specification generated in CFX-Pre. One of the most important features of ANSYS CFX is its use of a coupled solver, in which all the hydrodynamic equations are solved as a single system. The coupled solver is faster than the traditionally segregated solver and fewer iterations are required to obtain a converged flow solution.

### **3.2.3.3 ANS'S CFX-post**

CFD-Post provides state-of-the-art interactive post-processing graphics tools to analyze and present the ANSYS CFX simulation results.

Important features include:

- 1) Quantitative post-processing
- 2) Report generation
- 3) Command line, session file, or state file input
- 4) User-defined variables

- 5) Generation of a variety of graphical objects where visibility, transparency, color, and line/face rendering can be controlled
- 6) Power Syntax to allow fully programmable session files.

### **3.3 Programming procedure**

In the thesis mainly CFX-pre 18.1 is used as a pre-processor and CFX-solver Manager 18.1 is used as a solver. After making the physical model in ANSYS Workbench including creating the mesh file, boundary conditions were defined in CFX-pre 18.1. The parameters and equations were together all the information provided to the CFX-solver 18.1 pertaining to a specific fluid flow problem. All the calculation performed by CFX-solver 18.1 gives out the results and are detailed in CFX-post 18.1.

The results of this thesis were generated by ANSYS CFX 18.1 and compared with the experimental and numerical studies which focused on commercial spacers. Since the geometries of the two spacers considered in the numerical studies are identical to those spacers considered in previous studies, therefore quantitative comparison of their results showed the inclination of the results matching. Furthermore, the characteristics of two spacers were detailed. Among the variables considered for comparison, pressure drop, wall shear stresses on membrane surfaces, Power number, friction factor, and modified friction factor coefficient.

## Reference

1. Branscomb, L.; Belytschko, T.; Bridenbaugh, P. From Desktop To Teraflop: Exploiting the U.S. Lead in High Performance Computing Available online: [https://scholar.google.co.jp/scholar?hl=en&as\\_sdt=0%2C5&q=Computational+fluid+dynamics.+In%3A+From+Desktop+to+Teraflop%3A+Exploiting+the+US+Lead+in+High+Performance+Computing&btnG=](https://scholar.google.co.jp/scholar?hl=en&as_sdt=0%2C5&q=Computational+fluid+dynamics.+In%3A+From+Desktop+to+Teraflop%3A+Exploiting+the+US+Lead+in+High+Performance+Computing&btnG=) (accessed on Nov 22, 2018).
2. Moin, P.; Kim, J. Tackling turbulence with supercomputers. *Sci. Am.* **1997**, *276*, 62–68, doi:10.1038/scientificamerican0197-62.
3. Xia, B.; Sun, D. W. Applications of computational fluid dynamics (CFD) in the food industry: A review. *Comput. Electron. Agric.* **2002**, *34*, 5–24.
4. Versteeg, H.; Malalasekera, W. *An introduction to computational fluid dynamics: the finite volume method*; 2007;
5. Shakaib, M.; Hasani, S. M. F.; Ahmed, I.; Yunus, R. M. A CFD study on the effect of spacer orientation on temperature polarization in membrane distillation modules. *Desalination* **2012**, *284*, 332–340, doi:10.1016/j.desal.2011.09.020.
6. Young, T. H.; Chen, L. W. Pore formation mechanism of membranes from phase inversion process. *Desalination* **1995**, *103*, 233–247, doi:10.1016/0011-9164(95)00076-3.
7. Häyrynen, K.; Langwaldt, J.; Pongrácz, E.; Väisänen, V.; Mänttari, M.; Keiski, R. L. Separation of nutrients from mine water by reverse osmosis for subsequent biological treatment. *Miner. Eng.* **2008**, *21*, 2–9, doi:10.1016/j.mineng.2007.06.003.
8. Hamdache, A.; Belkacem, M. Effects of a zero normal-concentration-gradient

- outflow boundary condition on concentration polarization in a CFD study of a reverse osmosis process. *J. Brazilian Soc. Mech. Sci. Eng.* **2018**, *40*, 507, doi:10.1007/s40430-018-1430-z.
9. Li, F.; Meindersma, W.; De Haan, A. B.; Reith, T. Experimental validation of CFD mass transfer simulations in flat channels with non-woven net spacers. *J. Memb. Sci.* **2004**, *232*, 19–30, doi:10.1016/j.memsci.2003.11.015.
  10. Hasani, S. M. F.; Shakaib, M.; Mahmood, M. CFD modeling of unsteady fluid flow and mass transfer in spacer-filled membrane modules. *Desalin. Water Treat.* **2009**, *9*, 211–220, doi:10.5004/dwt.2009.778.
  11. Gurreri, L.; Tamburini, A.; Cipollina, A.; Micale, G. CFD analysis of the fluid flow behavior in a reverse electrodialysis stack. *Desalin. Water Treat.* **2012**, *48*, 390–403, doi:10.1080/19443994.2012.705966.
  12. Koutsou, C.; Karabelas, A.; Kostoglou, M. Fluid Dynamics and Mass Transfer in Spacer-Filled Membrane Channels: Effect of Uniform Channel-Gap Reduction Due to Fouling. *Fluids* **2018**, *3*, 12, doi:10.3390/fluids3010012.
  13. Fimbres-Weihs, G. A.; Wiley, D. E. Review of 3D CFD modeling of flow and mass transfer in narrow spacer-filled channels in membrane modules. *Chem. Eng. Process. Process Intensif.* **2010**, *49*, 759–781, doi:10.1016/j.cep.2010.01.007.
  14. Sandeep, K.; Karode, S. K.; Kumar, A. Flow visualization through spacer filled channels by computational fluid dynamics I. Pressure drop and shear rate calculations for flat sheet geometry. *J. Memb. Sci.* **2001**, *193*, 69–84, doi:10.1016/S0376-7388(01)00494-X.

15. Li, F.; Meindersma, W.; De Haan, A. B.; Reith, T. Optimization of commercial net spacers in spiral wound membrane modules. *J. Memb. Sci.* **2002**, *208*, 289–302, doi:10.1016/S0376-7388(02)00307-1.
16. Li, F.; Meindersma, W.; De Haan, A. B.; Reith, T. Novel spacers for mass transfer enhancement in membrane separations. *J. Memb. Sci.* **2005**, *253*, 1–12, doi:10.1016/j.memsci.2004.12.019.
17. Ranade, V. V.; Kumar, A. Fluid dynamics of spacer filled rectangular and curvilinear channels. *J. Memb. Sci.* **2006**, *271*, 1–15, doi:10.1016/j.memsci.2005.07.013.
18. Koutsou, C. P.; Yiantsios, S. G.; Karabelas, A. J. Direct numerical simulation of flow in spacer-filled channels: Effect of spacer geometrical characteristics. *J. Memb. Sci.* **2007**, *291*, 53–69, doi:10.1016/j.memsci.2006.12.032.
19. Koutsou, C. P.; Yiantsios, S. G.; Karabelas, A. J. A numerical and experimental study of mass transfer in spacer-filled channels: Effects of spacer geometrical characteristics and Schmidt number. *J. Memb. Sci.* **2009**, *326*, 234–251, doi:10.1016/j.memsci.2008.10.007.
20. Santos, J. L. C.; Geraldés, V.; Velizarov, S.; Crespo, J. G. Investigation of flow patterns and mass transfer in membrane module channels filled with flow-aligned spacers using computational fluid dynamics (CFD). *J. Memb. Sci.* **2007**, *305*, 103–117, doi:10.1016/j.memsci.2007.07.036.
21. Shakaib, M.; Hasani, S. M. F.; Mahmood, M. Study on the effects of spacer geometry in membrane feed channels using three-dimensional computational flow

- modeling. *J. Memb. Sci.* **2007**, *297*, 74–89, doi:10.1016/j.memsci.2007.03.010.
22. Fimbres-Weihs, G. A.; Wiley, D. E. Numerical study of mass transfer in three-dimensional spacer-filled narrow channels with steady flow. *J. Memb. Sci.* **2007**, *306*, 228–243, doi:10.1016/j.memsci.2007.08.043.
23. Lau, K. K.; Abu Bakar, M. Z.; Ahmad, A. L.; Murugesan, T. Feed spacer mesh angle: 3D modeling, simulation and optimization based on unsteady hydrodynamic in spiral wound membrane channel. *J. Memb. Sci.* **2009**, *343*, 16–33, doi:10.1542/peds.2006-2759.
24. Versteeg, H. H. .; Malalasekera, W. *An introduction to computational fluid dynamics*; 2007; Vol. M; ISBN 9780131274983.
25. Keir, G.; Jegatheesan, V. A review of computational fluid dynamics applications in pressure-driven membrane filtration. *Rev. Environ. Sci. Biotechnol.* **2014**, *13*, 183–201, doi:10.1007/s11157-013-9327-x.

## **Pillar-like spacer**

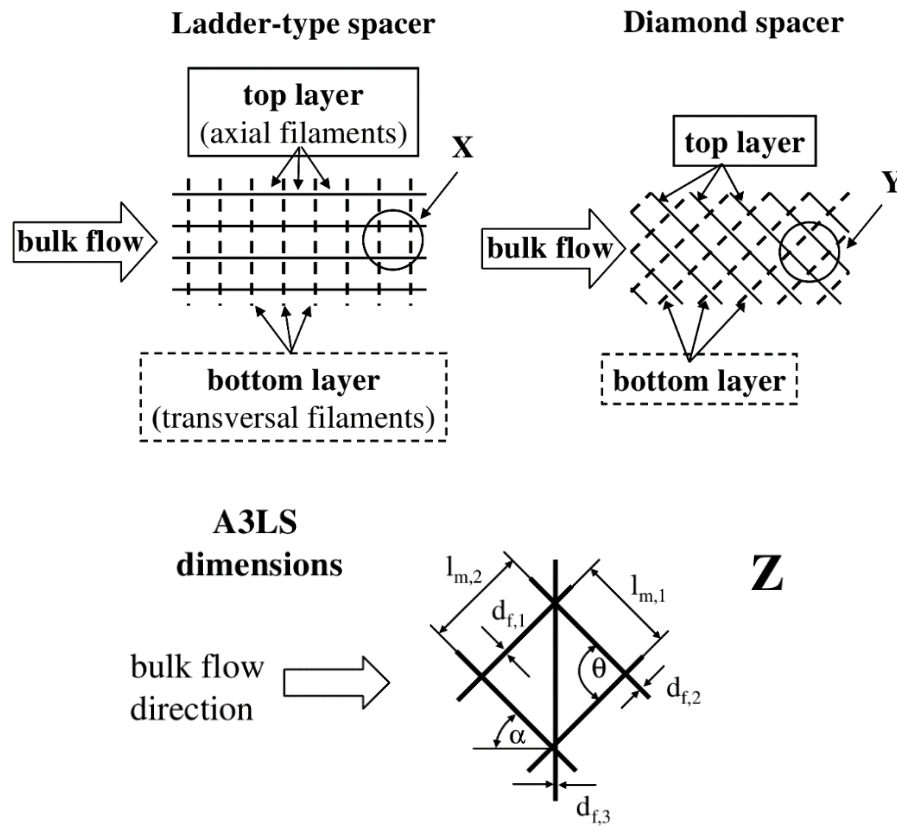
*This chapter shows the importance of flow situations to mass transfer in feed channel of spiral wound module. A novel spacer design is given out, and property of the spacer is discussed by using CFD simulation. The results of energy consumption and shear stress are compared with the commercial spacer.*

### **4.1 Introduction**

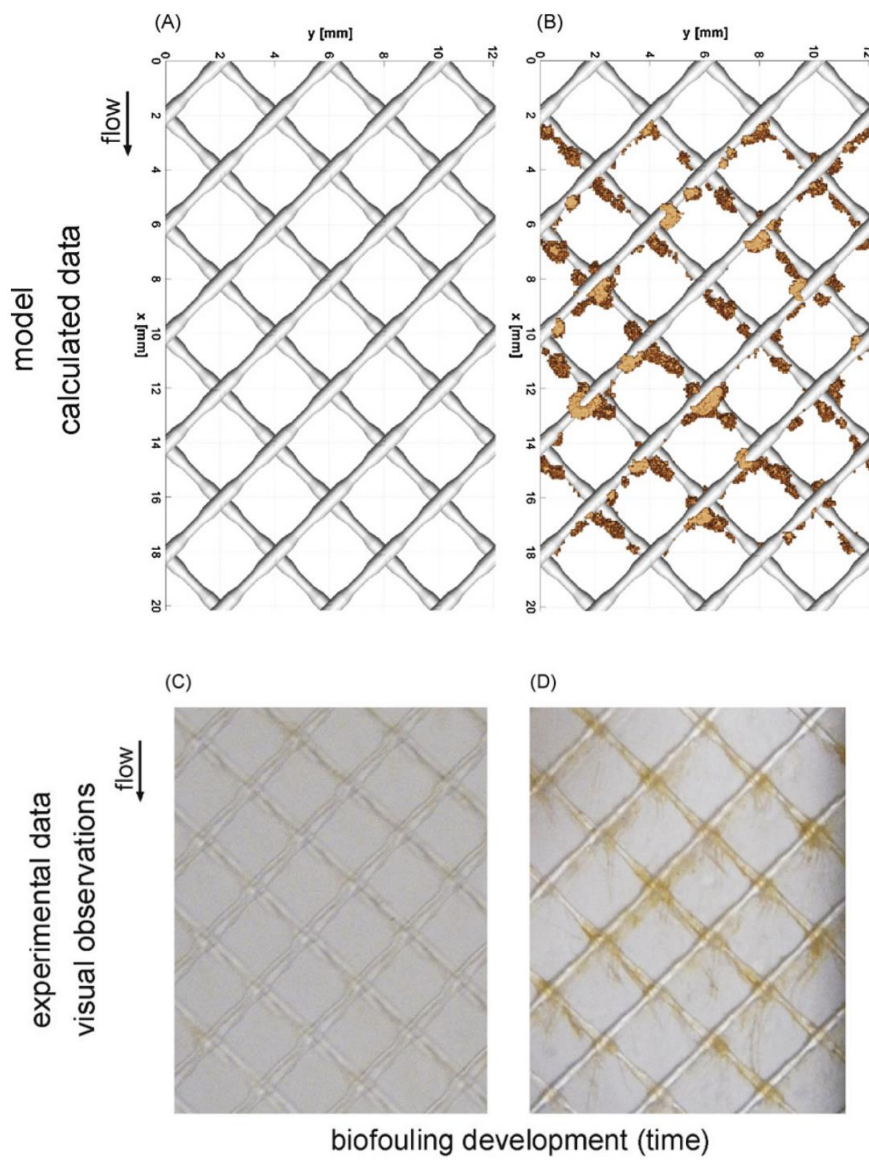
In the reverse osmosis (RO) process, membrane fouling occurs because the solute separation process is a significant challenge to reliable membrane performance. In addition to the membrane wall flow pattern, the solute separation process is vital to the feed spacer's design. To enhance the mass transport characteristics and to mitigate fouling and concentration polarization phenomena, different feed spacer geometries have been considered for the optimization of hydrodynamic characteristics in several numerical and experimental studies [1–3]. Schwinge et al. [4] reported, in detail, the effects of feed spacer geometry on the flux and pressure loss. Compared to other factors, previous studies have focused on the effect of feed spacers on fouling and performance. Using a numerical model, the experimental results of Vrouwenvelder et al. [5] confirmed that feed spacer fouling was more important than membrane fouling. Karabelas et al. [6] focused on the feed spacers' compressive stress effect on the characteristics of spacer-filled membrane channels. The authors' work focused on the effect of compressive stresses from the net-type spacers on

the spiral wound module's operating parameters and on the overall performance of the RO process. In recent years, the use of three-dimensional (3D) print technology in feed spacer fabrication has also been applied to enhance the membrane module's design [7,8]. Owing to biofouling and particulate fouling, the fouling of feed spacers in the membrane elements was noted as a vital problem during the RO operation. Cornelissen et al. [9] showed strategies to reduce biofouling linked to feed spacers with periodic air/water flushing. Araujo et al. [10] found that a decrease in pressure due to biofouling was generated by an increase in the spacer thickness. Particle Image Velocimetry (PIV) was applied to visually investigate the flow patterns determined by the feed spacer; PIV is considered to be a non-invasive and high-resolution experimental method [11]. The pressure decrease along the channel and the flux improvement are closely related to the flow pattern, especially the eddy promotion from the feed spacer. Radu et al. [12] reported that substrates rejection due to concentration polarization increased with biofilm thickness, and that biofilm removal depended on the velocity variation and shear stress. To achieve further economic improvements to the operation, the consideration of flow pattern has led to the study of feed spacer geometry.

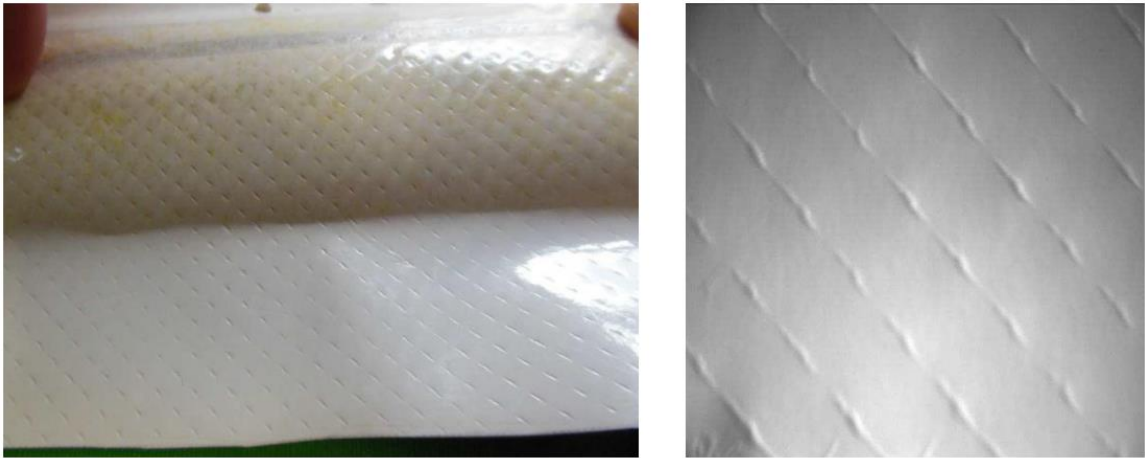




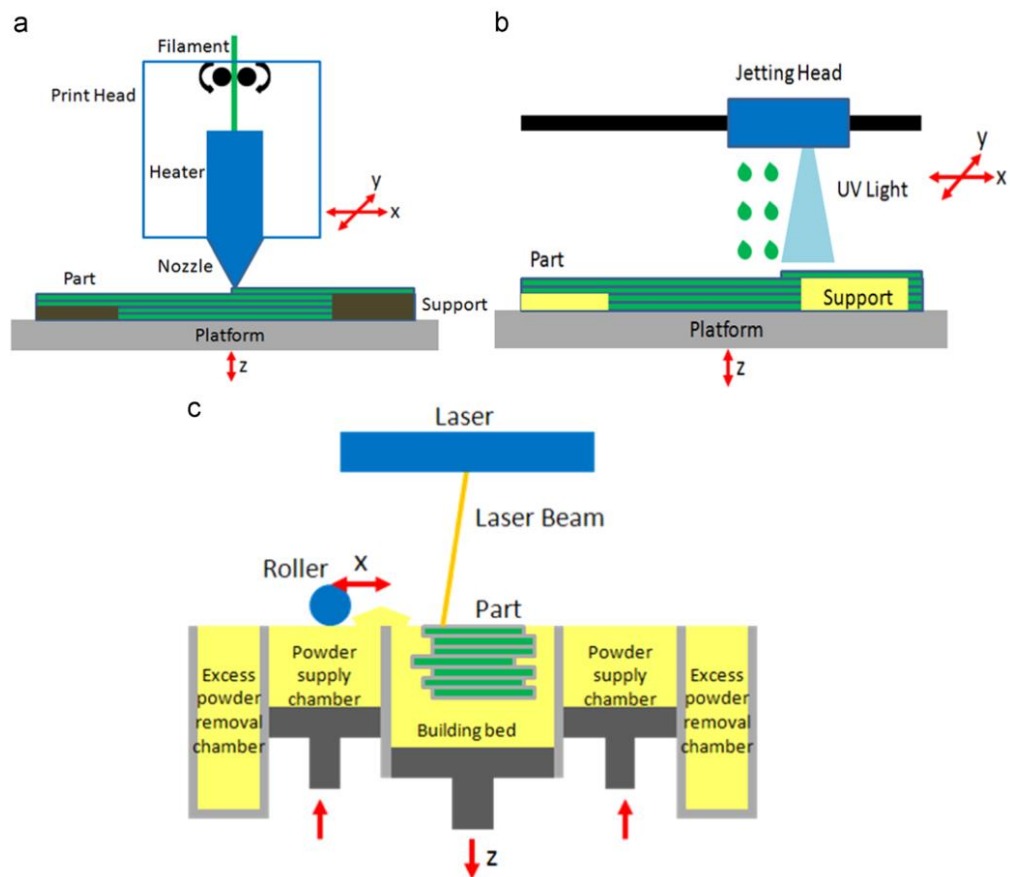
**Figure 4-1** 2 layer and 3 layer spacer reported by Schwinge et al. [4].



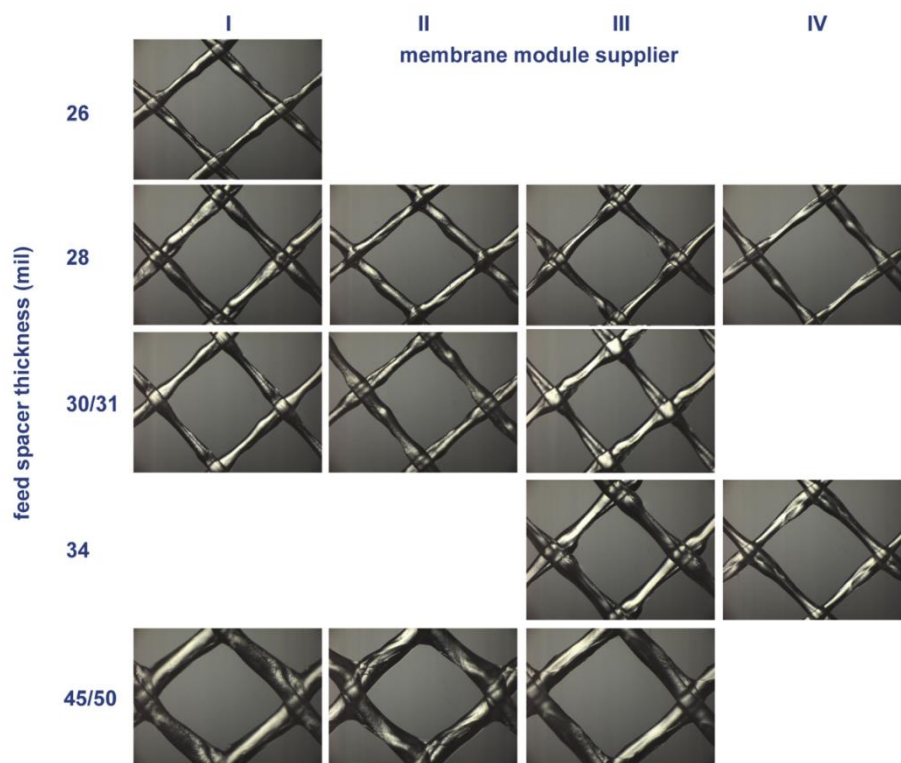
**Figure 4-2** Spacer fouling reported by Vrouwenvelder et al. [5].



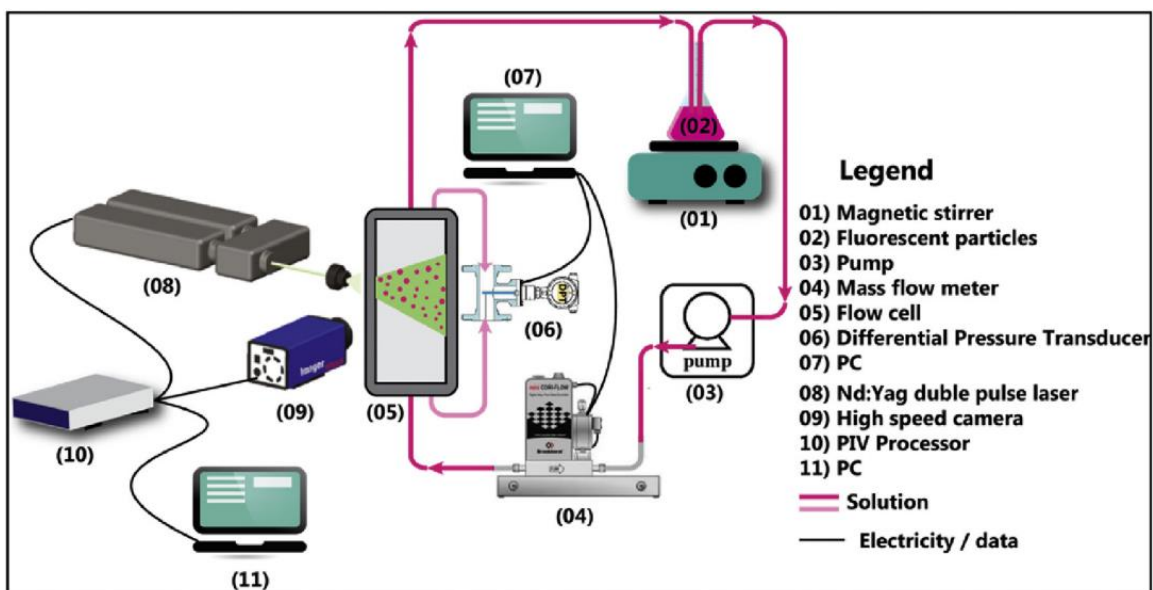
**Figure 4-3** Views of commercial RO membrane surfaces with indentations due to feed-spacer sheet compressed in-between envelopes reported by Karabelas et al. [6].



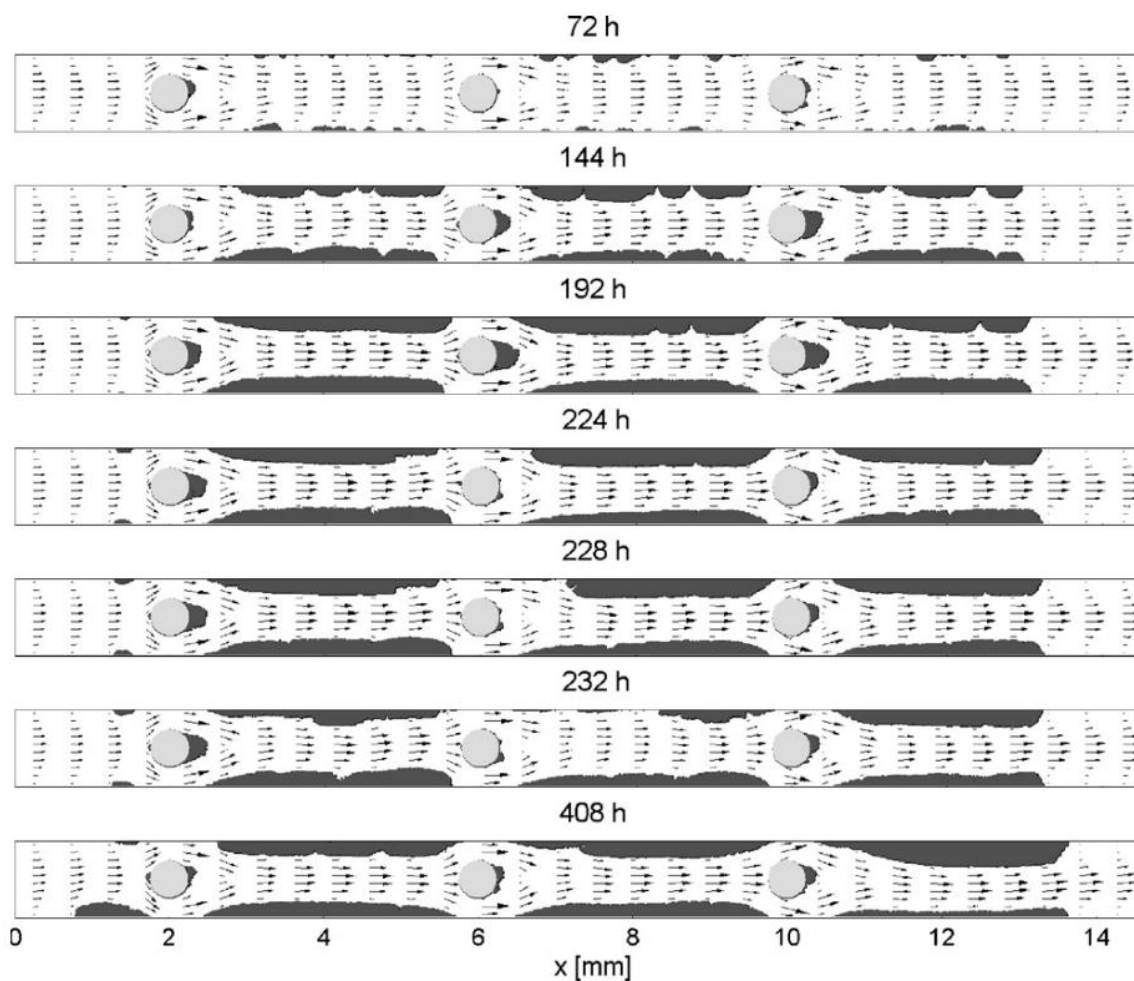
**Figure 4-4** Three representative 3D printing technologies [7].



**Figure 4-5** Images of standard feed spacers differing in thickness made with stereomicroscope at the same magnification factor reported by Araújo, P. A. et al.[10].



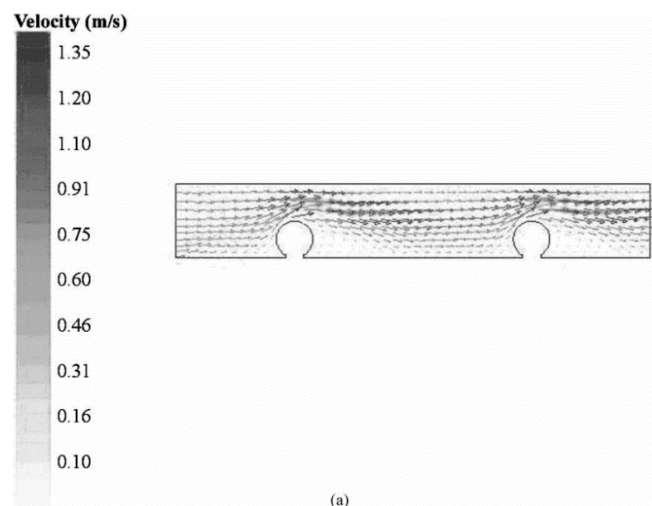
**Figure 4-6** PIV applying in spacer simulation [11].

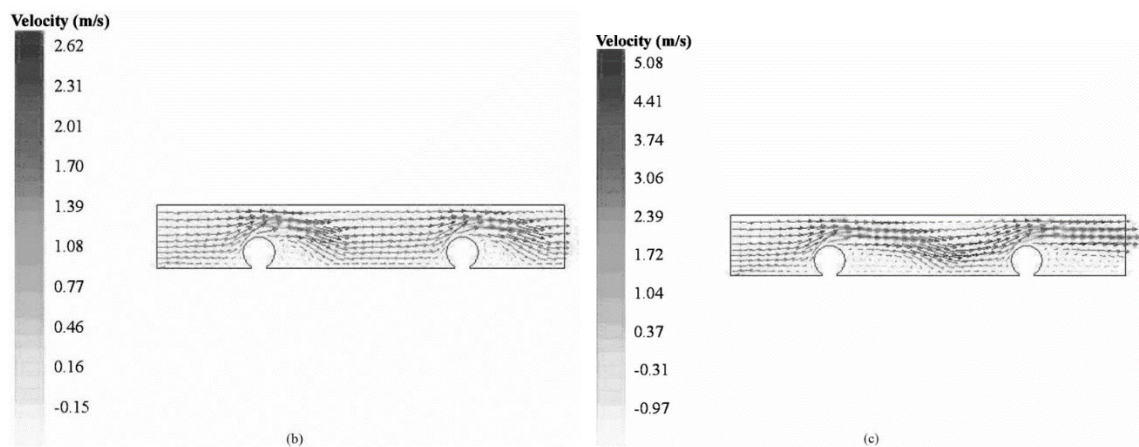


**Figure 4-7** Illustration of biofilm development in time in the feed channel with spacer reported by Radu, A. I. et al. [12].

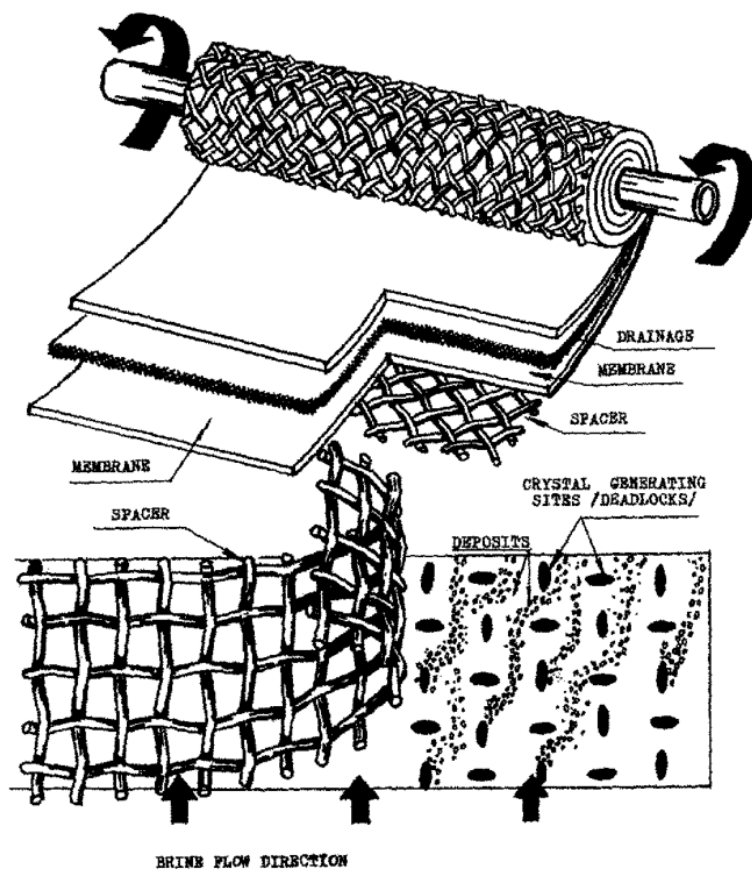
Extensive experimental and theoretical studies have sought a better understanding of spiral wound (SW) membrane mechanisms and the optimization of feed spacer geometric parameters. The studies have found the advantages of geometric configuration in the development of the feed spacer to promote high shear stresses and mass transfer rates. However, in the stagnant zone, which is behind the line contact filaments, a low flow

velocity means fewer shear stresses, lower mass transfer rates, and a quicker membrane flux decline, which are caused by a simultaneous increase in fouling [13]. In early work, Pervov et al. [14] pointed out the influence of the feed spacer on the scale formation process in the SW membrane model, and details of the mineral precipitation in the contact zone of the spacer and membrane were described in this work. It was found that the transverse filaments determined the flow structure, as reported by Da Costa et al. [15] and Santos et al. [16]. In the current study, a pillar-like spacer was designed to optimize feed spacer geometry. Compared with the conventional spacer, the contact method of the pillar-like spacer with the membrane changed with the area contact. Hence, it was possible that the diameter of the connecting filaments (transverse filament) had decreased to maximize the channel porosity. Furthermore, different cross-section of conjunction were considered shown in **Table 4-1**. To optimize the flow pattern near the membrane, different configuration of connecting filament were investigated shown in **Table 4-2**. The energy consumption and shear stress were analyzed using a numerical method, and the results were compared to those of commercial spacers studied in previous works.

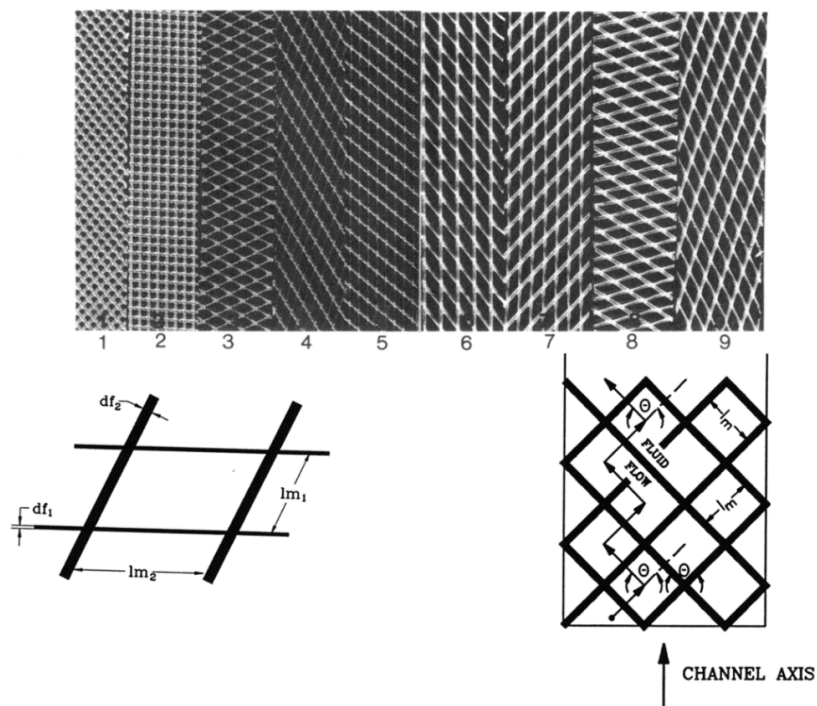




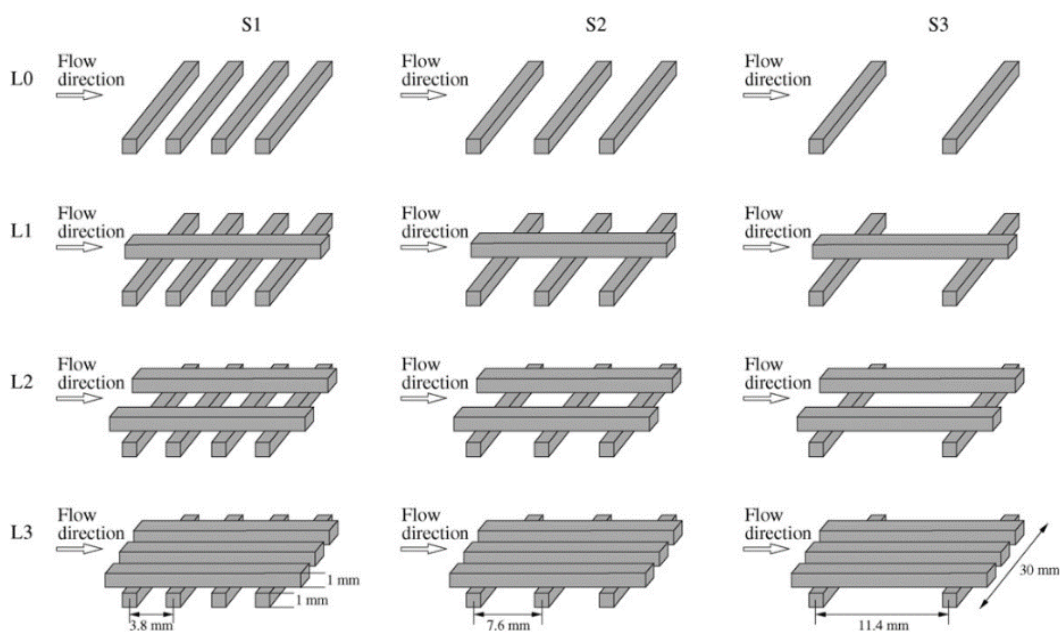
**Figure 4-8** Velocity vector distribution at velocity equal to (a) 0.5 m/s; (b) 1.0 m/s; (c) 2.0 m/s — two cylinders [17].



**Figure 4-9** The causes of scale formation in spiral wound RO modules reported by Pervov, Alexei G et al.[14].



**Figure 4-10** Commercial spacers reported by Da Costa et al. [15].





**Figure 4-11** Schematic of tested flow-aligned spacers in Santos et al. study [16].

## **4.2 Materials and Methods**

### **4.2.1 Characterization of the Pillar-Like Spacer**

#### **4.2.1.1 Feed Spacer Design-Related Problem**

Optimizing the feed spacer's design is the key way to improve SW membrane performance in a pressure-driven membrane process. In the feed channel, spacer use is essential to mass transfer; however, the feed spacer geometry determines the hydrodynamics at the same time. Changes in the flow direction and spacer filaments drag cause hydrodynamic resistance, which generates more power consumption in the membrane's operation. Compared to an empty channel, a spacer-filled channel has a higher pressure drop and 3–5 times more flux enhancement. However, beyond the critical Reynolds number of 60, the flow becomes unstable [18], notably when the cylinder is inserted in the middle of the channel. This is important to both the periodic and symmetric geometry in the feed spacer's design. The SW membrane parameter variables (i.e., the diameter of the filament, element size, channel height, channel porosity, etc.) influence the flow patterns linked to the shear stress distribution on the membrane and feed spacer surface. The hydrodynamic boundary layer must be considered for the permeate flux and fouling process in most of the hydrodynamic analysis.

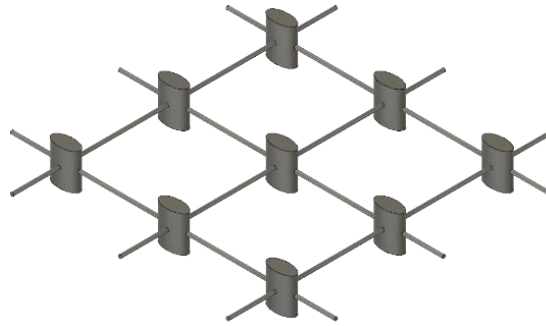
In conventional designs, the transverse filaments (perpendicular to the cross flow) of the woven and unwoven feed spacer are important to the phenomenon of concentration polarization, which is closely related to membrane fouling near to the membrane surface.

The region adjacent to the transverse filaments wall has much higher concentrations [19]. Boram et al. [20] compared the water flux in four classic types of feed spacer configurations, which included nonwoven, partially woven, middle-layer, and fully woven spacers, and showed concentration contours near the transverse filaments using COMSOL Multiphysics. Van Gauwbergen et al. [21] reported the same situation using potassium and calcium chloride as tracers in the experimental research. In the present design, transverse filaments were set as the submerged spacer, where the intersection of the filaments lowered the feed spacer effect owing to its cross-section design.

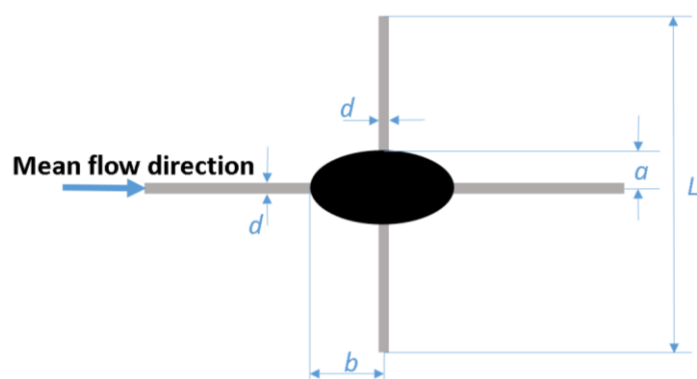
#### **4.2.1.2 Selection of Feed Spacer Design Parameter Values**

Typical net-like feed spacers are composed of woven and nonwoven feed spacers to enhance mass transfer in the membrane modules. Filaments contact the membrane with the line; so, in the downstream, there is a dead-flow zone behind the transverse filaments. In these dead-flow zones, velocity is close to zero, shear stress and mass transfer are low, and biofouling cultivates easily. The location and inter-filament distance of the feed spacers constrain the shear stress distribution, mass transfer coefficients, and the pressure inside the channel [17]. Koutsou et al. [22] designed a novel spacer to eliminate the adverse effects from the dead-flow zone. However, the nodes of the design were spherical and contacted the membrane with points, which was unstable and made it difficult to optimize the transverse filament. In the current study, a pillar-like spacer was designed, and it was composed of two sets of the intersection and the connecting filaments. A schematic diagram of the pillar-like feed spacer is illustrated in **Figure 4-12** (shown by an elliptic intersection) and **Figure 4-15**. The intersection that was perpendicular to the membrane

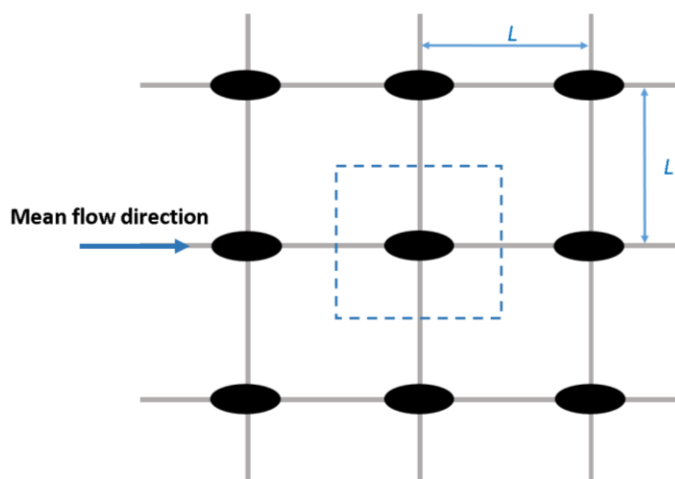
surface was fixed by the transverse and longitudinal connecting filaments. Furthermore, its cross-section was designed as ellipse and circular for comparison; hence, the intersection contacted the membrane with a small elliptic or circular area. The area contact was more stable than points or line contact. Additionally, the connecting filament was in the middle of the feed channel. The adverse effects on the dead-flow zone were eliminated. The geometry of this pillar-like feed spacer was described by the feed channel height,  $h_f$ , the element length (the distance between the filaments),  $\Delta L$ , the diameter of the connecting filament,  $d$ , the semi-major axis and semi-minor axis of the intersection elliptic cross-section,  $a$  and  $b$ , respectively (as shown in **Figure 4-13**), and the diameter of the intersection circular cross-section,  $D$  (shown in **Figure 4-15**). The feed spacer was also characterized by the hydraulic diameter,  $D_H$ , and the feed channel porosity or voidage,  $\varepsilon$ .



**Figure 4-12** A view of the morphology of the pillar-like feed spacer.










(a)



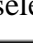

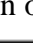

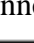

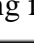

(b)

**Figure 4-13** The geometrical characteristics of the pillar-like feed spacer.

**Table 4-1** The selection of conjunction cross-section

Conjunction cross-section	Ratio	Fig
Ellipse	$b=2a$	
	$b=3a$	
Circle		
Drop	$b=a/2$	
	$b=a$	
	$b=2a$	
Hexagon		

**Table 4-2** The selection of connecting filament

Connecting filament cross-section	Fig	Major/Minor Diameter		Others	
		Major	Minor		
1			0.68/0.34	0.25	conjunction connecting
			0.5/0.25		connecting
2			0.68/0.34	0.25	conjunction connecting
			0.75/0.25		connecting
★ 3			0.68/0.34	0.25	conjunction connecting
			0.5/0.25		connecting
4			0.68/0.34	0.25	conjunction connecting
			0.75/0.25		connecting

The basic geometrical characteristics were the ratio of the distance between the parallel connecting filaments to the diameter of the cylinder intersection ( $L/D$ ) and the ratio of the diameter of the circular intersections to the diameter of the cylinder connecting filaments ( $D/d$ ), or the diameter of the cylinder connecting filaments to the ellipse semi-minor axis for the elliptic cross-section ( $d/a$ ), as shown on the right of **Figure 4-15**. The main flow direction was vertical to the cylinder connecting filaments, as shown in **Figure**

4-13. From a Computational Fluid Dynamics (CFD) viewpoint, it was convenient to define every simulated unit cell and simulate the respective flow field in detail. A higher pressure drop was caused by the feed spacer as reported by Haidari et al. [11]. The diameter of the cylinder connecting the filaments decreased to enhance the channel porosity. Lanxess AG (LXS-ASD) has done the same work, although it alternated the strand thickness to reduce the pressure drop [23]. Filament spacing is a key parameter for the pressure drop, mass transport, and fouling propensity [24,25]. In a commercial spacer, the ratio  $L/D$  usually varies between 7 and 9; however, in most studies, this ratio varies between 6 and 12 [26,27]. For consideration of the mechanical strength in this design, a high density was applied or a minor  $L/D$  ratio = 6 was applied. For area contact,  $D = h_f/2 = 1$  mm [4] was employed in the present parameters setting.

#### **4.2.2 Computational Model**

Along with the experimental techniques, the time, cost, and risks were reduced by the computational techniques. As a reliable and efficient numerical analysis tool, CFD has been extensively applied to the flow conditions of the SW membrane modules as described in Reference [28]. The interaction of the many different processes could be assessed through computational simulation. Without building spacers, CFD simulation can investigate hydrodynamics under various feed spacer geometry parameters. In the present work, the model of the pillar-like feed spacer was constructed to simulate a membrane system to analyze the role of the pillar-like feed spacer in the feed channel in terms of improving the hydraulic behavior and the decreasing pressure drop. In the current work, a

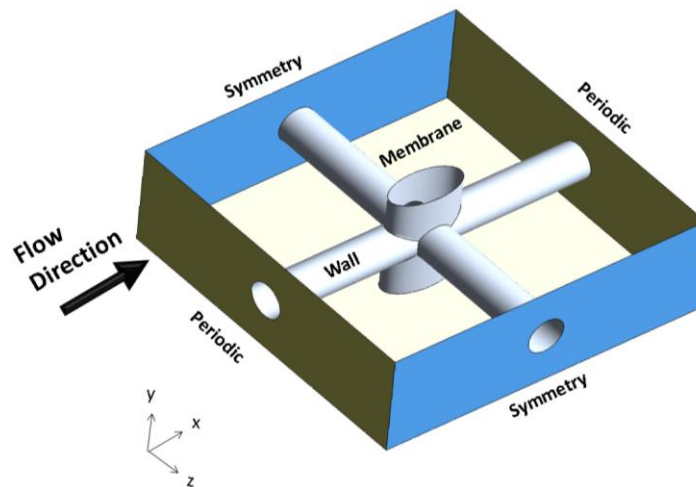
double-sided membrane was implemented, and the consideration of the feed spacer's impact was based on the fluid dynamics and also the through flow.

A 3D Computational Fluid Dynamics (CFD) model was constructed to study the impact of the pillar-like feed spacer in relation to hydraulics in the feed channel. There were two steps to the model. The geometry was constructed by comparison with conventional geometries. Therefore, the incompressible flow in the laminar flow regime was calculated using commonly employed parameters (i.e., friction factor, the dimensionless power number, and the modified friction factor).

#### **4.2.2.1 Model Construction**

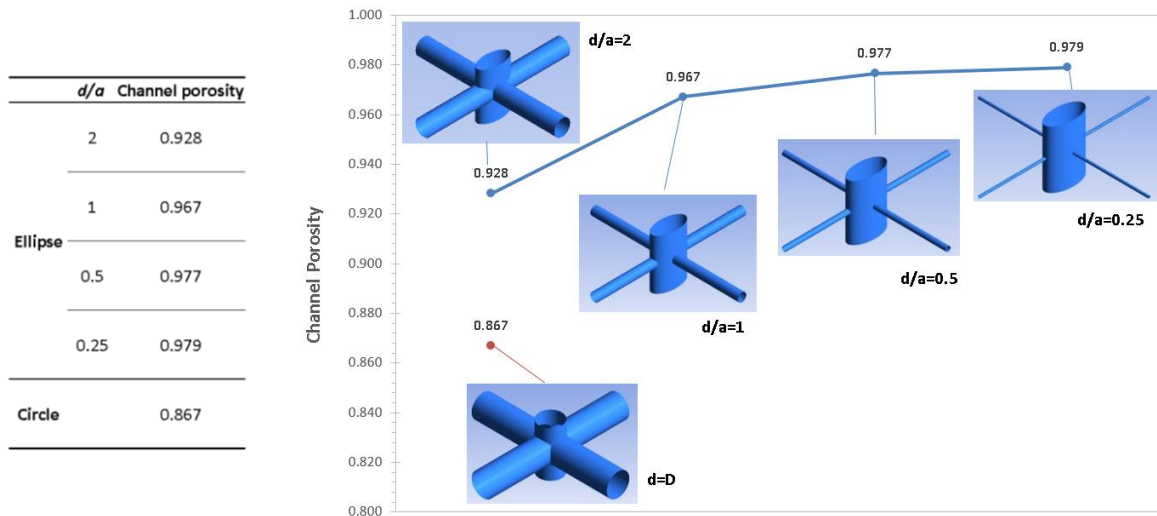
The middle region was chosen for the sake of simplicity as the study region (as shown in Figure 4-2). In most RO applications, the permeation velocity has no significant effect on the flow structure in the channel, and in industrial membrane processes, the permeate rate is no more than 0.5% of the total cross-flow velocity in the feed channel. For this reason, the membrane and feed spacer surface were set as a no-slip boundary condition and the assumption of a non-permeable wall was adopted; also, the velocity of the fluid on the surface was specified as zero in the CFD model. Thus, the spacer was explicitly defined as a solid object. The inlet and outlet cross-section were set as the periodic boundary as described in References [18,29]. The cross-section between two near elements was set as the symmetrical boundary as in Reference [30] (shown in **Figure 4-14**). The cylinder hydraulics diameter of the cross-section was fixed to compare the circle cross-section and the elliptic cross-section as outlined in Reference [31]. To enhance the porosity, the diameter of the connecting filament was decreased, and five kinds of geometry were

considered in this study (as shown in **Figure 4-15**). In most real cases, the flow through the spacer-filled modules falls in the Reynolds number category where the flow is steady and laminar [32]. The standard laminar model was applied following the literature recommendation to simulate flows below a Reynolds number of 300 in the laminar flow regime through the solution of continuity, as in Reference [33]. Given the simplified simulation, fluid was assumed to be Newtonian and incompressible, and, therefore, no salt source was considered.



**Figure 4-14** Computational Fluid Dynamics (CFD) model setting.





**Figure 4-15** The pillar-like feed spacer's porosity.

#### 4.2.2.2 Simulation of Flow Patterns

The flow of a Newtonian fluid in the spacer-filled channel was modelled by Navier–Stokes and continuity equations. The simulation equations are listed below:

The channel porosity is

$$\varepsilon = 1 - \frac{V_{Spacer}}{V_{Total}} \quad (2)$$

where  $V_{Spacer}$  is the feed spacer volume, and  $V_{Total}$  is the channel space volume in which the mean flow was separated. The hydraulic channel Reynolds number as in Reference [2] is

$$Re = \frac{\rho U_{ave} D_H}{\mu} \quad (3)$$

where  $\rho$  is the water density,  $U_{ave}$  is the average velocity that flows in the spacer-filled channel, where  $U_{ave}$  is calculated by dividing the superficial velocity (for the empty

channel) by the porosity, ( $U_{ave} = U_{sup}/\varepsilon$ ).  $\mu$  is the water kinematic viscosity. The definition of the Reynolds number was used in the results of friction factor and dimensionless power number. The channel hydraulic diameter, as a geometrical parameter that is dependent on the  $d/a$  ratio and is close to the filament drag, can be defined as in Reference [2]

$$D_H = \frac{4 \times \text{computational volume}}{\text{wet surface area}} \quad (4)$$

where the computational volume is the total volume of the element cell. Wet surface area was included in the surface of the spacer and the membrane. Pressure drop can be expressed via the friction factor described in References [34,35].

$$f = \frac{\Delta P}{\Delta L} \frac{2D_H}{\rho U_{ave}^2} \quad (5)$$

where  $\Delta p$  is the pressure drop in the channel and  $\Delta L$  is the element length.

The dimensionless power number outlined in References [27,36] is calculated as follows:

$$P_n = f R_e^3. \quad (6)$$

Shear stress on the membrane's surface is important to lower the concentration polarization and enhance the mass transfer. The modified friction factor employed to select the best feed spacer for mass transfer efficiency was used as the method to analyze shear stress on the membrane in comparing five group data as in Reference [16].

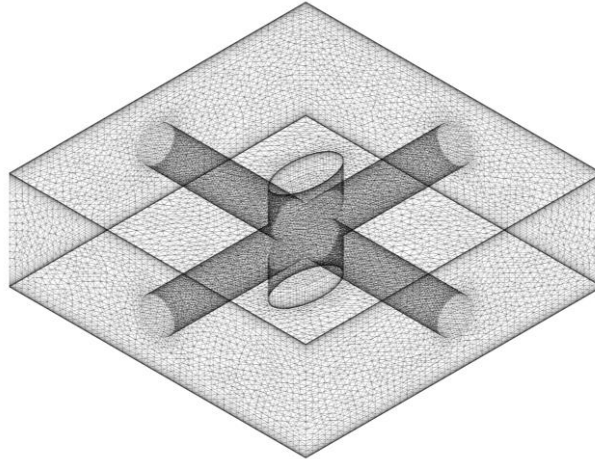
The modified friction factor for the area average shear stress is represented as in Reference [16]

$$f_{wall} = \tau_{wall} \frac{Re^2}{\rho U_{ave}^2} = \tau_{wall} \frac{\rho D_H^2}{\mu^2} \quad (7)$$

where  $\tau_{wall}$  is the average shear stress on the membrane surface. All other quantities in the equations are known and constant quantities.

#### 4.2.2.3 Model Solution

Navier–Stokes equations (REF) were solved in ANSYS-CFX (v18.1, ANSYS, Inc. Cecil Township, Pennsylvania, United States, [www.ansys.com](http://www.ansys.com)), with the finite volume method on the tetrahedral mesh (shown in **Figure 4-16**) being generated by the ANSYS-CFX automatic mesh generator. Tetrahedral elements were the main elements of the fluid simulation, where Haaksman et al. also generated the same kind of mesh in a simulation [23,28]. Picioreanu et al. [37] also used tetrahedral elements for the finite element solution in three-dimensional application modes. In **Figure 4-16**, the mesh quality of the boundary layer is illustrated. The grid sizes varied from 89,823 to 134,003 min nodes for the different channel porosities. The mesh was refined near the membrane surface of the boundary layer simulation, and the mesh was expanded away from the membrane. The near-wall node on the membrane was at a distance of 0.2 mm. The thickness of the first mesh element layer was below 1% of the channel height as in Reference [38]. The mesh independence of the solution was checked to ensure that there were sufficient cells in the boundary layer.



**Figure 4-16** The computational grid for the pillar-like feed spacer.

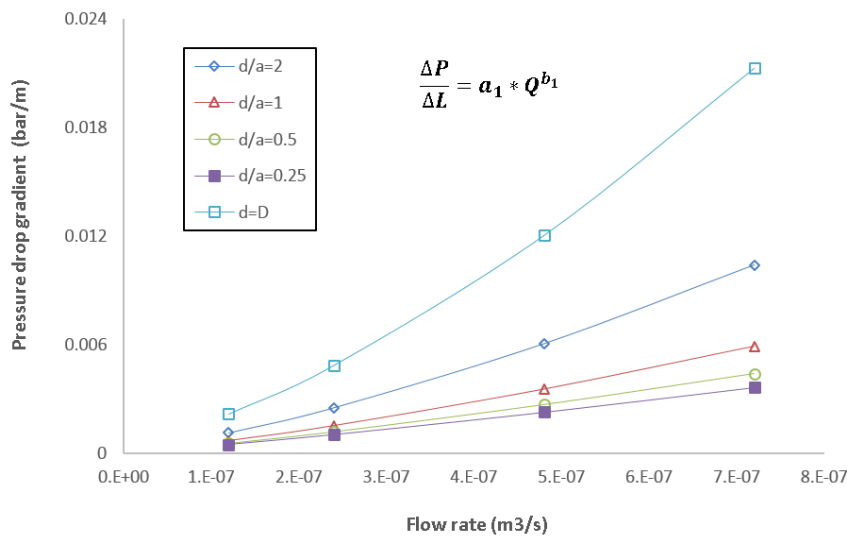
### 4.3 Results

Significant quantitative characteristics of the pillar-like feed spacer are presented herein. The results of this study were obtained from direct numerical simulation techniques. To investigate the flow pattern, water was taken as a bulk flow in this study. The Reynolds number up to 200 and the filament spacing 4 resulted in a moderate pressure drop and higher values of the mass transfer coefficient as reported by Asim Saeed et al. [35]. Ranade et al. [39] indicated that, in most of the spacer-filled channels, the transition from the laminar to turbulent flow regime occurred at Reynolds numbers of 300–400 for packed beds. In Shakaib et al. [40], the simulation for the onset of unsteady flow took Reynolds numbers from 100 to 300. Haaksman et al. [23] observed differences in the experiment and model results, where the Reynolds number was from 125 to 200. In the current study, four different flow rates were relayed with average inlet velocities of  $0.01 \text{ m s}^{-1}$ ,  $0.02 \text{ m s}^{-1}$ ,  $0.04 \text{ m s}^{-1}$ , and  $0.06 \text{ m s}^{-1}$ , yielding a Reynolds number ranging from 30 to 250 when running the CFD simulation. To validate the present work for simulating the character of

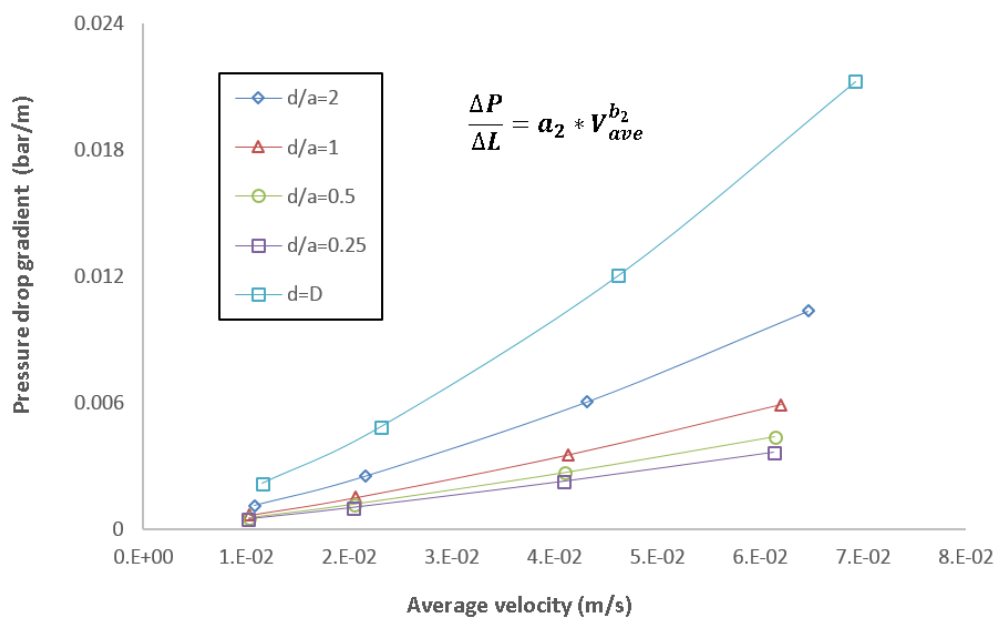
the pillar-like feed spacer, the results of the basic dimensionless parameters friction factor, the dimensionless power number, and the modified friction factor, which have been used in other studies, were compared with the results of previous studies on the empty channel and conventional spacers. From Equation (3), the Reynolds number depends on the hydraulic diameter, which is related to the filament surface defined by the ratio  $d/a$ . Therefore, the Reynolds number was selected by comparing the energy consumption. The comparison of the shear stress was performed by selecting the same energy consumption, where the dimensionless power number was equal to  $10^6$ , and commercial spacers were added to compare the inclination of the modified friction factor. Two types of commercial spacers were used (Conwed Plastics, Minneapolis USA), as mentioned in Haaksman et al. [23], for comparative purposes.

#### 4.3.1 Porosity

Channel porosity is the ratio of the empty volume to total volume. Channel porosity can be applied to estimate filament dimension and feed spacer mesh size. Feed spacer volume can be measured by the feed spacer weight or feed spacer density using the experimental method. However, the geometry parameters of the feed spacer have been measured using a microscope in most of the experimental studies [41]. The channel porosity can be calculated using Equation (2). In the present work, a different element length meant a different porosity of the feed channel, and the value was higher than in other feed spacer studies, where the maximum value of the porosity measurement was 0.906 as reported by Siddiqui et al. [42]. In this study, the porosity value of the elliptic cross-section was from 0.928 to 0.979, as shown in **Figure 4-15**.



(a)



(b)

**Figure 4-17** The pressure drop, associated with the connecting filament diameter, as a function of (a) the flow rate and (b) the average velocity.

**Table 4-3** The pressure drop function parameters.

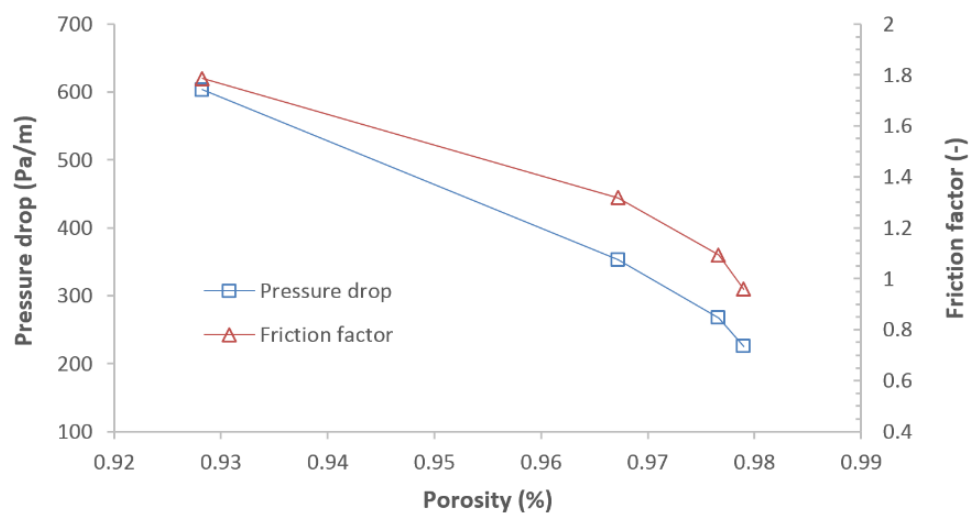
	$a_1$	$b_1$	$a_2$	$b_2$
$d/a = 0.25$	$3.26 \times 10^4$	1.13	0.09	1.13
$d/a = 0.5$	$6.45 \times 10^4$	1.17	0.11	1.17
$d/a = 1$	$1.59 \times 10^5$	1.21	0.17	1.21
$d/a = 2$	$4.62 \times 10^5$	1.25	0.31	1.25
$d = D$	$1.00 \times 10^6$	1.28	0.62	1.28
Haidar Spacer [11]	$1.77 \times 10^8$	1.63	7.91	1.63
Haidar Channel [11]	5384	0.97	0.23	0.97

The viscous drag on the feed channel walls and the feed spacer form the drag of the feed spacer, and the kinetic losses determine the pressure drop through directional flow change in a spacer-filled channel [43]. The average velocity influences the flow change, where Da Costa et al. [44] reported on the relationship between pressure and average velocity and gave the parameter “ $m$ ” result in the laminar and turbulent flow.

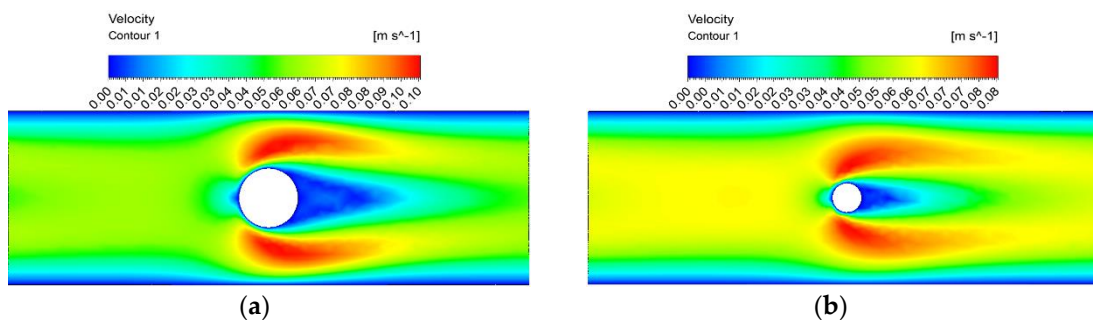
$$\Delta P \propto u^m \quad (8)$$

In this study, the pressure drop per unit of channel length, affected by the flow rate ( $Q = U_{super} \times h \times b$ ) and average velocity, increased as deduced in **Figure 4-17**. Haidari et al. compared the pressure drop in the spacer-filled and empty channels, and the results are listed in **Table 4-3** [11]. The changing inclinations of the pressure drop gradient were simulated in the results by Haidari et al. The equation parameter values were between the spacer-filled channel and the empty channel. The lower porosity was accelerated with the gradual increase of the pressure drop. In **Figure 4-18**, the inlet velocity was set at 0.04 m/s (a constant flow rate was selected to clarify the inclination of the pressure drop and friction factor), and the pressure drop decreased with the increase in porosity, and this inclination was in agreement with previous studies [42,43]. In comparison, the channel porosity increased by 5% and the pressure drop reduced by 62.56%. At a high channel porosity, the

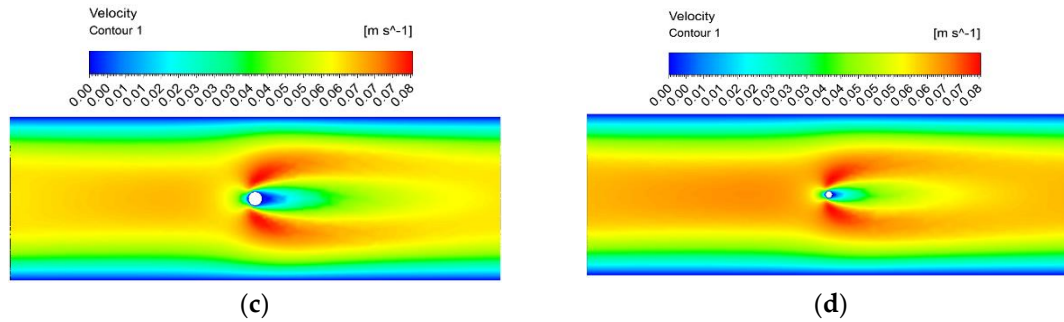
pressure drop approached that of the empty channel. As shown in **Figure 4-19**, a higher diameter of the connecting filament or a lower channel porosity generated a bigger shadow region behind the transverse filament. It is important to note that the friction had a closer relationship with the filament drag from the feed spacer than the surface of the membrane. Furthermore, the pressure drop depended on the friction in the middle of the channel. That was the reason for the decrease in the connecting filament diameter generated by the lower pressure drop.



**Figure 4-18** The pressure drop and friction factor as a function of channel porosity for the inlet velocity at 0.04 m/s (at a constant flow rate).







**Figure 4-19** Contours of velocity in the main flow direction for the super velocity of 0.04 m/s (red: high, blue: low). (a)  $d/a = 2$ ; (b)  $d/a = 1$ ; (c)  $d/a = 0.5$ ; (d)  $d/a = 0.25$ .

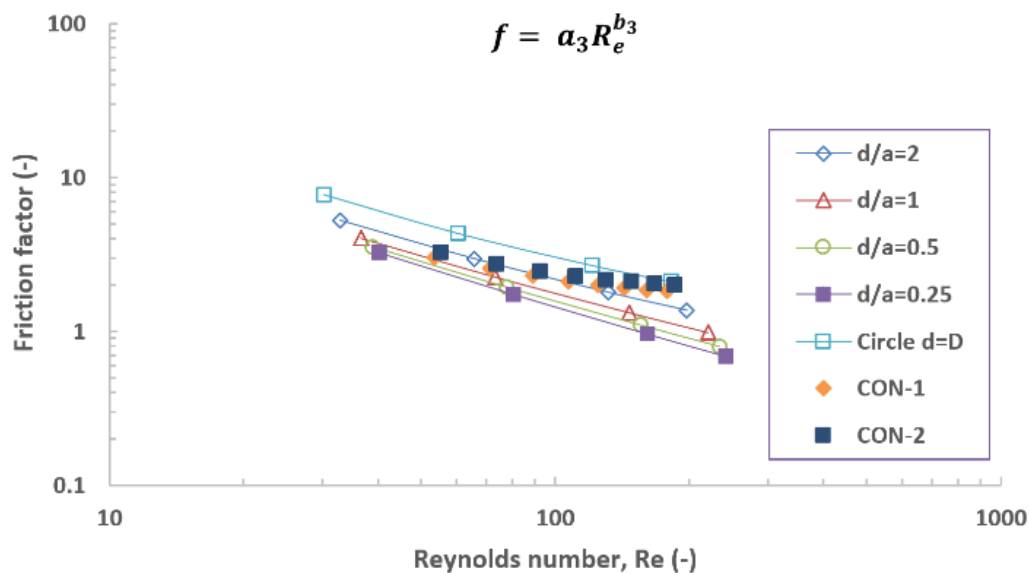
### 4.3.2 Friction Factor and the Dimensionless Power Number

The pressure drop in the SW membrane channel directly reduces the total transmembrane pressure that acts on the membrane surface. A driven pump has to maintain the transmembrane pressure; so, in the separation process, higher energy is required to compensate for the energy loss influenced by the pressure losses. To make comparisons across different feed spacer situations, the pressure drop can be expressed in terms of the friction factor. The friction factor is commonly employed as a dimensionless parameter to find the changing inclination for different Reynolds numbers. The relationship is presented as the following equation,

$$f = f(R_e). \quad (9)$$

**Figure 4-20** shows the friction factor generated by the feed spacer with different connecting filament diameters and different Reynolds numbers. **Table 4-4** lists the results reported in the study by Schock et al. [2]. The pressure drop increased when the Reynolds number increased, but the friction factor decreased when the Reynolds number increased. As the connecting filament diameter decreased (the channel porosity was increased), the

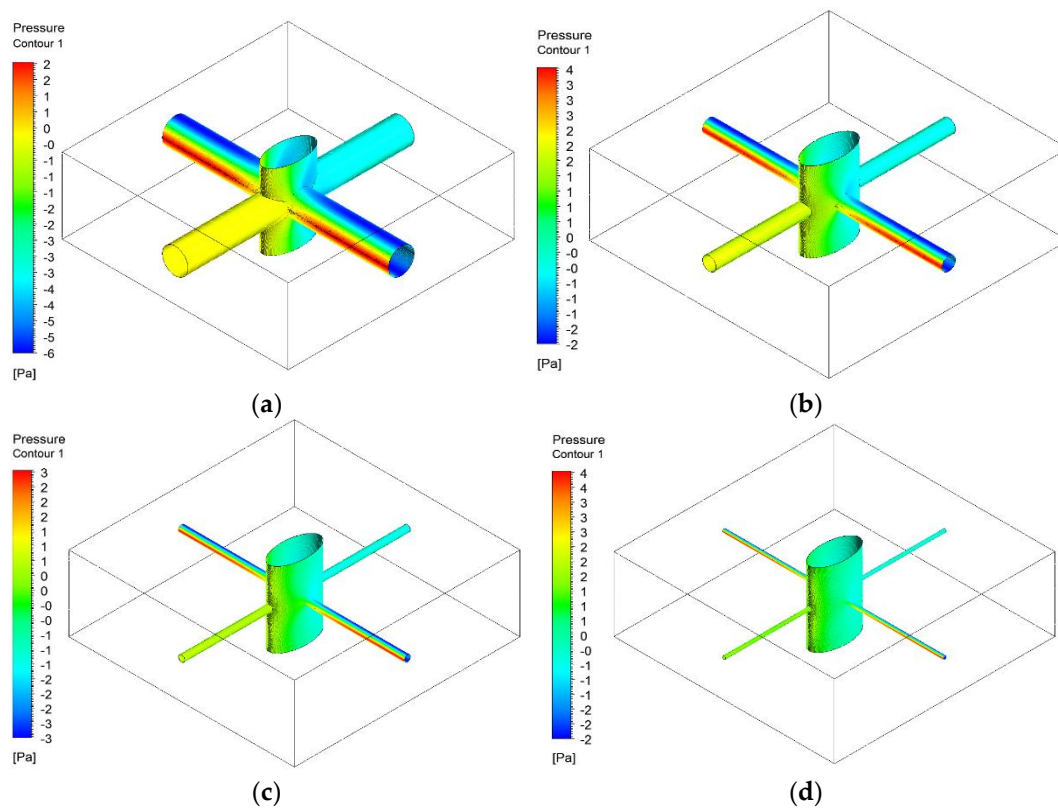
flow cross-section of the channel obstructed by the feed spacer decreased. The pressure drop and friction factor values were higher when the porosity was low. The friction factor decreased when the porosity increased; however, the amplitude gradually became smaller, as shown in **Figure 4-20**. Moreover, from the contours of total pressure shown in **Figure 4-21**, the higher filament diameter generated a higher friction factor linked to the filament drag, and this was described as the drag coefficient in previous studies [45,46]. Moreover, the Haaksman et al. experimental friction factor results for the commercial spacers were added to **Figure 4-20** [23]. The results of the current study tended to agree with results from the study by Haaksman et al. At the Reynolds number of 150, the pillar-like feed spacer  $d/a = 0.25$  reduced by almost 43.63% compared to the commercial spacer CON-1. In the same group, the friction factor was lower than the commercial spacer CON-2 by almost 49.23% at the same Reynolds number. **Figure 4-22** showed that for different conjunction cross-section, at lower Reynold numbers the value of friction factor was close to the commercial spacers, but at the higher Reynold numbers friction factor was smaller than the commercial spacers. Friction factor did not change too much with different conjunction cross-section. Group Drop  $b=a/2$  got the lowest value of friction factor. Additionally, the configuration of connecting filament changing enhanced frition factor shown in **Figure 4-23**. With these configurations the transverse filaments forced the flow cross narrow slit. The velocity increased with higher flushing on membrane surface shown in **Figure 4-24**.



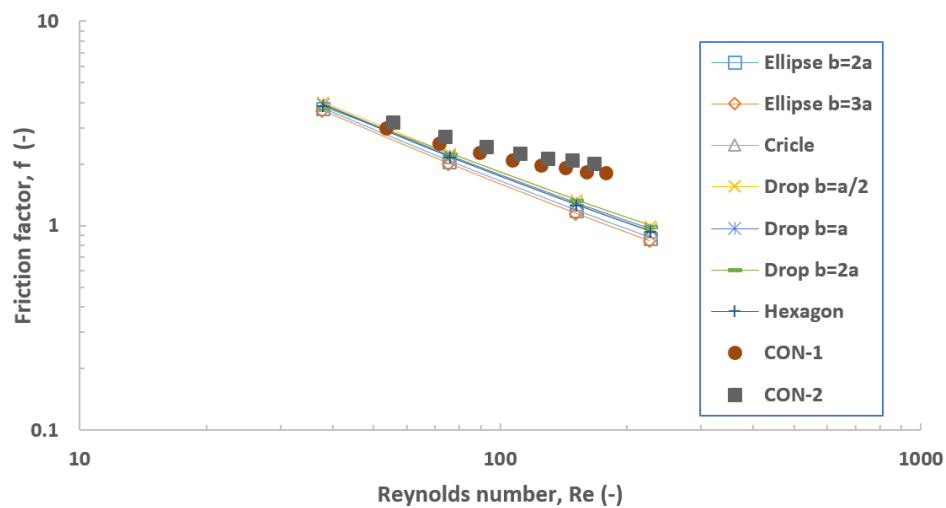
**Figure 4-20** The friction factor, associated with the connecting filament diameter, as a function of the Reynolds number. A comparison was made with the friction factor results of Haaksman et al. [23].

**Table 4-4** The friction factor function parameters.

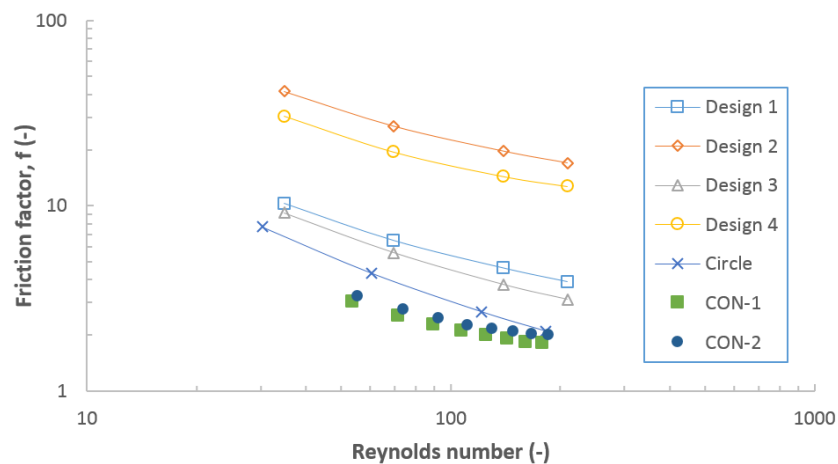
-	$a_3$	$b_3$	
d/a = 0.25	79.215	-0.867	
d/a = 0.5	73.599	-0.832	
d/a = 1	68.338	-0.79	
d/a = 2	71.529	-0.753	
d = D	88.172	-0.724	
	Film Tec	105	-0.8
Schock et al. [2]	Toray PEC1000	13	-0.8
	HP Tricot	46	-0.8
	Desal RO	105	-0.8



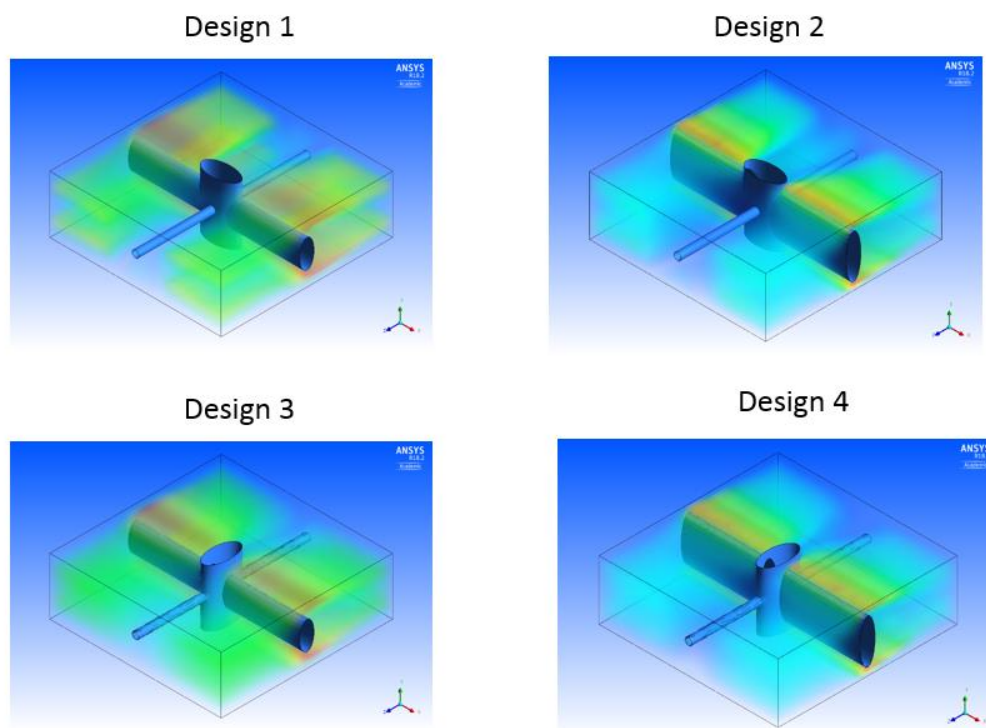
**Figure 4-21** The contours of total pressure in the main flow direction for the super velocity of 0.04 m/s (red: high, blue: low). (a)  $d/a = 2$ ; (b)  $d/a = 1$ ; (c)  $d/a = 0.5$ ; (d)  $d/a = 0.25$ .



**Figure 4-22** The friction factor associated with the conjunction cross-section,



**Figure 4-23** The friction factor, associated with the configuration of connecting filament.



**Figure 4-24** Different configuration of traverse filament

Besides the friction factor, the dimensionless power number has also been commonly employed to simulate the pressure drop through energy consumption. The dimensionless power number increased when the Reynolds number increased. However,

like the friction factor, the dimensionless power number was stable versus the channel porosity. In the work by Koutsou et al. [27] the dimensionless power number reached  $10^7$  when the Reynolds number equaled 200. **Figure 4-25** shows that for the feed spacer  $d/a = 2$ , the dimensionless power number value was in agreement with the value in the numerical simulation results of Koutsou et al. [27]. However, the dimensionless power number was lower as the  $d/a$  decreased, and the dimensionless power number was also lower with low porosity. The relationship between the dimensionless power number and the Reynolds number is presented as the following equation,

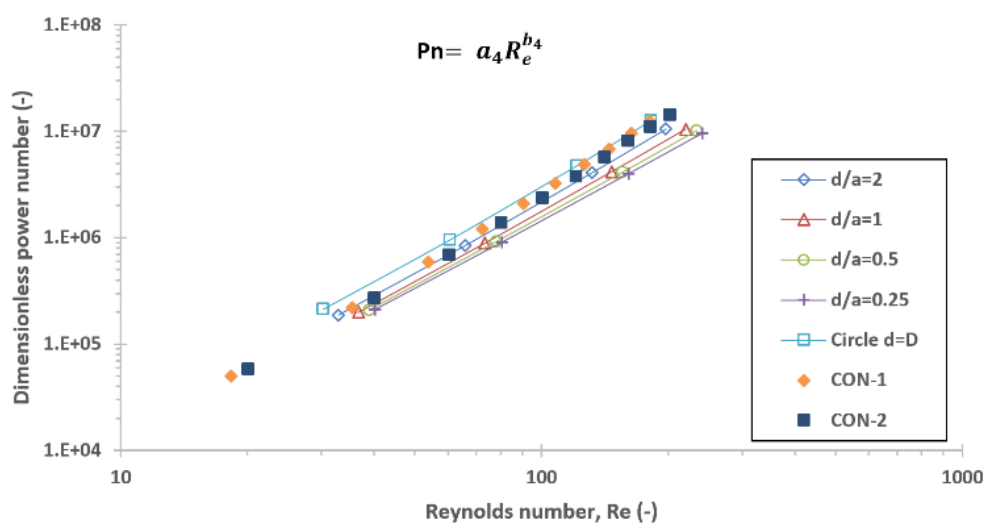
$$P_n = f(R_e). \quad (10)$$

**Figure 4-25** shows the dimensionless power number generated by the feed spacer with different connecting filament diameters for different Reynolds numbers. From Equation (6) and Equation (10), the parameter  $a_3 = a_4$ ,  $b_4 = 3 + b_3$ . Li et al. reported experimental empty channel results on this relationship [47]. The pillar-like feed spacer results were compared with the results from Li et al. (which are listed in **Table 4-5**). The  $a_4$  and  $b_4$  were higher than the empty channel due to the hydraulic resistance from the spacer filament drag.

The results of Haaksman et al. [23] on the dimensionless power number of the commercial spacer were also added for comparison in **Figure 4-25**. The results of the current study tended to agree with the results of Haaksman et al., where the friction factor decreased when the Reynolds number increased, although more quickly, and the dimension power number increased when the Reynolds number increased, although more slowly. The minimum group  $d/a = 0.25$  friction factor was lower than the commercial spacer CON-1

by almost 52.93% at the Reynolds number of 150. In the same group, the dimensionless power number was lower than the commercial spacer CON-2 by almost 47.31% at the same Reynolds number.

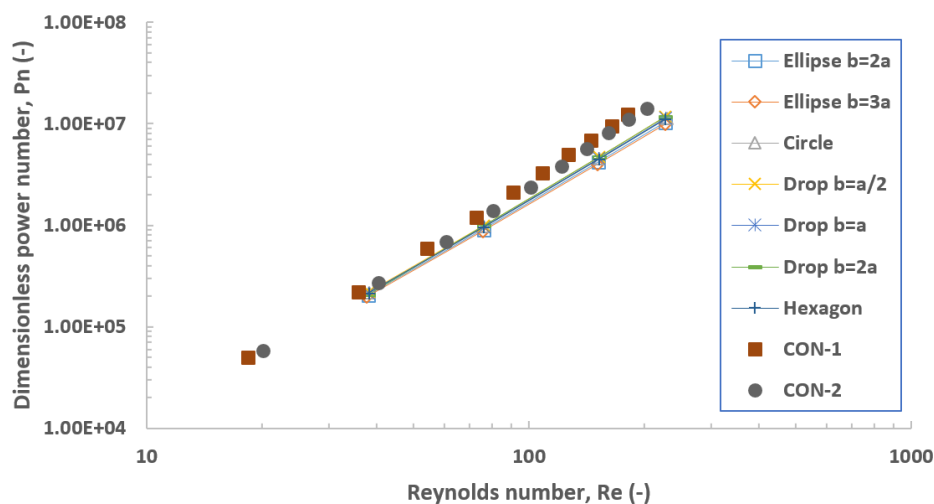
The porosities of CON-1 and CON-2 were 0.855 and 0.866, respectively [23], and for the group filament conjunction with the circular cross-section  $d = D$ , the porosity was 0.867. The value of the friction factor and the dimensionless power number approached those of CON-1 and CON-2 at a higher Reynolds number. This inclination indicated the effect of the filament drag on the energy consumption shown as channel porosity.



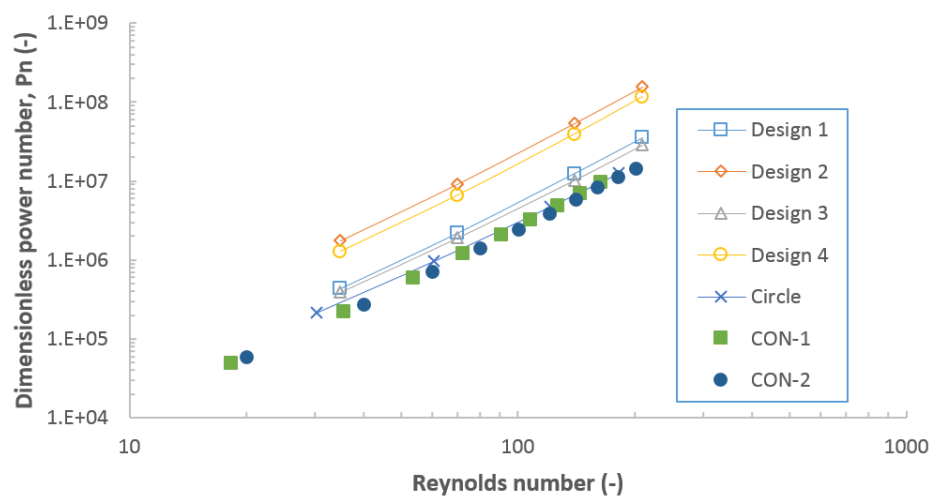
**Figure 4-25** The dimensionless power number, associated with the connecting filament diameter, as a function of the Reynolds number. A comparison was made with the dimensionless results of Haaksman et al. [23].

**Table 4-5** The dimensionless power number function parameters.

-	$a_4$	$b_4$
$d/a = 0.25$	79.215	2.1326
$d/a = 0.5$	73.599	2.1678
$d/a = 1$	68.338	2.2105
$d/a = 2$	71.529	2.2467
$d = D$	88.172	2.2756
Li empty channel [47]	12	2



**Figure 4-26** The dimensionless power number associated with the conjunction cross-section



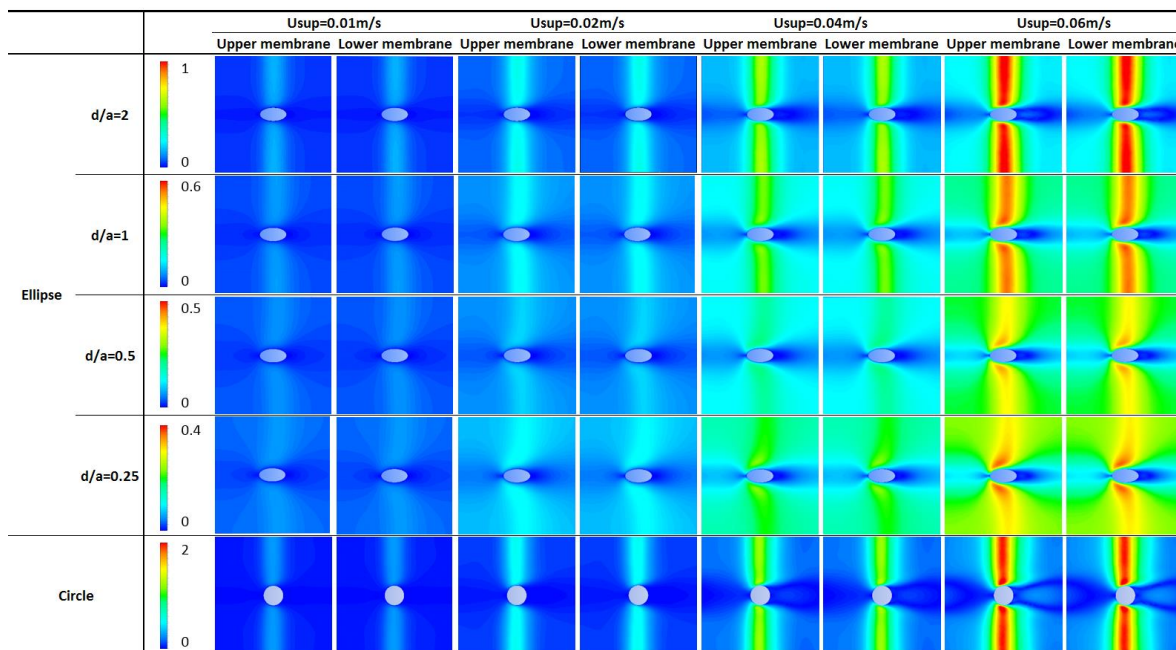


**Figure 4-27** The dimensionless power number associated with the configuration of connecting filament.

**Figure 4-15** showed that for different conjunction cross-section, at lower Reynold numbers the value of the dimensionless power number was agree with the commercial spacers, but at the higher Reynold numbers the dimensionless power number was smaller than the commercial spacers. The dimensionless power number did not change too much with different conjunction cross-section. Group Drop  $b=a/2$  got the lowest value of the dimensionless power number. Additionally, the configuration of connecting filament changing enhanced the dimensionless power number shown in **Figure 4-27**, but in acceptable rang.

### 4.3.3 The Modified Friction Factor

RO membrane fouling relates to the hydrodynamics adjacent to the membrane surface. Even a new biomass attachment is dependent on the distribution of shear stress on the walls. An analysis of the wall shear stress was key to understanding the effect of hydrodynamics in the membrane wall region. Wall shear stress,  $\tau$ , was indicated by the relation of the velocity shear rate  $\tau = \mu du/dy$  at the laminar flow. In this study, the wall shear stress simulation comparison for the different feed spacer structures was considered by comparisons of the wall shear stress contours and the modified friction factor's application.



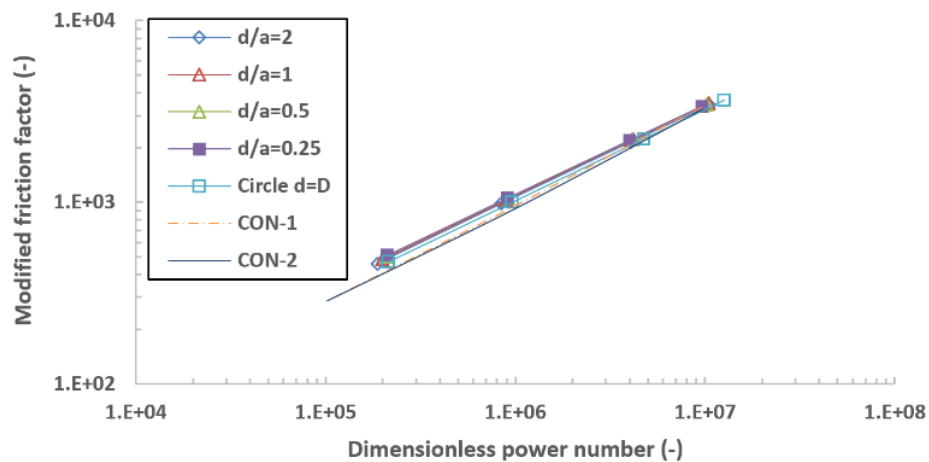
**Figure 4-28** The contour plots of the wall shear stress ( $\tau$ ) profile on the upper membrane and the lower membrane generated by the pillar-like feed spacer.

The area average wall shear stress profiles were visualized by a two-dimensional (2D) contour plot from the 3D model. **Figure 4-28** depicts the 2D contour plot of the wall shear stress on the upper membrane and lower membrane for the super velocities  $0.01 \text{ m s}^{-1}$ ,  $0.02 \text{ m s}^{-1}$ ,  $0.04 \text{ m s}^{-1}$ , and  $0.06 \text{ m s}^{-1}$  at different diameters of connecting filament. As a tool for statistical validity, the distribution of shear stress was shown under different super velocities and porosities, as shown in **Figure 4-28**. Changes in the different Reynolds numbers and different porosities were concluded as follows:

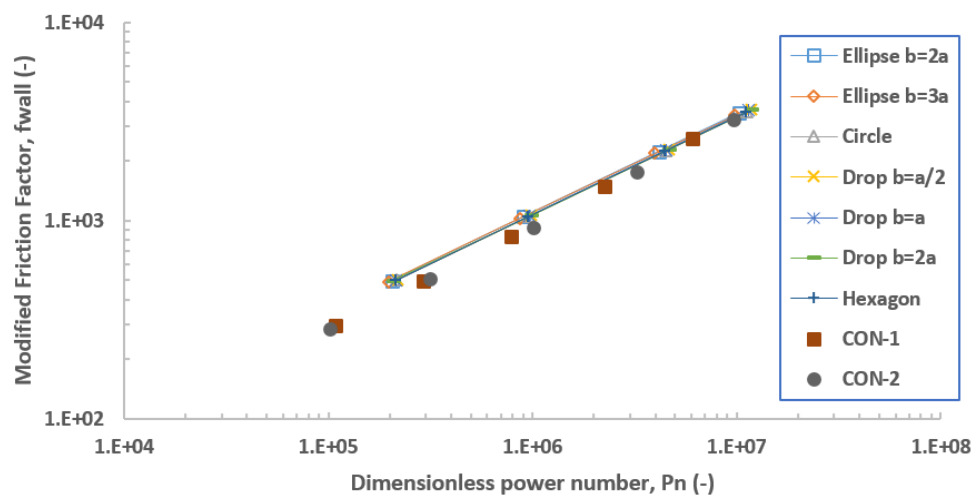
1. Based on the contour plot, the upper membrane and the lower membrane exhibited small differences in the wall shear stress profiles of the symmetric structure of the pillar-like feed spacer.

2. From the color of the wall shear stress contours with a high Reynolds number, the wall shear stress was higher than with a low Reynolds number.
3. It was obvious that a high channel porosity generated a low area average wall shear stress.
4. High connecting filament diameters generated high wall shear stress focused on the membrane surface region above and below the connecting filament through its compression.
5. The existence of high hydrodynamics on the upper membrane and lower membrane walls with an increasing Reynolds number enhanced the concentration reduction ability.

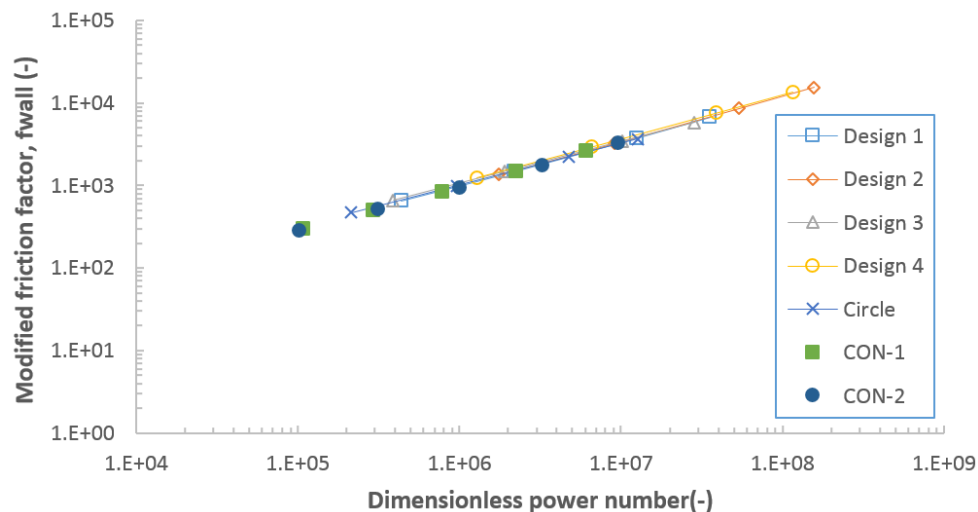
The modified friction factor was computed under the plot in **Figure 4-29**. As a function of the dimensionless power number, the modified friction factor was illustrated in Equation (7). Santos et al. [4,16] reported that the modified friction factor was slightly higher than  $10^3$  when the dimensionless power number approached  $10^6$ . Vicktor et al. [23] issued a similar report detailing that, when the dimensionless power number was close to  $10^6$ , the modified friction factor was approximately  $10^3$ . Additionally, compared to the Haaksman et al. results that were added in **Figure 4-29**, the current study's results on the modified friction factor agreed with the results of Haaksman et al.; however, the value of the modified friction factor was higher. As the dimensionless power number reached  $10^6$ , the modified friction factor was enhanced by almost 20.40% and 22.27% compared to the commercial spacers CON-1 and CON-2, respectively.



**Figure 4-29** The modified friction factor, associated with the connecting filament diameter, as a function of the dimensionless power number. A comparison was made with the modified friction factor of Haaksman et al. [23].



**Figure 4-30** The modified friction factor associated with the conjunction cross-section



**Figure 4-31** The modified friction factor associated with the configuration of connecting filament.

**Figure 4-30** showed that for different conjunction cross-section, at higher Reynold numbers the value of the modified friction factor was agree with the commercial spacers, but at the lower Reynold numbers the modified friction factor was higher than the commercial spacers. The modified friction factor did not change too much with different conjunction cross-section. The effect from the conjunction cross-section on the distribution of shear stress was lower than the transverse filament. Additionally the modified friction factor were similar with the different configurations of connecting filament shown in **Figure 4-31**. Different configurations chanthe ged partial value of shear stress on membrane surface, but did not change the average shear stress apparently.

#### 4.4 Conclusions

- To lower the obstacle effect from the feed spacer in the SW Membrane feed channel, the support from the high porosity of the feed spacer structures with a small filament diameter was indispensable. The pillar-like feed spacer was introduced as a new template to manipulate energy consumption. Under laminar flow conditions, the element of the feed spacer between membrane envelopes was simulated using the CFD method. Subsequently, the simulation parameters were compared and validated with previous works. The main research findings revealed that, regarding the pressure drop, the decline in the connecting filament diameter of the pillar-like spacer and the rise in channel porosity reached 0.979. The inlet velocity was set at 0.04 m/s (at a constant flow rate), the channel porosity increased by 5%, and the pressure drop reduced by 62.56%. Compared with the results of previous works on conventional spacers and an empty channel, the current study's results on the pressure drop tended to be in agreement with them.
- For the friction factor, based on the numerical predictions, the results for the dimensionless power number and the modified factor agreed with previous conventional spacer results. At the Reynolds number of 150, the group  $d/a = 0.25$  friction factor reduced by almost 43.63% and 49.23% compared with the commercial spacers CON-1 and CON-2, respectively, and the dimensionless power number was lower than the commercial spacer CON-2 by almost 47.31% at the same Reynolds number for the same group.

- Regarding the shear stress, homogenization of distribution changed the flow profile close to the membrane. At the dimensionless power number  $10^6$ , the modified friction factor was enhanced by almost 20.40% and 22.27% compared to the commercial spacers CON-1 and CON-2, respectively.
- The effect from conjunction cross-section on energy consumption was lower than the traverse filament. For the modified friction factor the same inclination was with friction factor and the dimensionless power number.
  - The configuration of connecting filament defined the distribution of shear stress on membrane surface. The partial shear stress increasing caused more energy consumption.

## Reference

1. Van der Waal, M. J.; Racz, I. G. Mass transfer in corrugated-plate membrane modules. I. Hyperfiltration experiments. *J. Memb. Sci.* **1989**, *40*, 243–260, doi:10.1016/0376-7388(89)89008-8.
2. Schock, G.; Miquel, A. Mass transfer and pressure loss in spiral wound modules. *Desalination* **1987**, *64*, 339–352, doi:10.1016/0011-9164(87)90107-X.
3. Winograd, Y.; Solan, A.; Toren, M. Mass transfer in narrow channels in the presence of turbulence promoters. *Desalination* **1973**, *13*, 171–186, doi:10.1016/S0011-9164(00)82043-3.
4. Schwinge, J.; Wiley, D. E.; Fane, A. G. Novel spacer design improves observed flux. *J. Memb. Sci.* **2004**, *229*, 53–61, doi:10.1016/j.memsci.2003.09.015.
5. Vrouwenvelder, J. S.; Picioreanu, C.; Kruithof, J. C.; van Loosdrecht, M. C. M. Biofouling in spiral wound membrane systems: Three-dimensional CFD model based evaluation of experimental data. *J. Memb. Sci.* **2010**, *346*, 71–85, doi:10.1016/j.memsci.2009.09.025.
6. Karabelas, A. J.; Koutsou, C. P.; Sioutopoulos, D. C. Comprehensive performance assessment of spacers in spiral-wound membrane modules accounting for compressibility effects. *J. Memb. Sci.* **2018**, *549*, 602–615, doi:10.1016/j.memsci.2017.12.037.
7. Lee, J. Y.; Tan, W. S.; An, J.; Chua, C. K.; Tang, C. Y.; Fane, A. G.; Chong, T. H. The potential to enhance membrane module design with 3D printing technology. *J. Memb. Sci.* **2016**, *499*, 480–490, doi:10.1016/j.memsci.2015.11.008.



8. Siddiqui, A.; Farhat, N.; Bucs, S. S.; Linares, R. V.; Picioreanu, C.; Kruithof, J. C.; Van Loosdrecht, M. C. M.; Kidwell, J.; Vrouwenvelder, J. S. Development and characterization of 3D-printed feed spacers for spiral wound membrane systems. *Water Res.* **2016**, *91*, 55–67, doi:10.1016/j.watres.2015.12.052.
9. Cornelissen, E. R.; Vrouwenvelder, J. S.; Heijman, S. G. J.; Viallefont, X. D.; Van Der Kooij, D.; Wessels, L. P. Periodic air/water cleaning for control of biofouling in spiral wound membrane elements. *J. Memb. Sci.* **2007**, *287*, 94–101, doi:10.1016/j.memsci.2006.10.023.
10. Araújo, P. A.; Kruithof, J. C.; Van Loosdrecht, M. C. M.; Vrouwenvelder, J. S. The potential of standard and modified feed spacers for biofouling control. *J. Memb. Sci.* **2012**, *403–404*, 58–70, doi:10.1016/j.memsci.2012.02.015.
11. Haidari, A. H.; Heijman, S. G. J.; van der Meer, W. G. J. Visualization of hydraulic conditions inside the feed channel of Reverse Osmosis: A practical comparison of velocity between empty and spacer-filled channel. *Water Res.* **2016**, *106*, 232–241, doi:10.1016/j.watres.2016.10.012.
12. Radu, A. I.; Vrouwenvelder, J. S.; van Loosdrecht, M. C. M.; Picioreanu, C.; Posadzy-Malaczyńska, A.; Kosch, M.; Hausberg, M.; Rahn, K. H.; Stanisic, G.; Malaczynski, P.; Gluszek, J.; Tykarski, A.; Radu, A. I.; Vrouwenvelder, J. S.; van Loosdrecht, M. C. M.; Picioreanu, C. Effect of flow velocity, substrate concentration and hydraulic cleaning on biofouling of reverse osmosis feed channels. *Chem. Eng. J.* **2012**, *188*, 30–39, doi:10.1016/j.cej.2012.01.133.
13. Radu, A. I.; Bergwerff, L.; van Loosdrecht, M. C. M.; Picioreanu, C. Combined

- biofouling and scaling in membrane feed channels: a new modeling approach. *Biofouling* **2015**, *31*, 83–100, doi:10.1080/08927014.2014.996750.
14. Pervov, A. G. Scale formation prognosis and cleaning procedure schedules in reverse osmosis systems operation. *Desalination* **1991**, *83*, 77–118, doi:10.1016/0011-9164(91)85087-B.
  15. Da Costa, A. R.; Fane, A. G. Net-Type Spacers: Effect of Configuration on Fluid Flow Path and Ultrafiltration Flux. *Ind. Eng. Chem. Res.* **1994**, *33*, 1845–1851, doi:10.1021/ie00031a026.
  16. Santos, J. L. C.; Geraldes, V.; Velizarov, S.; Crespo, J. G. Investigation of flow patterns and mass transfer in membrane module channels filled with flow-aligned spacers using computational fluid dynamics (CFD). *J. Memb. Sci.* **2007**, *305*, 103–117, doi:10.1016/j.memsci.2007.07.036.
  17. Cao, Z.; Wiley, D. E.; Fane, A. G. CFD simulations of net-type turbulence promoters in a narrow channel. *J. Memb. Sci.* **2001**, *185*, 157–176, doi:10.1016/S0376-7388(00)00643-8.
  18. Koutsou, C. P.; Yiantsios, S. G.; Karabelas, A. J. Numerical simulation of the flow in a plane-channel containing a periodic array of cylindrical turbulence promoters. *J. Memb. Sci.* **2004**, *231*, 81–90, doi:10.1016/j.memsci.2003.11.005.
  19. Song, L.; Ma, S. Numerical studies of the impact of spacer geometry on concentration polarization in spiral wound membrane modules. *Ind. Eng. Chem. Res.* **2005**, *44*, 7638–7645, doi:10.1021/ie048795w.
  20. Gu, B.; Adjiman, C. S.; Xu, X. Y. The effect of feed spacer geometry on membrane

- performance and concentration polarisation based on 3D CFD simulations. *J. Memb. Sci.* **2017**, *527*, 78–91, doi:10.1016/j.memsci.2016.12.058.
21. Van Gauwbergen, D.; Baeyens, J. Macroscopic fluid flow conditions in spiral-wound membrane elements. *Desalination* **1997**, *110*, 287–299, doi:10.1016/S0011-9164(97)00104-5.
  22. Koutsou, C. P.; Karabelas, A. J. A novel retentate spacer geometry for improved spiral wound membrane (SWM) module performance. *J. Memb. Sci.* **2015**, *488*, 129–142, doi:10.1016/j.memsci.2015.03.064.
  23. Haaksman, V. A.; Siddiqui, A.; Schellenberg, C.; Kidwell, J.; Vrouwenvelder, J. S.; Picioreanu, C. Characterization of feed channel spacer performance using geometries obtained by X-ray computed tomography. *J. Memb. Sci.* **2017**, *522*, 124–139, doi:10.1016/j.memsci.2016.09.005.
  24. Lau, K. K.; Abu Bakar, M. Z.; Ahmad, A. L.; Murugesan, T. Effect of feed spacer mesh length ratio on unsteady hydrodynamics in 2d spiral wound membrane (swm) channel. *Ind. Eng. Chem. Res.* **2010**, *49*, 5834–5845, doi:10.1021/ie9017989.
  25. Saeed, A.; Vuthaluru, R.; Vuthaluru, H. B. Impact of Feed Spacer Filament Spacing on Mass Transport and Fouling Propensities of RO Membrane Surfaces. *Chem. Eng. Commun.* **2015**, *202*, 634–646, doi:10.1080/00986445.2013.860525.
  26. Koutsou, C. P.; Karabelas, a. J. Towards optimization of spacer geometrical characteristics for spiral wound membrane modules. *Desalin. Water Treat.* **2010**, *18*, 139–150, doi:10.5004/dwt.2010.1382.
  27. Koutsou, C. P.; Yiantsios, S. G.; Karabelas, A. J. Direct numerical simulation of

- flow in spacer-filled channels: Effect of spacer geometrical characteristics. *J. Memb. Sci.* **2007**, *291*, 53–69, doi:10.1016/j.memsci.2006.12.032.
28. Versteeg, H.; Malalasekera, W. *An introduction to computational fluid dynamics: the finite volume method*; 2007;
29. Yuan, Z. X.; Tao, W. Q.; Wang, Q. W. Numerical prediction for laminar forced convection heat transfer in parallel-plate channels with streamwise-periodic rod disturbances. *Int. J. Numer. Methods Fluids* **1998**, *28*, 1371–1387, doi:10.1002/(SICI)1097-0363(19981215)28:9<1371::AID-FLD774>3.0.CO;2-A.
30. Fimbres-Weihs, G. A.; Wiley, D. E. Review of 3D CFD modeling of flow and mass transfer in narrow spacer-filled channels in membrane modules. *Chem. Eng. Process. Process Intensif.* **2010**, *49*, 759–781, doi:10.1016/j.cep.2010.01.007.
31. Schwinge, J.; Wiley, D. E.; Fletcher, D. F. A CFD study of unsteady flow in narrow spacer-filled channels for spiral-wound membrane modules. *Desalination* **2002**, *146*, 195–201, doi:10.1016/S0011-9164(02)00470-8.
32. Fimbres-Weihs, G. A.; Wiley, D. E. Numerical study of mass transfer in three-dimensional spacer-filled narrow channels with steady flow. *J. Memb. Sci.* **2007**, *306*, 228–243, doi:10.1016/j.memsci.2007.08.043.
33. Hayes, R. E. *Computational flow modeling for chemical reactor engineering*; 2002; Vol. 80; ISBN 0125769601.
34. Geraldés, V.; Semião, V.; De Pinho, M. N. Flow management in nanofiltration spiral wound modules with ladder-type spacers. *J. Memb. Sci.* **2002**, *203*, 87–102, doi:10.1016/S0376-7388(01)00753-0.

35. Saeed, A.; Vuthaluru, R.; Vuthaluru, H. B. Investigations into the effects of mass transport and flow dynamics of spacer filled membrane modules using CFD. *Chem. Eng. Res. Des.* **2015**, *93*, 79–99, doi:10.1016/j.cherd.2014.07.002.
36. Koutsou, C. P.; Yiantsios, S. G.; Karabelas, A. J. A numerical and experimental study of mass transfer in spacer-filled channels: Effects of spacer geometrical characteristics and Schmidt number. *J. Memb. Sci.* **2009**, *326*, 234–251, doi:10.1016/j.memsci.2008.10.007.
37. Picioreanu, C.; Vrouwenvelder, J. S.; van Loosdrecht, M. C. M. Three-dimensional modeling of biofouling and fluid dynamics in feed spacer channels of membrane devices. *J. Memb. Sci.* **2009**, *345*, 340–354, doi:10.1016/j.memsci.2009.09.024.
38. Lim, S. Y.; Liang, Y. Y.; Fimbres Weihs, G. A.; Wiley, D. E.; Fletcher, D. F. A CFD study on the effect of membrane permeance on permeate flux enhancement generated by unsteady slip velocity. *J. Memb. Sci.* **2018**, *556*, 138–145, doi:10.1016/j.memsci.2018.03.070.
39. Ranade, V. V.; Kumar, A. Fluid dynamics of spacer filled rectangular and curvilinear channels. *J. Memb. Sci.* **2006**, *271*, 1–15, doi:10.1016/j.memsci.2005.07.013.
40. Shakaib, M.; Hasani, S. M. F.; Mahmood, M. Study on the effects of spacer geometry in membrane feed channels using three-dimensional computational flow modeling. *J. Memb. Sci.* **2007**, *297*, 74–89, doi:10.1016/j.memsci.2007.03.010.
41. Horstmeyer, N.; Lippert, T.; Schön, D.; Schleder, F.; Picioreanu, C.; Achterhold, K.; Pfeiffer, F.; Drewes, J. E. CT scanning of membrane feed spacers – Impact of

- spacer model accuracy on hydrodynamic and solute transport modeling in membrane feed channels. *J. Memb. Sci.* **2018**, *564*, 133–145, doi:10.1016/j.memsci.2018.07.006.
42. Siddiqui, A.; Lehmann, S.; Haaksman, V.; Ogier, J.; Schellenberg, C.; van Loosdrecht, M. C. M.; Kruithof, J. C.; Vrouwenvelder, J. S. Porosity of spacer-filled channels in spiral-wound membrane systems: Quantification methods and impact on hydraulic characterization. *Water Res.* **2017**, *119*, 304–311, doi:10.1016/j.watres.2017.04.034.
43. Da Costa, A. R.; Fane, A. G.; Wiley, D. E. Spacer characterization and pressure drop modelling in spacer-filled channels for ultrafiltration. *J. Memb. Sci.* **1994**, *87*, 79–98, doi:10.1016/0376-7388(93)E0076-P.
44. Da Costa, A. R.; Fane, A. G.; Fell, C. J. D.; Franken, A. C. M. Optimal channel spacer design for ultrafiltration. *J. Memb. Sci.* **1991**, *62*, 275–291, doi:10.1016/0376-7388(91)80043-6.
45. Dendukuri, D.; Karode, S. K.; Kumar, A. Flow visualization through spacer filled channels by computational fluid dynamics-II: Improved feed spacer designs. *J. Memb. Sci.* **2005**, *249*, 41–49, doi:10.1016/j.memsci.2004.06.062.
46. Taamneh, Y.; Bataineh, K. Improving the performance of direct contact membrane distillation utilizing spacer-filled channel. *Desalination* **2017**, *408*, 25–35, doi:10.1016/j.desal.2017.01.004.
47. Li, F.; Meindersma, W.; De Haan, A. B.; Reith, T. Experimental validation of CFD mass transfer simulations in flat channels with non-woven net spacers. *J. Memb. Sci.*

**2004**, 232, 19–30, doi:10.1016/j.memsci.2003.11.015.

# I

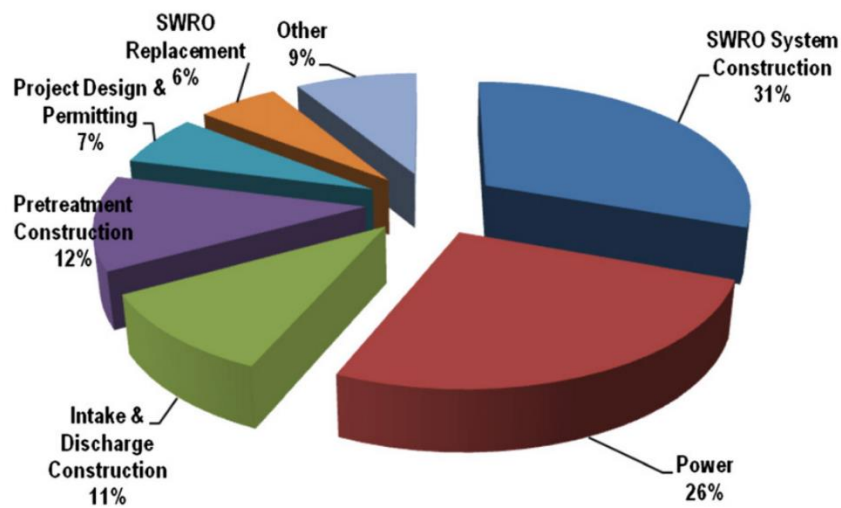
## Arc-like spacer

*This chapter presents the importance of mixing improvement for concentration gradient near membrane surface in feed channel of spiral wound module. Another spacer design is given out for this purpose. Flow situations defined by the spacer structure were investigated by using CFD simulation. The results of energy consumption and shear stress are compared with the commercial spacer.*

### 5.1 Introduction

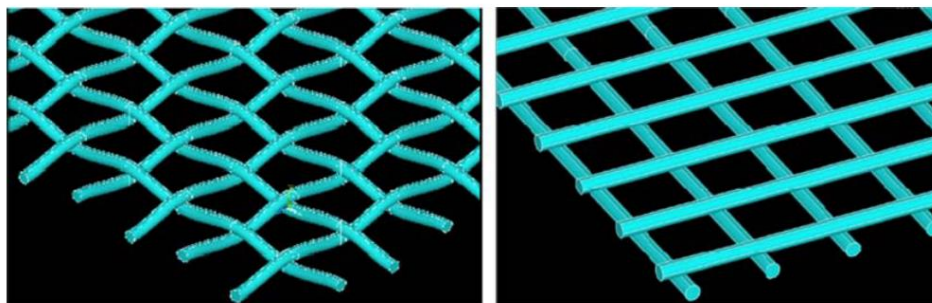
The increased water demand caused by an increased population, industrial expansion, tourism, and agricultural development urges augmenting the water supply in many water-stressed or arid regions or countries. Reverse osmosis (RO) as a desalination technology has become widely accepted for the purification of water for drinking or other purposes due to the reduction in desalination cost achieved through significant technological advances. In membrane technology, the two most used configurations of commercial membrane elements are spiral wound and hollow fiber. Spiral wound modules (SWM) wrap a leaf around a tube for perforated permeate collection to create a compact structure. Two flat membrane sheets separated by a spacer to form a channel for feed flow are assembled into a leaf.





**Figure 5-1** SWRO plant construction cost breakdown [1]

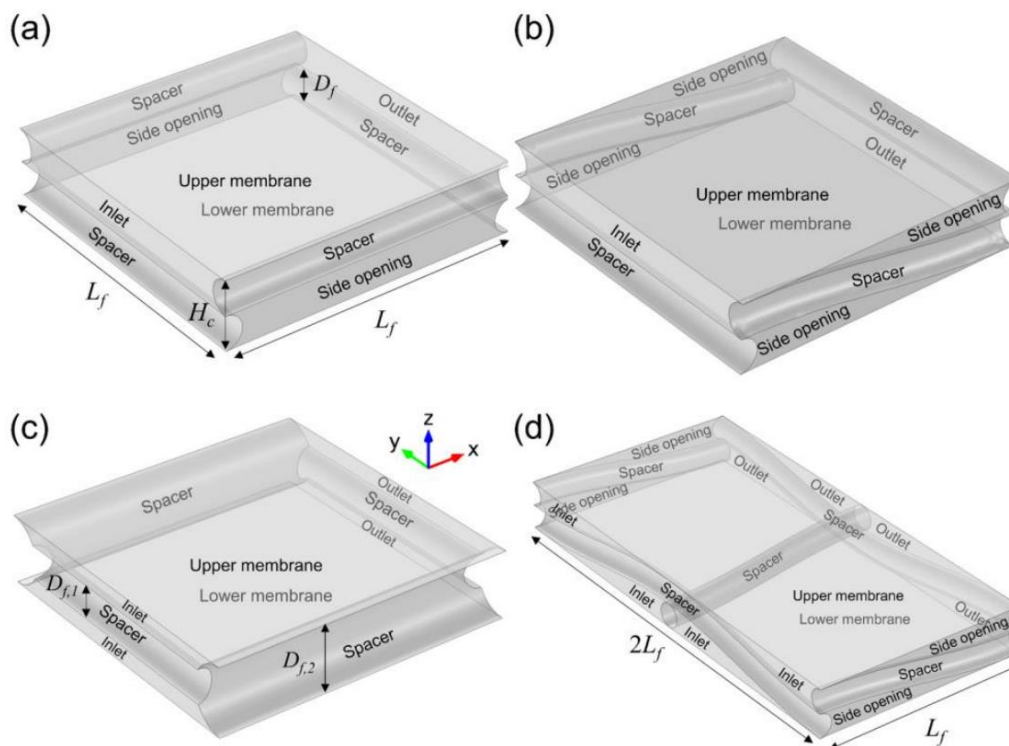
Concentration polarization and fouling are the inevitable phenomena that are the prime reasons for flux reduction in commercial water treatment processes. Avoiding membrane fouling, pretreatment of feed flow, and so on have been taken into consideration by many researchers [1]. Spacers, as an essential part of SWMs, not only create a feed channel, but also promote the mixing of feed fluid at the same time, which affects the flow patterns near the membrane surface related with the fouling inclination and concentration gradient.



**Figure 5-2** Computational reproduction of the modeling of the (left) woven net spacer and the (right) overlapped one [2].



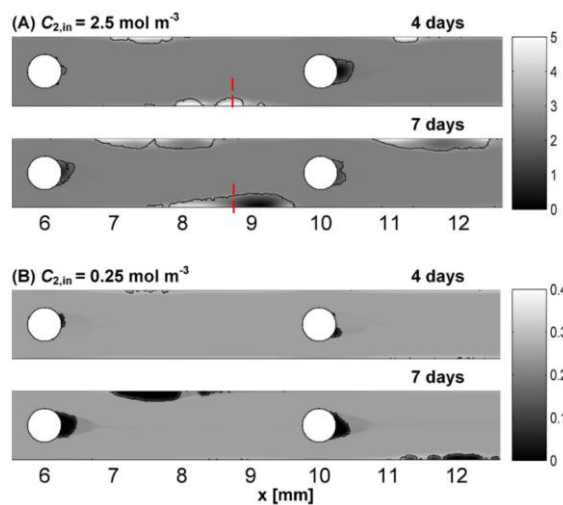
**Figure 5-3** Conventional net-type spacers mentioned Lee et al. study [3].



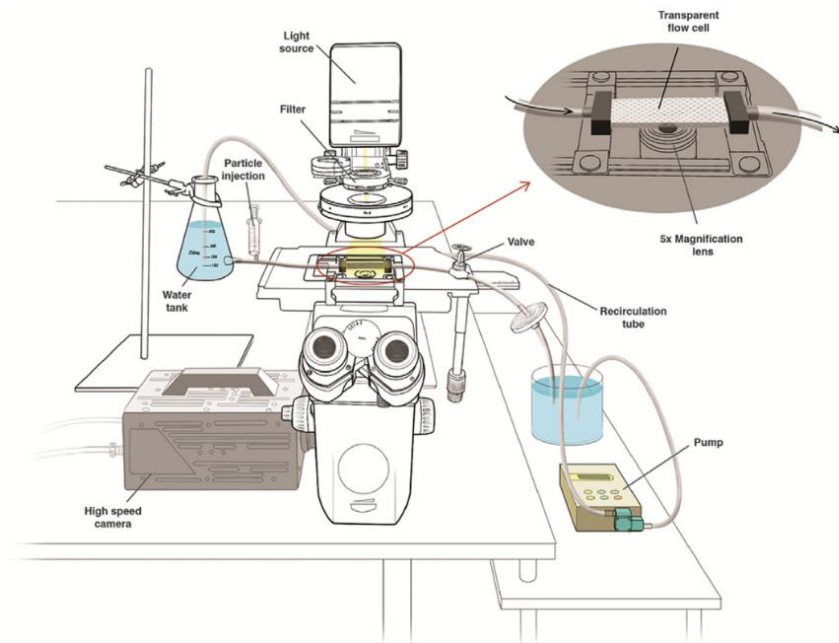
**Figure 5-4** Selected filament arrangements in Gu, Boram et al.[4].

Most of conventional spacer applying in separation process are woven and non-woven spacer [2,3]. Spacer geometry and the dead zone behind the spacer have been focused on in many numerical and experimental studies. For instance, Boram et al. reported the effect of feed spacer geometry on membrane performance and concentration

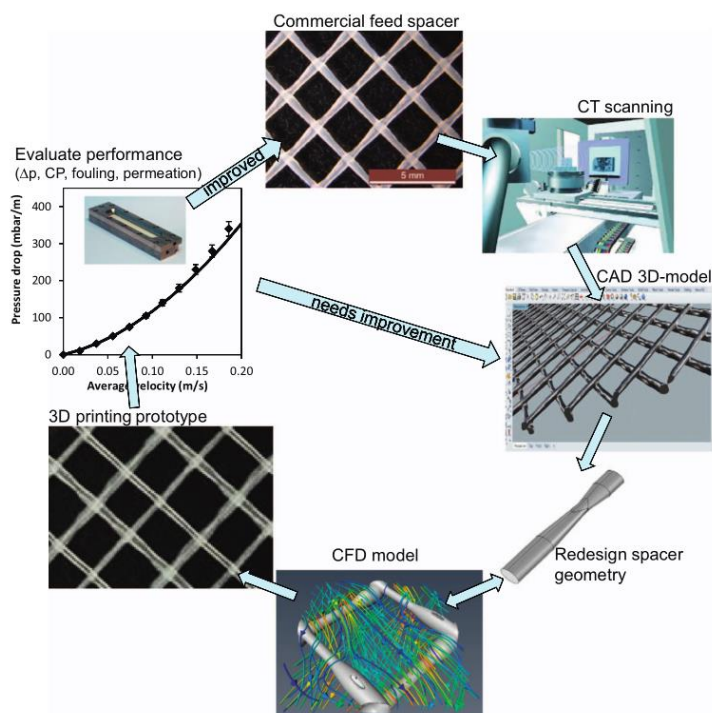
polarization based on CFD (computational fluid dynamics) simulation [4]. In their study, four types of feed spacer configurations, namely nonwoven, partially woven, middle layer, and fully woven, were investigated through three-dimensional simulations. Their numerical simulation results indicated that fully woven spacers showed better performance than other configurations in mitigating concentration polarization and delivering water flux by the mesh angle of  $60^\circ$ , but a greater pressure drop was caused than with their nonwoven counterparts. Sablani et al. experimentally found [5] a decrease in flux with decreasing spacer thickness, but for the intermediate spacer thickness, the maximum permeate flow was generated. Radu et al. reported that substrate rejection due to concentration polarization increased with biofilm thickness, depending on flow pattern [6]. Particle Image Velocimetry (PIV) was applied to visually investigate the flow patterns determined by the feed spacer; PIV is considered to be a non-invasive and high-resolution experimental method [7]. CT scanning and 3D printing, which has long history in spacer study, are applied to investigate the details of spacer by experimental testing [3,8].



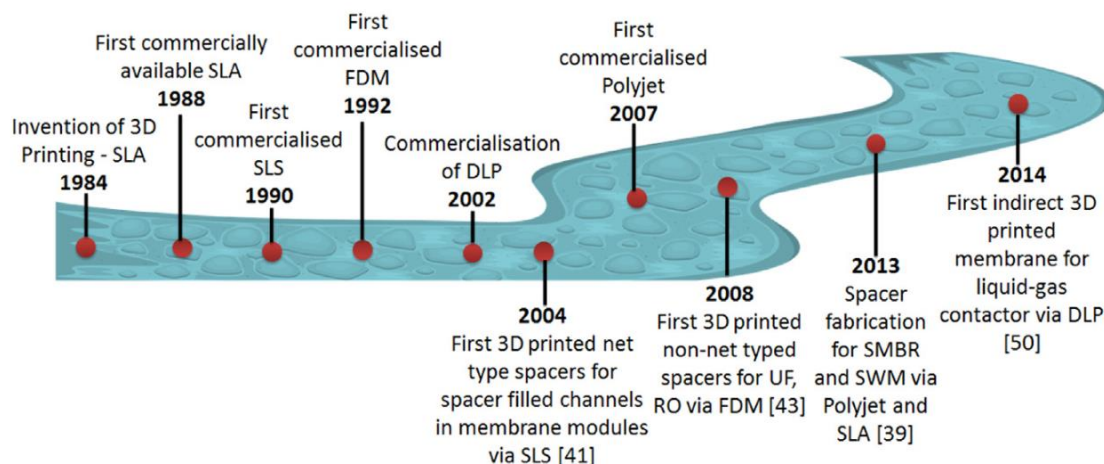
**Figure 5-5** Details with 2-d substrate concentration distribution and biofilm structures at different substrate concentrations in the feed water reported Radu, A. I. et al.[6].



**Figure 5-6** Experimental setup used for water flow measurements and visualization, using particle image velocimetry (PIV) [7].



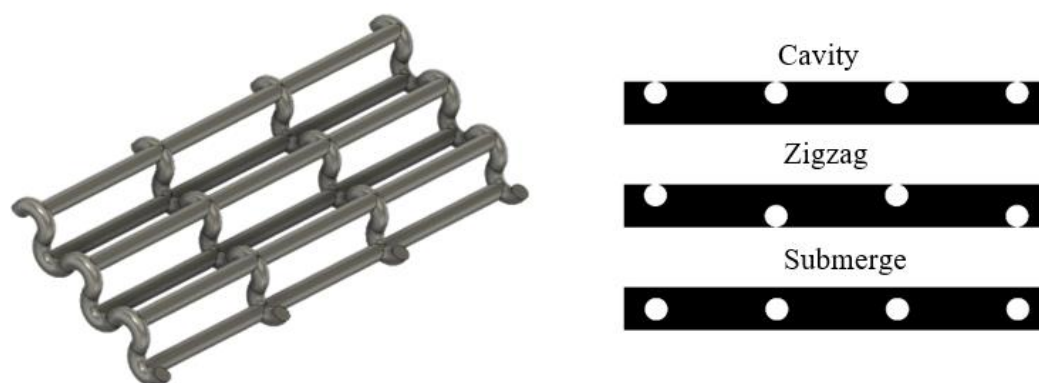
**Figure 5-7** Proposed steps in the development of improved spacers for membrane filtration systems involving, 3D printing, CT scanning and numerical modeling in conjunction with experimental testing [8].



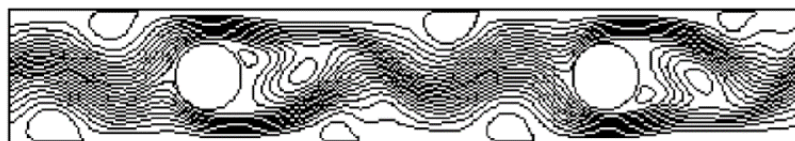
**Figure 5-8** Milestones of 3D printing in membrane modules design [3].

The study of spacers is a direct method to improve flow patterns to reduce fouling. In previous studies, three kinds of configurations, namely zigzag, submerged, and cavity, have been focused on in two-dimensional configuration simulations for classic spacer geometry (**Figure 5-9**). Compared with the submerged configuration and cavity configuration, the zigzag configuration is the most efficient spacer type for a spiral wound membrane module [9]. However, in the open channel, the highest axial pressure drop is found for the submerged configuration. From previous works, mixing improvement is one of the key methods to optimize flux in curved channel [10,11]. Spacer configuration can be characterized by the distance between spacer filaments; the angle between the spacer filaments,  $\beta$ ; and the flow attack angle,  $\alpha$ . The distance between the spacer filaments defines the porosity of the feed channel, and the angles define the flow regime and drag

force from the spacer. In this study, a arc-like spacer was designed to enhance the mixing ability, which was constructed with arched filaments and zigzag filaments. In this arc-like spacer design, the filament, which was parallel to the flow direction, was set as the zigzag configuration, and the transverse filament facing the flow direction was set as the arched filament in order to enhance the mixing between the fluid bulk and fluid elements adjacent to the membrane surface. Furthermore, the conjunction between the arched filament and zigzag filament had a small area of contact with the membrane, which reduced the dead zone caused by the shadow of the filament. The arched filament in the middle of the feed channel enabled the disruption of the solute concentration boundary layer. A schematic diagram of the modified feed spacer is illustrated in **Figure 5-9**.



**Figure 5-9** A view of the morphology of the modified feed spacer.

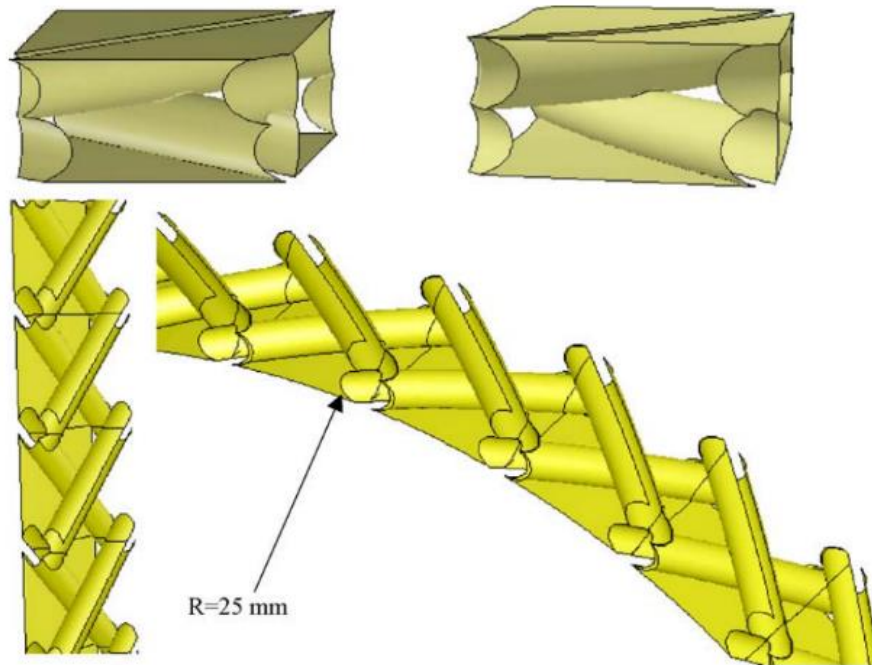


(a)

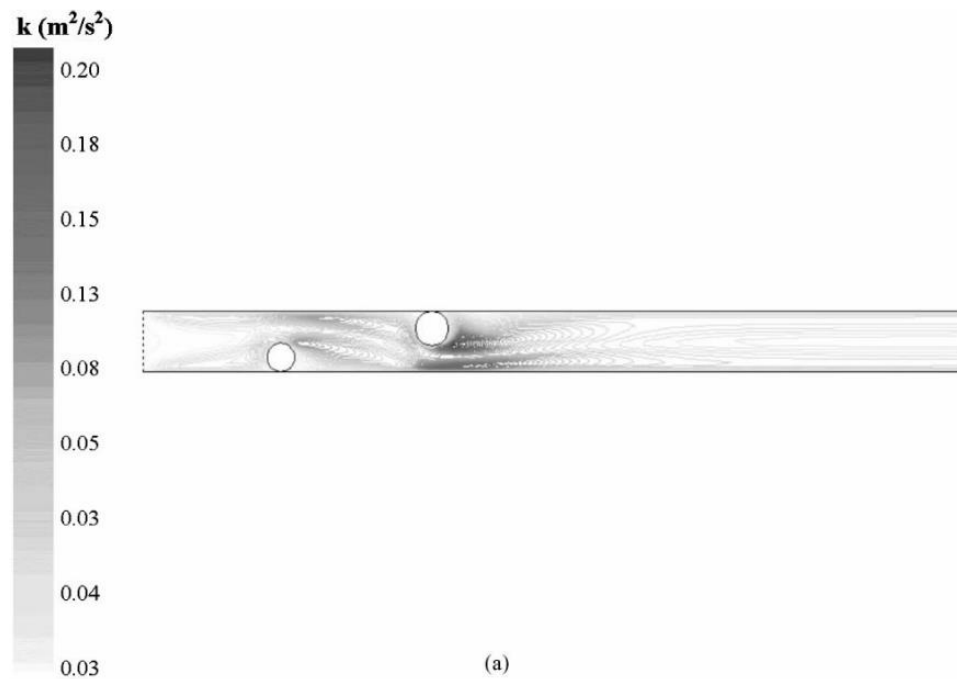


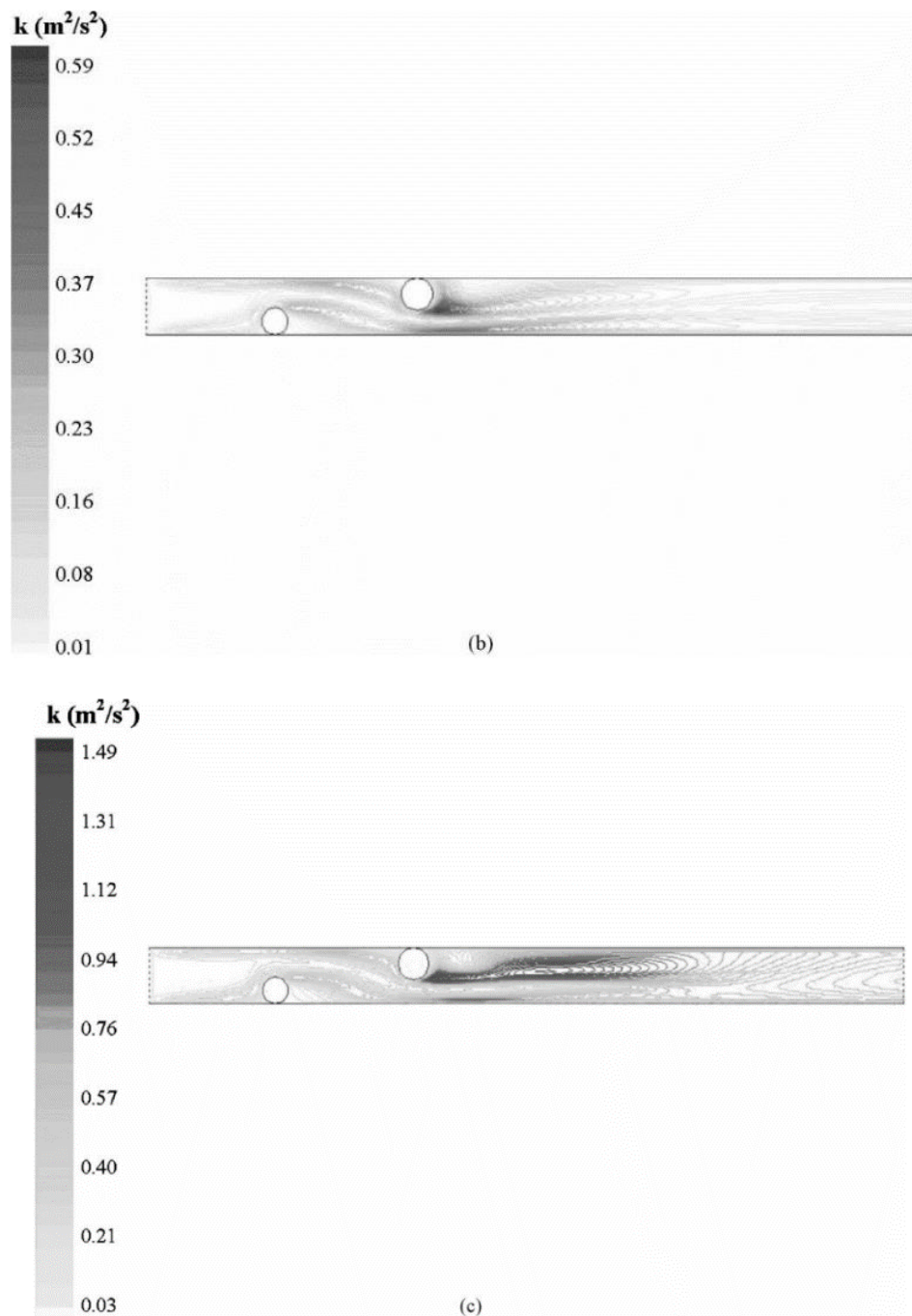
(b)

**Figure 5-10** Streamline (a) and vorticity contours (b) of Koutsou et al. study [9].



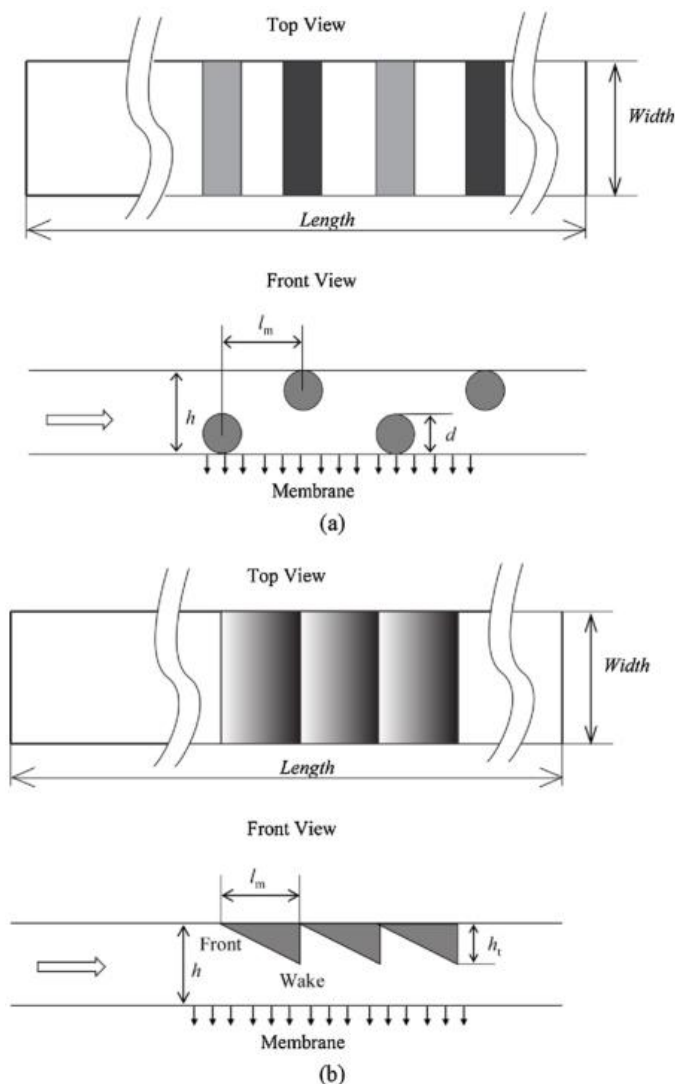
**Figure 5-11** Solution domain and computational grid for the curved channel in Ranade and Kumar study [10].





**Figure 5-12** Turbulent kinetic energy distribution at an inlet velocity equals to (a) 0.5 m/s; (b) 1.0 m/s; (c) 2.0 m/s — two opposing cylinders reported by Cao, Z. et al. [12].

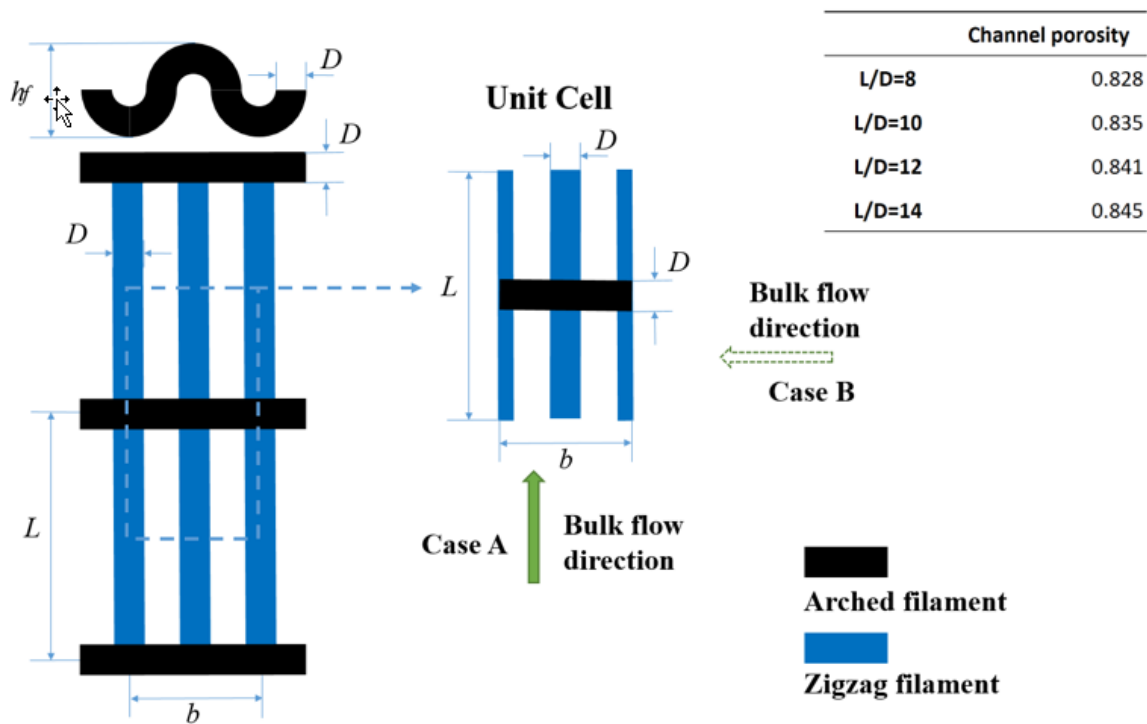




**Figure 5-13** Configurations of the zigzag spacer and saw-tooth spacer [11].

In the separating process, the rejected solute generates a concentration gradient in the boundary layer near the membrane surface, and this phenomenon is known as concentration polarization [13]. In typical net-like feed spacers, both woven and nonwoven, the flow in the feed channel is always divided into the boundary region and the bulk flow region. In the boundary region, concentration polarization is easily attained in the undisturbed condition. To enable the mixing of feed flow in two regions, the design of

the spacer configuration is one way to reduce the phenomenon of concentration polarization. Cao et al. reported that the enhancement of mass transfer is closely related to the high shear stress value, velocity fluctuation, and eddy formation, and that the location and inter filament distance of the spacers constrain the shear stress distribution, mass transfer coefficients, and pressure inside the channel [12]. To clarify the characteristics of the modified spacer, the simulation of two flow directions normal to the zigzag filament and normal to the arched filament, detailed in the next section, was considered. Comparison with the experimental results of the commercial spacer was applied to confirm the result of the CFD simulation and understand its quality. As shown in **Figure 5-14**, when the main flow was normal to the zigzag filament, from the basic concept of laminar flow, except for the region surrounding the arched filament, the flow pattern was similar to that of the conventional partially woven spacer mentioned in many previous works [4]. Moreover, not only the values of velocity and shear stress affect the concentration on the membrane surface; the distribution of shear stress also plays a key role in disrupting the concentration and creating the concentration layer, which was discussed through the contour plot in this study. However, for comprehensive research, the unit energy consumption and average shear stress should be in a rational range. The dimensionless parameter of friction factor and the modified friction factor were applied to enable comparison with the previous study of the commercial spacers.



**Figure 5-14** The geometrical characteristics of the modified feed.

The impact of the modified feed spacer on channel hydraulics was focused on through the construction of a 3D CFD model. There were two steps to the model: (i) The geometry was constructed through comparison with conventional geometries; (ii) the incompressible flow in the laminar flow regime was calculated by using commonly employed parameters (friction factor and modified friction factor).

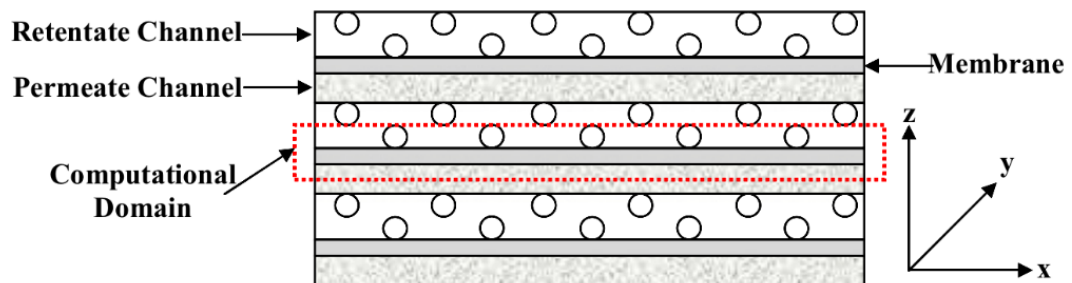
## 5.2 Modeling

To compare different feed spacer characteristics, pressure drop can be expressed in terms of the dimensionless power number and friction factor. The dimensionless power number is generally accepted as a dimensionless parameter to find the situation of energy consumption for different spacer geometries with the same Reynolds number.

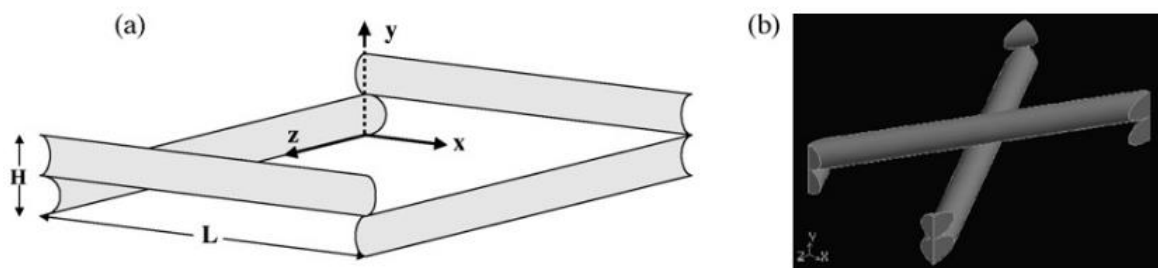
Additionally, the dimensionless power number as a basic parameter is used to compare shear stress, as discussed in the next sections.

### 5.2.1 Characterization of the modified feed Spacer

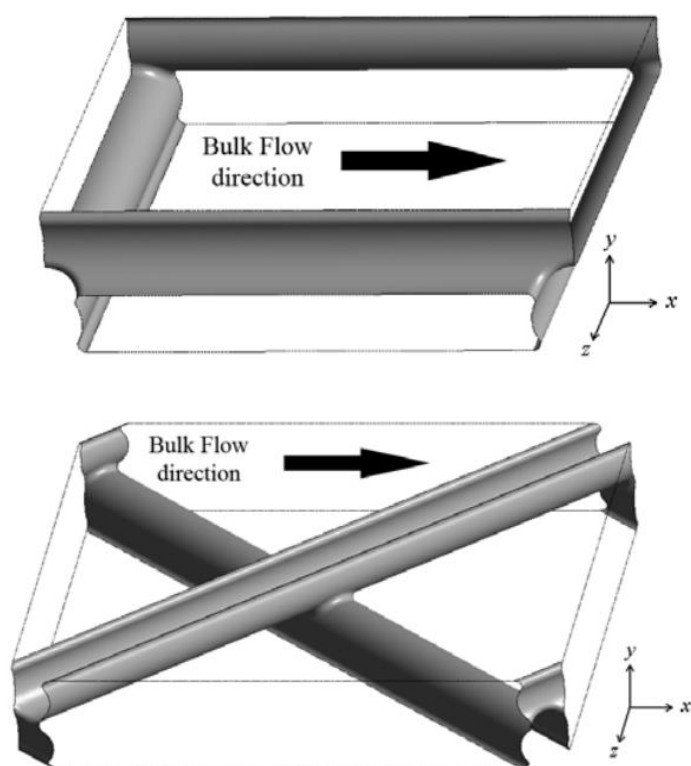
The geometry of this modified feed spacer was described by the feed channel height,  $h_f$ ; the element length (the distance between arched filaments),  $L$ ; and the thickness of the zigzag and arched filaments,  $D$ , which was equal to one-third of the channel height, considering the fabrication possibility,  $D = h_f/3$ . The arched filament was designed as a semicircle, and the distance between the zigzag filaments,  $b$ , was equal to the circle's diameter or twice the channel height,  $b = 2h_f$ , as shown by the three-view diagram in **Figure 5-14** (front view, side view, and vertical view). The feed spacer was characterized by the hydraulic diameter,  $D_H$ , and the porosity or voidage of the feed channel,  $\varepsilon$ . A simplified, cylindrical filament, which, in most of the numerical studies, replaced a realistic spacer, was applied in the present study [14–16].



**Figure 5-15** A view of the representative computational domain, for a stack of flat-sheet membranes, which includes half a retentate and permeate channel with a desalination membrane in-between [14].



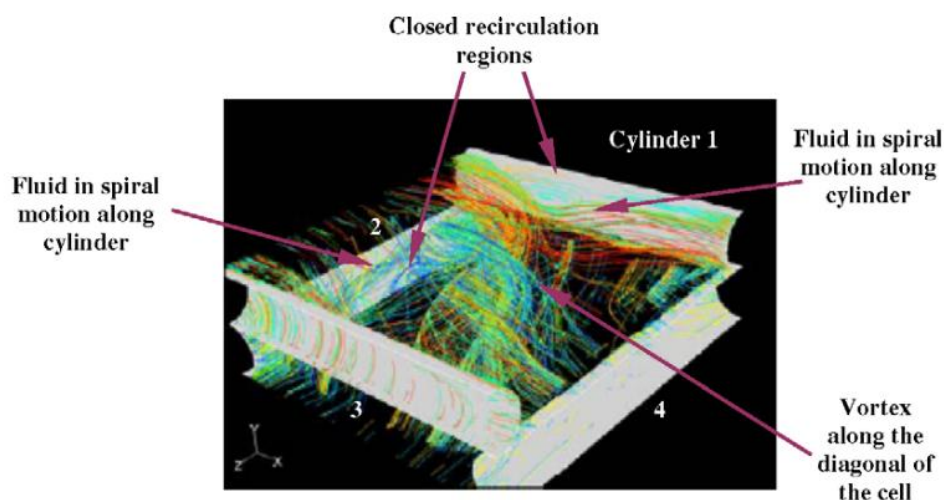
**Figure 5-16** The geometry of the 3D-simulation in Koutsou et al. study [16].



**Figure 5-17**  $90^{\circ}$  and  $45^{\circ}$  orientation of the non-woven spacer filament mesh of Fimbres-Weihs et al. study [15].

The arched filament was between the two walls/membranes and through the bulk region to connect the zigzag filaments, and the zigzag filament contacted the membrane with the line, as shown in **Figure 5-9**. The basic geometrical characteristic is the ratio of the distance between arched filaments to the thickness of cylinder filaments' intersection

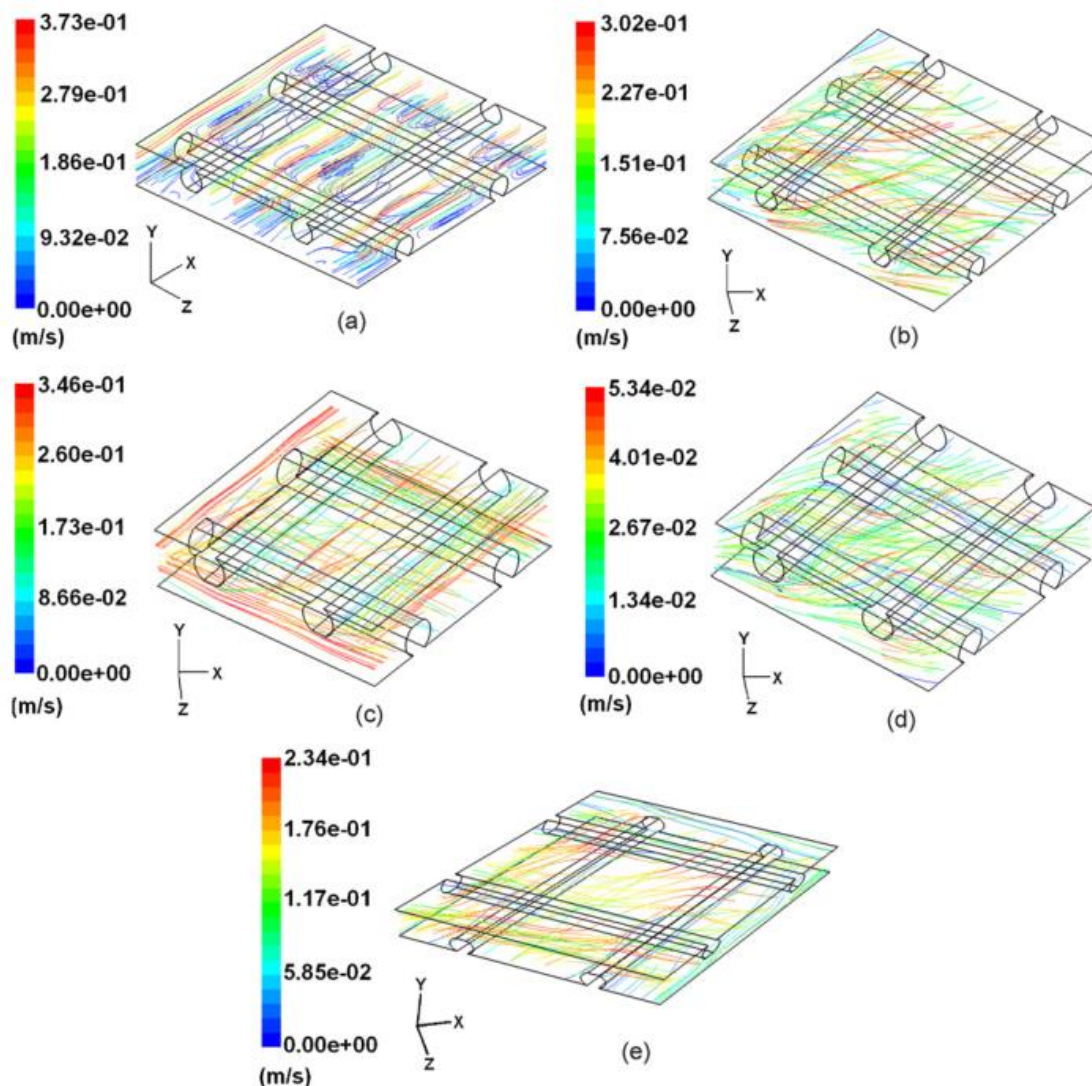
( $L/D$ ), which is related to the channel porosity. This key ratio is employed in defining the element size of common conventional spacers. From the CFD viewpoint, it is convenient to define every simulated unit cell and simulate the respective flow field in detail; thus,  $L/D = 8, 10, 12,$  and  $14$  were employed in the present parameter setting. In addition, Shyam et al. focused on the influence of spacer thickness on permeate flux. Their results showed that when the spacer thickness was from 1.168 to 0.508 mm, the observed flux decreased by up to 50%, and the spacer with a thickness of 0.71 mm was found to be the most economical [5]. In this design,  $D = 0.6$  mm, being close to 0.71 mm, was used.



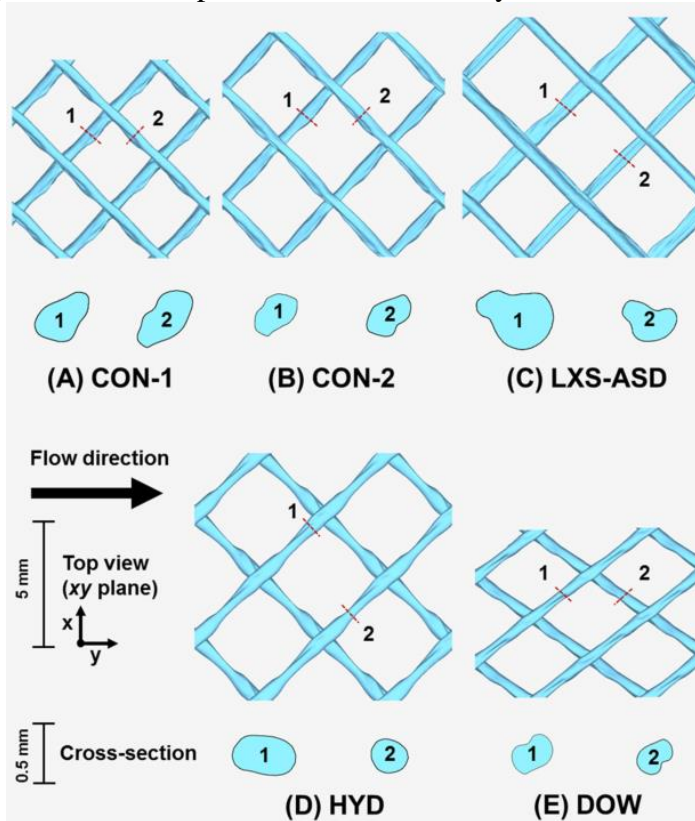
**Figure 5-18** Steady-state fluid particle path lines in Koutsou et al. study [17].

As shown in **Figure 5-2**, the main flow direction was normal to the arched filaments (Case A), and for the comparison of vortex induction, the main flow was set as normal to the zigzag filaments (Case B). It is recognized that the model of CFD simulation is defined by the value of the Reynolds number [17]. For identifying the flow regime, Ranade et al. reported that in most of the spacer-filled channel, the transition from a laminar to turbulent flow regime occurs at Reynolds numbers from 300 to 400 for packed beds

[10]. In the study by Shakaib et al., the simulation for the onset of unsteady flow takes Reynolds number from 100 to 300 [18]. Haaksman et al. observed differences in experimental and model results when the Reynolds number was from 125 to 200 [19]. In the current study, the Reynolds number was from 8 to 150. On the membrane surface, velocity is equal to zero, according to basic fluid theory. In order to clarify flow pattern near the membrane,  $0.05h_f$  and  $0.95h_f$  positions were selected. In addition,  $0.50h_f$  was selected to interpret vortex shedding in the middle of the feed channel.



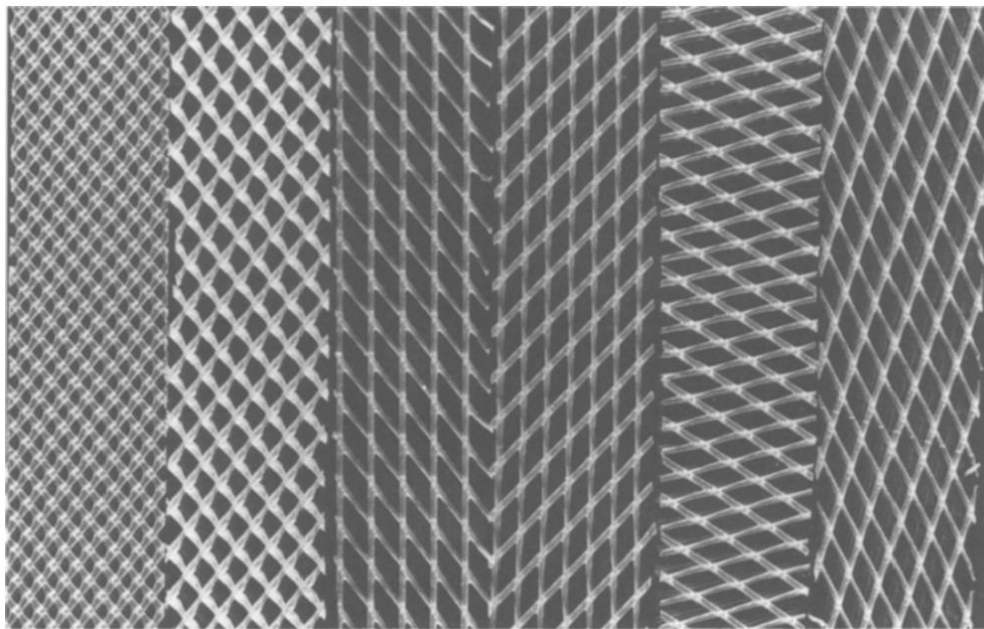
**Figure 5-19** Flow path under different Reynold numbers [18].



**Figure 5-20** CT scans of commercial spacers. The acronyms refer to the spacer manufacturer: Conwed (CON-1, CON-2), LANXESS (LXS-ASD), Hydranautics (HYD) and Dow Chemical (DOW) [19].

Enhancing the efficiency of the membrane module to mitigate fouling is extremely dependent on increasing shear stress at the membrane surface, which is related to the efficacy of the spacers to increase mass transport back to the bulk flow [20]. Wall shear stress,  $\tau$ , is indicated by the relationship of velocity shear rate:  $\tau = \mu du/dy$ . In this study, wall shear stress simulations for different spacer porosity or element length were considered through comparison of shear stress contours and application of the modified friction factor.

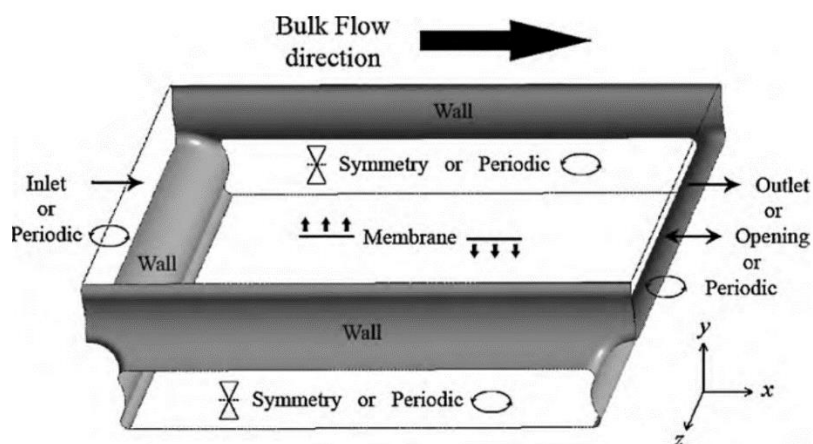




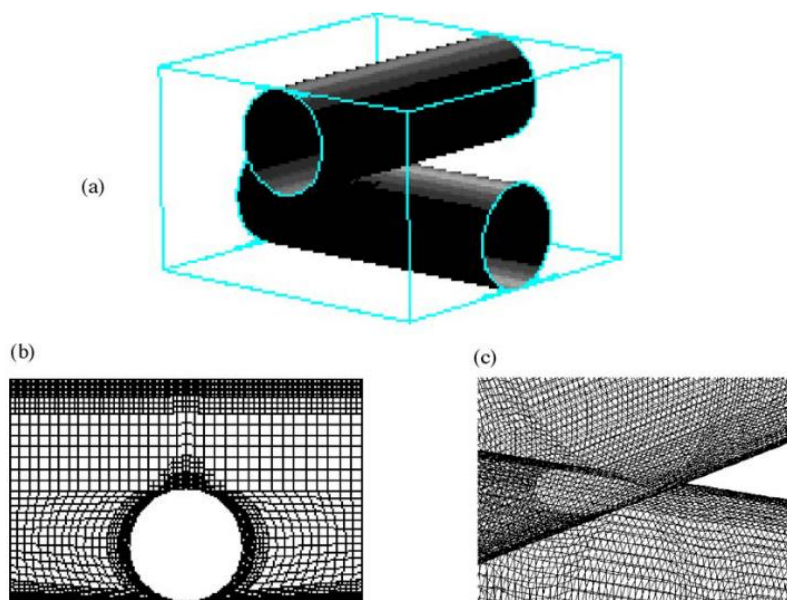
**Figure 5-21** Channel spacer reported by Da Costa, A. R. et al. [20].

## 5.2.2 Model Description

### 5.2.2.1 Computational Domain



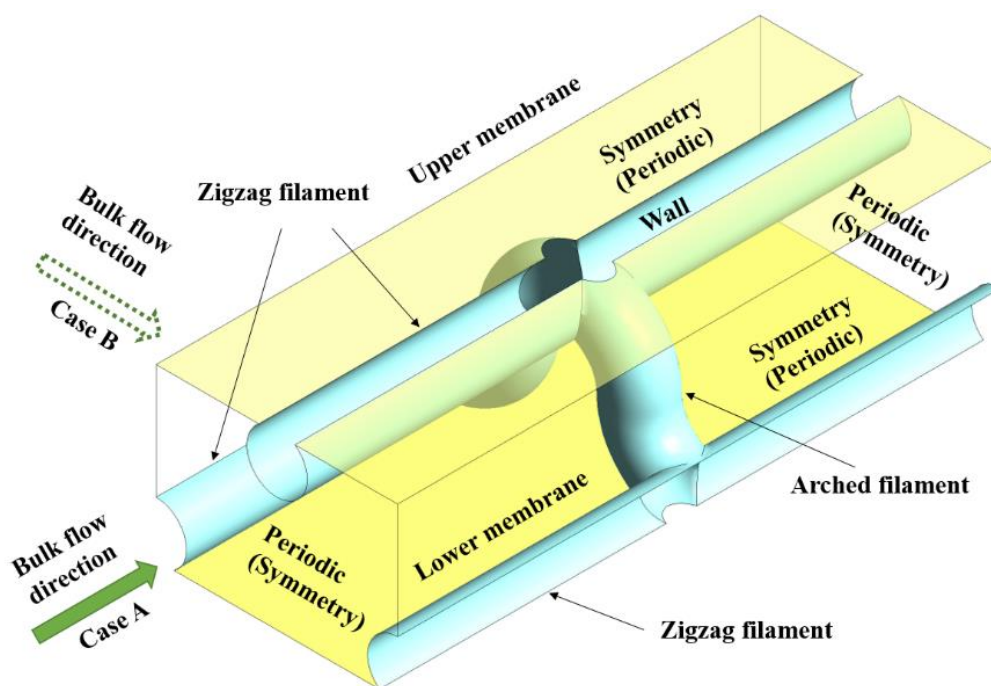
**Figure 5-22** Schematic of a 3D flow domain depicting the locations of the different boundary conditions reported by Fimbres-Weihs, G. A. et al.[21].



**Figure 5-23** Solution domain and computational grid for intersection of spacers [10].

The middle region was chosen as the study region, for the sake of simplicity. An area of an arched filament was in the center of the study region in order to clarify the flow pattern surrounding the filament. In most RO applications, the permeation velocity has no significant effect on the flow structure in the channel, and in industrial membrane processes, the permeate rate is no more than 0.5% of the total cross-flow velocity in the feed channel [22]; for this reason, the membrane and feed spacer surfaces were set as the no-slip boundary condition, the assumption of the nonpermeable wall was adopted, and the velocity of the fluid on the surface was specified as zero in the CFD model. The spacer was explicitly defined as a solid object. The inlet and outlet flow cross sections were set as periodic boundaries [9], and the boundaries between two near elements were set as symmetrical boundaries [21]. The periodic boundary and symmetrical boundary conditions were employed to enable this study to simulate just one cell of the pattern formed by the

modified spacer. Furthermore, in order to clarify the flow pattern for the mixing enhancement, the arched filament was set in the center of the unit cell [10]. In the simulations of case A and case B, the boundary settings were opposite: In case A, when the direction of the bulk flow was normal to the arched filament, the inlet and outlet boundaries were set as period boundaries and modules' connecting boundaries was set as symmetry boundaries. In case B, when the direction of the bulk flow was normal to the zigzag filament, the boundary setting was opposite to that in case A, as detailed in **Figure 5-24**. Considering the scope of the Reynolds number, the standard laminar model was applied following the recommendation in the literature [23] for simulating flows at Reynolds numbers below 150 in a laminar flow regime through a continuous solution. To simplify the simulation, the fluid was assumed to be Newtonian and incompressible at steady state (i.e., no time variations), and no salt source was considered.



**Figure 5-24** CFD (computational fluid dynamics) model setting.

### 5.2.2.2 Simulation of Flow Patterns

The flow of a Newtonian fluid in the spacer-filled channel is modelled by Navier–Stokes and continuity equations. Simulation equations are listed below.

The channel porosity is:

$$\varepsilon = 1 - \frac{V_{Spacer}}{V_{Total}} \quad (11)$$

where  $V_{Spacer}$  is the spacer volume and  $V_{Total}$  is the channel space volume in which the mean flow was separated. The hydraulic channel Reynolds number [24] is:

$$Re = \frac{\rho U_{ave} D_H}{\mu} \quad (12)$$

where  $\rho$  is the water's density.  $U_{ave}$  is the average velocity, which was known as the effective velocity in a previous study [15].  $U_{ave}$  is calculated by dividing the superficial velocity (for the empty channel) by the porosity ( $U_{ave} = U_{sup}/\varepsilon$ ).  $\mu$  is the water's kinematic viscosity. The channel hydraulic diameter, as a geometrical parameter, can be defined as follows for the spacer-filled channel [24]:

$$D_H = \frac{4 \times \text{computational volume}}{\text{wet surface area}} \quad (13)$$

where computational volume is the total volume of the element cell. Wet surface area was included in the surface of the spacer and membrane. Pressure drop can be expressed via the friction factor [25]:

$$f = \frac{\Delta P}{\Delta L} \frac{2D_H}{\rho U_{ave}^2} \quad (14)$$

where  $\Delta P$  is the pressure drop in the channel and  $\Delta L$  is the element length.

The dimensionless power number [17] is calculated as follows:

$$P_n = f R_e^3 \quad (15)$$

Salt rejection of the RO membrane increases with pressure and decreases with salt concentration. In the study by Song et al., their results indicated that the salt concentrations in the regions adjacent to transverse filaments are very much higher than others [26]. Shear stress, as a key parameter, is defined by the velocity gradient, given that the shear stress on the membrane surface is believed to lower concentration polarization and enhance mass transfer. The modified friction factor employed to select the best feed spacer for mass transfer efficiency was used as a means to analyze shear stress on the membrane for comparing the results of four groups with different element length data ( $L/D = 8, 10, 12,$  and  $14$ ) [27].

The modified friction factor for the area average shear stress is represented as [27]:

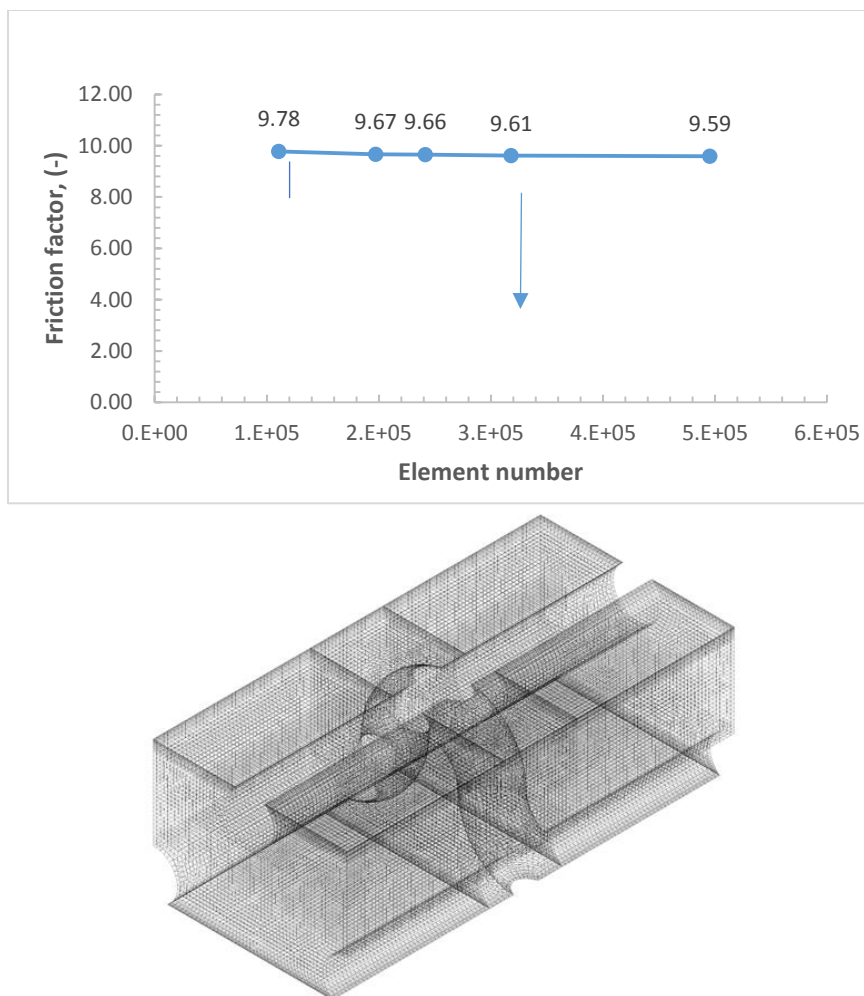
$$f_{wall} = \tau_{wall} \frac{Re^2}{\rho U_{ave}^2} = \tau_{wall} \frac{\rho D_H^2}{\mu^2} \quad (16)$$

where  $\tau_{wall}$  is the average shear stress on the membrane surface.

### 5.2.2.3 Model Solution

Navier–Stokes equations were solved in ANSYS-CFX (v18.1, ANSYS, Inc. Cecil Township, PA, USA. [www.ansys.com](http://www.ansys.com)) with the finite volume method on the hex mesh

generated by the ANSYS-CFX automatic mesh generator. Hex Dominant was applied as the main definition method. According to the literature, the use of hexahedral mesh leads to results being more reliable and closer to the experimental data [10,18,28], since the perfect hexahedral mesh helps to remove the adverse effects of mesh quality variation on different partitions, such as in this study. Gurreri et al. used the same mesh setting in their CFX simulation [29]. The mesh was refined near the membrane surface for the boundary layer simulation and the mesh was expanded smoothly away from the membrane. Various mesh sizes varied from 322,921 to 428,217 min nodes for different cases. The near-wall node on the membrane was at the distance of 0.2 mm. The thickness of the first mesh element layer was 2.5  $\mu\text{m}$ , i.e., below 1% of the channel height [30]. The mesh independence of the solution was checked to make sure that there were sufficient cells in the boundary layer. As indicated in **Figure 5-4**, no significant changes were recorded while meshing the domain with smaller cells. Moreover, the changes of the friction factor were less than 1% [31,32].



**Figure 5-25** Mesh dependence analysis and the adopted mesh for this study.

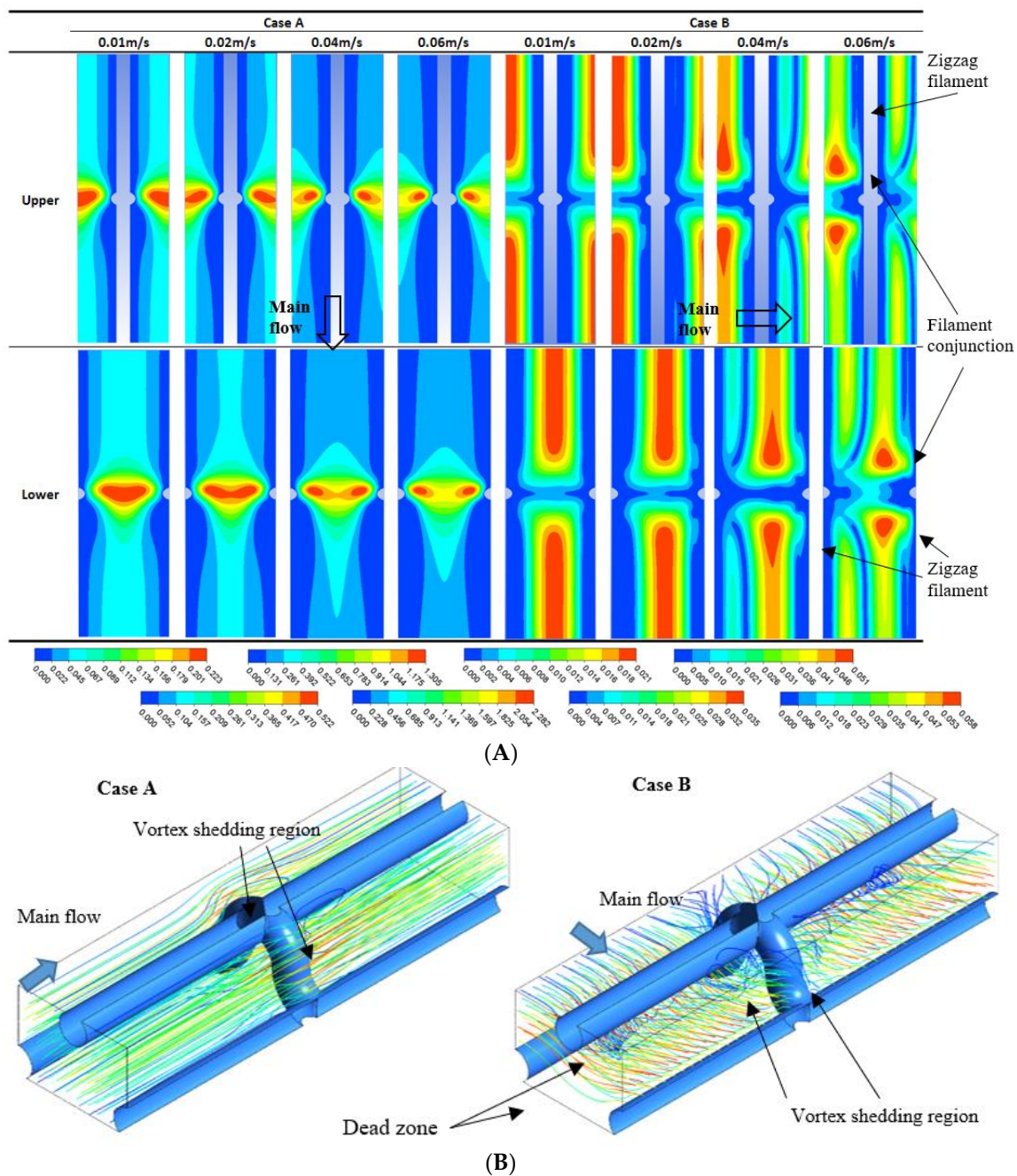
## 5.3 Results and discussion

### 5.3.1 Flow Pattern and Shear Stress Distribution

In the present study, the laminar model has been used, the Reynolds number was up to 150, and the filament spacing was  $L/D = 8, 10, 12,$  and  $14$ . With the purpose of comparing with a commercial spacer, four different flow rates were relayed, with superficial inlet velocities of  $0.01 \text{ m s}^{-1}$ ,  $0.02 \text{ m s}^{-1}$ ,  $0.04 \text{ m s}^{-1}$ , and  $0.06 \text{ m s}^{-1}$  for the

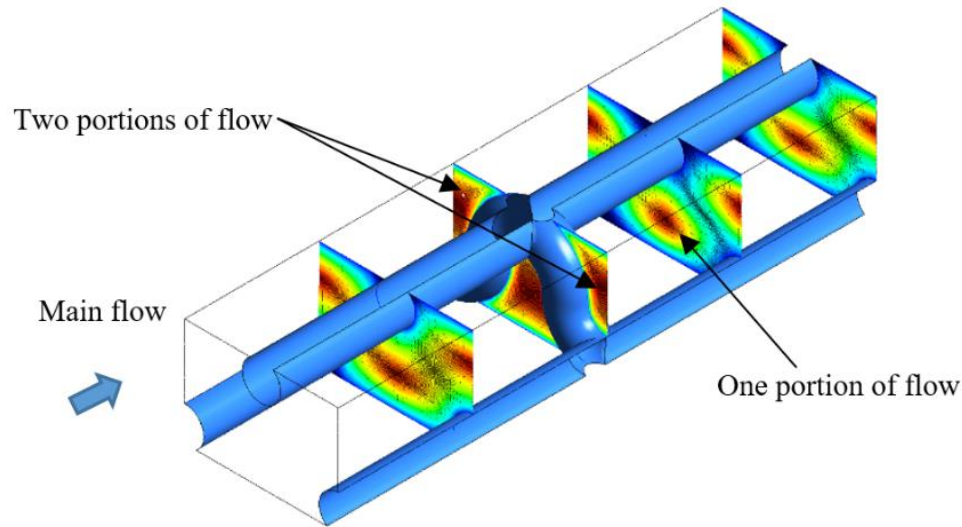
situation where the main flow was normal to the arched filament (when the main flow is vertical to the zigzag filament, the same flow rate was applied, respectively) in the running of the CFD simulation. Through periodic cross-section setting, a fully developed flow can be obtained. In **Figure 5-5A**, the variation of shear stress on the upper and lower membrane surface is shown by a contour plot. **Figure 5-6** shows the velocity vector of the planes in the middle of the channel and in the vicinity of the membranes, for which the position height of the selected planes were 0.05, 0.50, and 0.95 of the channel height for each of case A and case B. In **Figure 5-5A**, three parts of the figure are used to delve into the flow pattern in case A and case B: The middle lower small figure is the location of the selected plane in the unit cell, the left figure is the velocity vector of the selected plane, and the right top small figure is the enlargement of part of the image of the left figure in case A. Furthermore, in **Figures 5-5A** and **5-6**, the value ranges of shear stress and velocity used the default ranges in the CFX-post to clarify the difference for qualitative analysis. The shear stress distribution is closely related to the velocity field, thus **Figures 5-5A** and **5-6** were discussed together. Being beneficial for comparing case A and case B, the ratio,  $L/D = 12$ , was selected for featuring apparently. The mixing enhancement was shown in this subsection by flow (reverse flow, reflecting flow, and difference of velocity) and shear stress (shear stress distribution and control area).





**Figure 5-26** (A) Contour plot ( $L/D = 12$ ) of the average wall shear stress ( $\tau$ ) profile on the upper membrane and lower membrane generated by the spacer; flow was from up to down in case A and flow was from left to right in case B (red: High, blue: Low, unit: Pa); (B) streamline of velocity in case A and case B ( $L/D = 12$ ,  $U_{sup} = 0.06 \text{ m s}^{-1}$ ).

For **Figure 5-5A** upper, the vertical blank in the middle of the contour was the region in which the zigzag filament connected with the membrane surface. From the streamline shown in **Figure 5-5B**, in case B, the main flow cannot reach the zone behind the zigzag filament, hence this corner was called the dead zone, which is mentioned in some conventional woven spacer or nonwoven spacer studies [27,28]. However, for case A, the main flow can flush it directly. The small region in the center of the contour was the conjunction in which the arched filament connects with the zigzag filament. The red contour (maximum value of shear stress) near the conjunction was above the narrow spacer between the membrane and arched filament. For case A (**Figure 5-5B**), the region in which the zigzag filament connected with the membrane surface was located at the vertical boundary of the contour, shown in **Figure 5-5A**. The region was the same as that in the middle vertical region of the contour plot for case A because of the model's simulation of the symmetrical boundary setting. According to these settings, the left half of the region in the upper diagram was same as the right half of the region in the lower diagram, and the right half of the region in the upper diagram was same as the left half of the region in the lower diagram. For case B's upper and lower diagrams, the shear stress contour obeyed the same settings.



**Figure 5-27** Contour plot of velocity in case A ( $L/D = 12$ ,  $U_{sup} = 0.06 \text{ m s}^{-1}$ ).

In case A, the flow can be divided into two portions in the present unit cell: One portion of the flow is in the middle of the arched filament, which was between the arched filament and the lower membrane; another portion of the flow is the symmetrical flow between the arched filament and the upper membrane, pointed out in **Figure 5-6**. Two vortex-shedding regions behind the arched filament were caused by the separation of the flow into two portions and their combining back together at the region near the conjunction of the arched filament and zigzag filament (**Figure 5-5B**). As the streamline of velocity shows in **Figure 5-5B**, the flow continually flushed the dead zone in the vicinity of the region in which the zigzag filament connects with the membrane, forming a line through the two portions of the bulk flow. In **Figure 5-7**, case A, the right top small enlarged figures of  $0.05h_f$  and  $0.95h_f$  show the velocity close to the filament connecting line. This was of benefit to diminish the construction of concentration. In case B, the main flow at the middle of the channel was surrounded by arched filaments, which caused a vortex-shedding region in the arc circle, but for other portions of the flow, was similar with the zigzag configuration

of the conventional nonwoven spacer [22,29]. This is the reason why in case B, a lower porosity or longer element length gave more similar flow patterns to those reported by previous studies for conventional spacers [19,30].

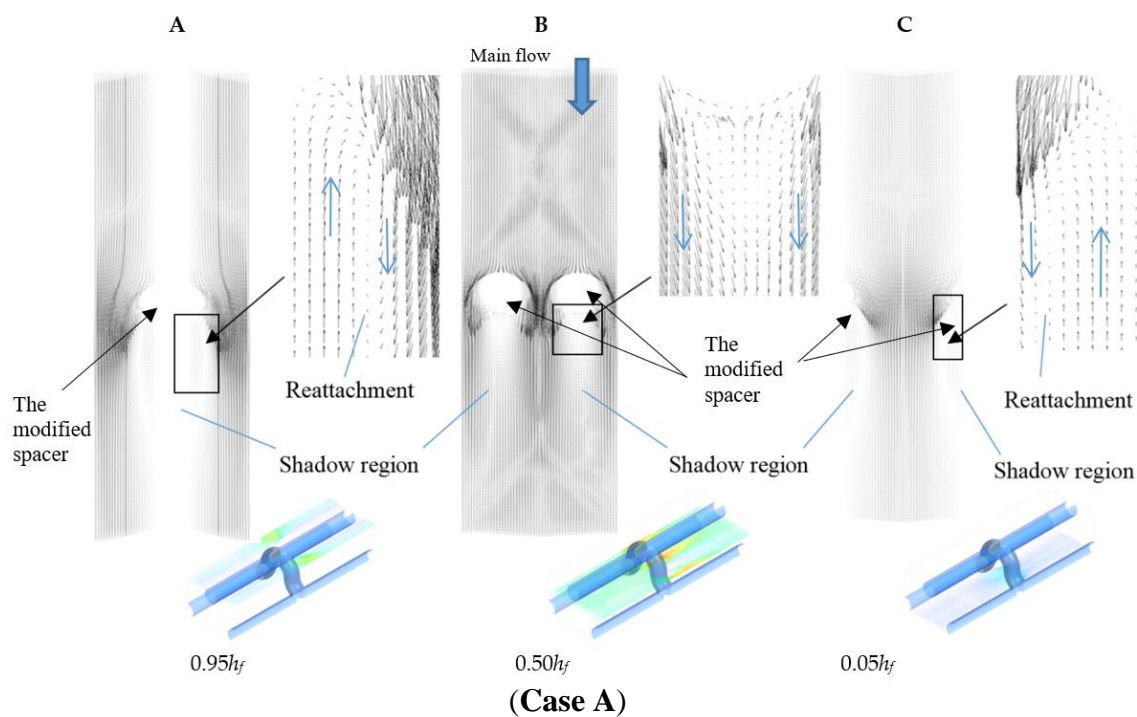
In basic hydrodynamic theory, shear stress represents the velocity gradient in the laminar flow, which was applied in a real process. The variation of the velocity value and direction causes the shear stress to change on a solid surface or in the flow regime. In simulations of conventional woven and nonwoven spacers, because of the impact from the boundary layer in the region near the spacer, the velocity is very small. The shear stress in this region, which was defined from the velocity gradient, was similar to zero, but in the center of the unit cell, the shear stress reaches the maximum value due to higher velocity values. Velocity is high for the flow moving through the narrow cross section, so shear stress is higher on the area of the membrane surface that is in the region above or below filaments; **Figure 5-5A** shows the regions of higher shear stress in red color. In **Figure 5-5A**, case B shows the details of this inclination, which Lau et al. reported in their 2D study [37]. In case A, at the near region in which the filament was connected with the membrane surface, velocity was higher and shear stress reached the maximum value. In the region near the zigzag filament connected with the membrane surface, velocity was the lowest value and shear stress reached the minimum value. In case B, on the upper membrane in the region near the top filament where the line connects with the membrane surface, shear stress was equal to zero, as shown in the middle of the figure, and in the region of the left and right sides of the figure above the bottom filament, velocity was higher and shear stress reached the maximum value. On the lower membrane in the two regions that were near the

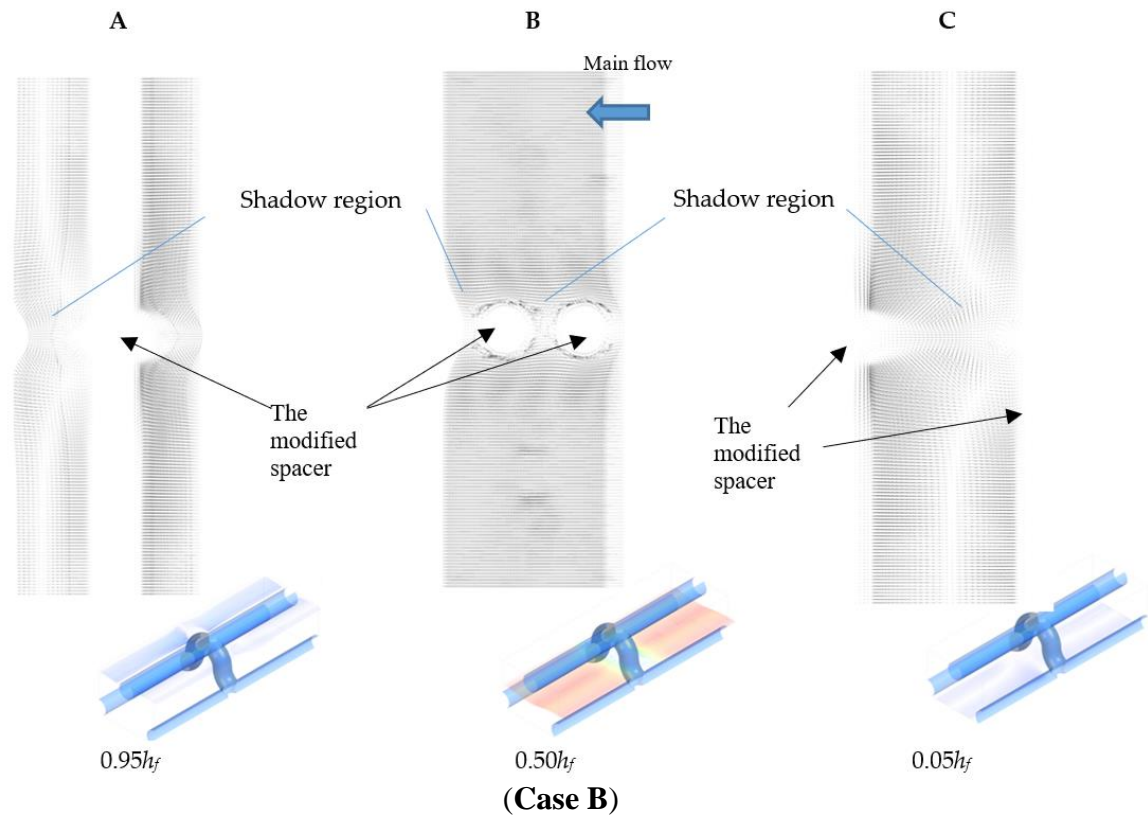
two bottom filaments at the left and right sides of the figure, shear stress was equal to zero, and for the middle of the figure below the top filament, velocity was higher and shear stress reached the maximum value. From the symmetrical boundary setting mentioned in the `Materials and Methods` section, the shear stress distribution on the upper membrane and lower membrane had the same description from different angles. Compared with case B, in case A, the area of low shear stress was smaller. With increasing inlet velocity, the area of the region surrounding the minimum value of shear stress was enhanced, and the area of the region surrounding the maximum value of shear stress was decreased. Shear stress, which increased with velocity, extended to the region near the filaments (in case B, this region was the dead zone indicated by prior studies). The control area was applied to clarify the distribution of shear stress, as shown in **Figure 5-5A**, and the absolute value of shear stress can be checked using the legends. In **Table 5-1**, the ratios of the control area to total membrane area are listed. The control area was the area dominated by the value of shear stress, which was lower and higher than 10% maximum shear stress and 90% maximum shear stress, respectively, for  $L/D = 12$ . In case A, the ratio of low shear stress increased with increasing inlet velocity, but in case B, the ratio of low shear stress decreased with increasing inlet velocity. Laminar vortex shedding was one of the instabilities indicated in the study by Fibers-Weihs et al. [15]. Koutsou et al. focused on the periodic array of cylindrical turbulence promoters in a plane channel, and their result showed that when the cylinder is inserted in the middle of the channel, the flow becomes unstable, with Reynolds numbers beyond 60 [9]. Arched filaments from the upper membrane to the lower membrane were in the middle of the channel, and the Reynolds numbers were in the

laminar flow range. The hydrodynamic boundary layer, which is closely related with permeate flux and fouling processes, was considered for the effect of the instability. In this study, laminar vortex shedding was detailed in **Figure 5-7**; for case A (A and C), it is shown that near the connecting region of the filament joined to the membrane surface, there was a larger affected zone in the down-flow of the feed solution. In the two enlarged images in **Figure 5-7**, between the two flow directions—upward direction and downward direction—there are small arrows, which represent the reflected flow prevented from reattaching to the membrane surface because when the main flow was surrounding the arched filament, the flow direction had a vertical inclination. One portion of the flow was reflected back after striking the membrane surface. The small enlarged images for  $0.05h_f$  and  $0.95h_f$  point out the flow reattachment clearly. In **Figure 5-7**, case A (B), two vortex-shedding zones were developed behind the arched filament in the middle of the feed channel and the flow direction was reversed. From the different vortex-shedding areas in **Figure 5-6**, case A (A), (B), and (C), the 3D vortex-shedding zone behind the arched filament was extrapolated. This 3D zone was from two boundary layers near the membrane and from across the middle main flow zone. The region between the arched filaments was a narrow cross section of the feed flow, and velocity in this region was higher. For this kind of situation, a steeper velocity gradient between the low velocity in the shadow region and the high velocity in the narrowly arched filament region was caused. This flow pattern created by the arched filament directly enhanced mixing. **Figure 5-7** showed the same inclination in case B, but compared with case A, the affected region behind the filament was smaller.

**Table 5-1** The ratio of the control area to total area for the values of shear stress, which are smaller than 10% maximum value or greater than 90% maximum value.

			0.01 m/s	0.02 m/s	0.04 m/s	0.06 m/s
<b>Case A</b>	<b>upper</b>	smaller	23.916%	29.274%	37.002%	42.018%
		greater	2.056%	1.605%	0.758%	0.552%
	<b>lower</b>	smaller	23.855%	29.099%	36.751%	41.720%
		greater	2.093%	1.753%	0.814%	0.572%
<b>Case B</b>	<b>upper</b>	smaller	33.544%	35.614%	29.087%	23.815%
		greater	13.788%	12.603%	4.015%	1.937%
	<b>lower</b>	smaller	33.427%	35.987%	29.285%	23.635%
		greater	13.954%	13.133%	3.838%	1.815%





**Figure 5-28** Velocity vectors in case A and case B ( $L/D = 12$ ,  $U_{sup} = 0.06 \text{ m s}^{-1}$ ; in (case A), the main flow was from up to down, and in (case B), the main flow was from right to left for (A)  $0.95h_f$ , (B)  $0.50h_f$ , and (C)  $0.05h_f$ .

### 5.3.2 Validation of Arc-like spacer Simulation

#### 5.3.2.1 Pressure drop and Friction Factor

An unavoidable phenomenon in SW membrane channel pressure drop directly reduces the total transmembrane pressure which acts on the membrane surface. Driven pump have to maintain the transmembrane pressure, so in separation process higher energy is required to compensate the energy loss which is critically influenced by these pressure loss. The viscous drag on the feed channel walls and feed spacer, form drag of the feed



spacer and kinetic losses determine pressure drop through directional flow changing in a spacer-filled channel [38]. Average velocity influences the flow change. A.R. Da Costa et al.[20] reported the relationship between pressure and average velocity and given out the parameter “m” resulted in laminar and turbulent flow.

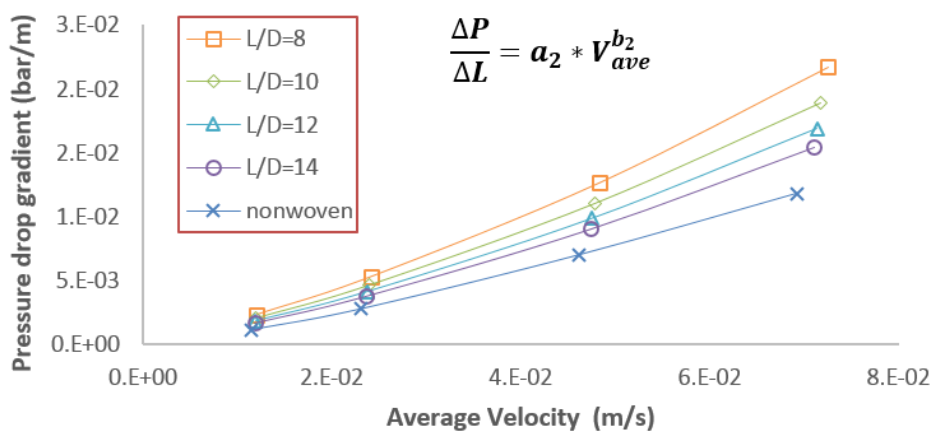
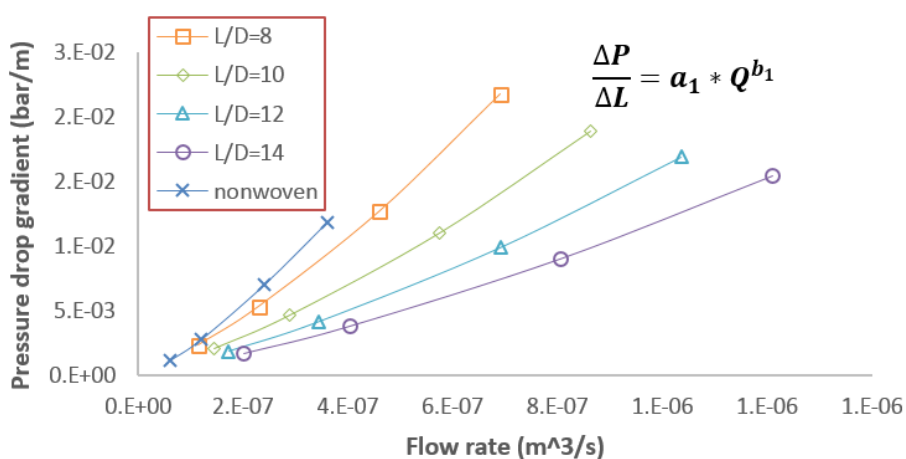
$$\Delta P \propto u^m \quad (10)$$

In this study, the pressure drop per unit channel length effected by flow rate ( $Q = U_{super} \times h \times b$ ) and average velocity increasing as deduced in **Figure 5-29** and **Figure 5-30**. A.H. Haidari et al. compared pressure drop in spacer-filled and empty channel [39]. Their results were listed in **Table 5-2** and **Table 5-3**. The pressure drop increased with flow rate and average velocity. When flow direction was vertical to arched filament pressure drop was smaller than nonwoven spacer in relation of flow rate, but a little bit larger than nonwoven spacer in relation of average velocity. When flow direction was vertical to zigzag filament pressure drop was smaller than nonwoven spacer in relation of flow rate and average velocity. The changing trends of the pressure drop gradient were simulated with A.H. Haidari et al. results. The values of equation parameter were between the spacer-filled channel and empty channel. Different element length means the different porosity of feed channel. Higher porosity costs more driving energy or causes more kinetic loss from the spacer drag. The higher porosity or smaller element length was accelerated the gradual increase of pressure drop. This trend was same to the previous studies of porosity of feed channel [38,40]. **Figure 5-31** showed the trend of pressure drop as a function of the Reynolds number, the value of pressure drop was higher than nonwoven spacer. The effect of porosity is smaller when main flow was vertical to the zigzag filament.

The arched filament from upper membrane to lower membrane in the middle of feed channel was similar conventional submerge configuration, higher energy consumption was like Arun Subramani et al. conclusion [41].

**Table 5-2** The pressure drop function parameters for case A.

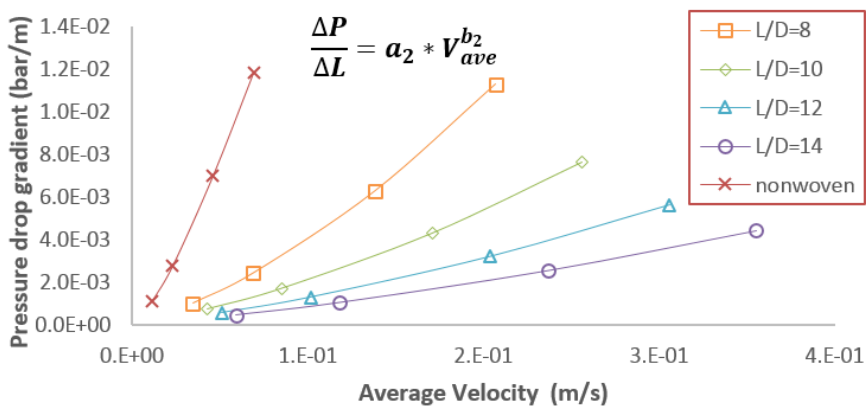
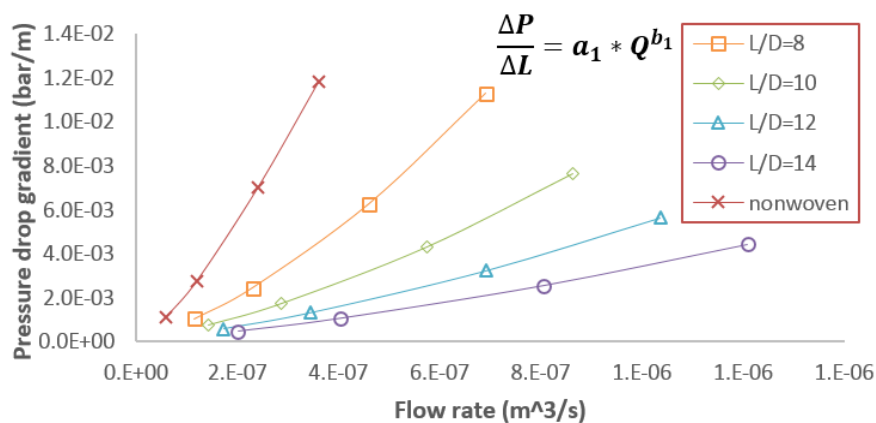
	a1	b1	a2	b2
L/D=8	9.93E+05	1.24	0.56	1.24
L/D=10	6.24E+05	1.24	0.49	1.24
L/D=12	4.02E+05	1.23	0.43	1.23
L/D=14	2.78E+05	1.23	0.39	1.23
nonwoven	3.00E+06	1.31	0.39	1.31
A.H. Haidar spacer	1,77E+08	1.63	7.91	1.63
A.H. Haidar channel	5384	0.97	0.23	0.97



**Figure 5-29** The pressure drop for case A, associated with the element length, as a function of the flow rate and average velocity.

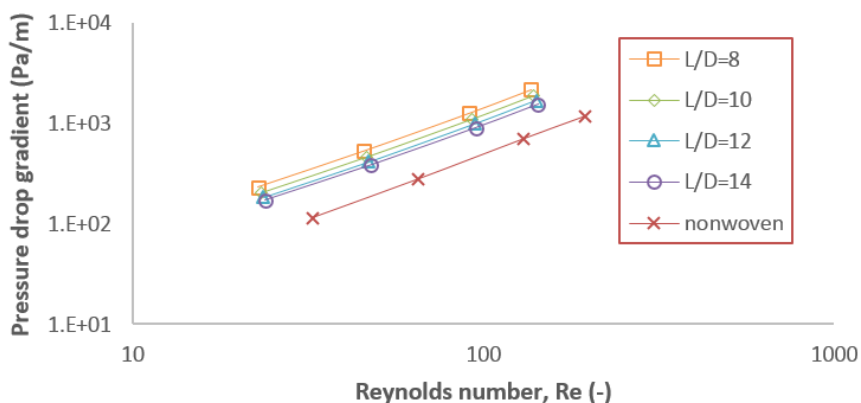
**Table 5-3** The pressure drop function parameters for case B.

	a1	b1	a2	b2
L/D=8	2.00E+06	1.33	0.09	1.33
L/D=10	5.22E+05	1.29	0.04	1.29
L/D=12	2.00E+05	1.26	0.02	1.26
L/D=14	9.23E+04	1.24	0.02	1.24
nonwoven	3.00E+06	1.31	0.39	1.31
A.H. Haidar spacer	1,77E+08	1.63	7.91	1.63
A.H. Haidar channel	5384	0.97	0.23	0.97

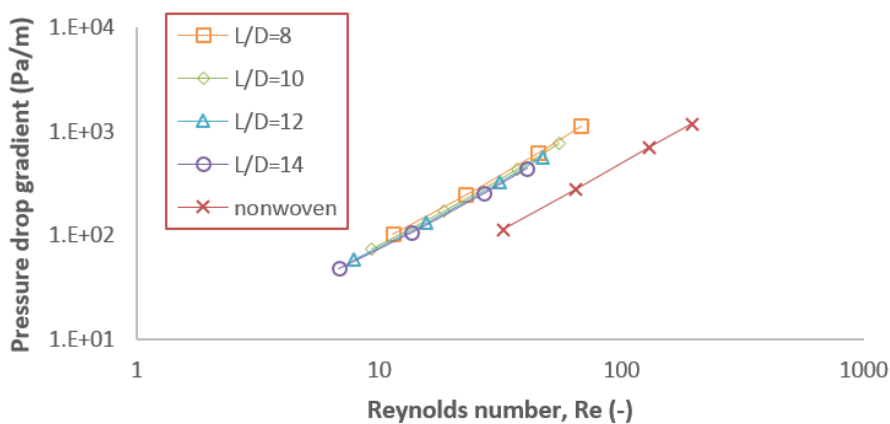


**Figure 5-30** The pressure drop for case B, associated with the element length, as a function of the flow rate and average velocity

(A)



(B)



**Figure 5-31** The pressure drop gradient of (A) main flow was vertical to arched filament and (B) main flow was vertical to zigzacc filament, associated with the element length, as a function of the Reynolds number.

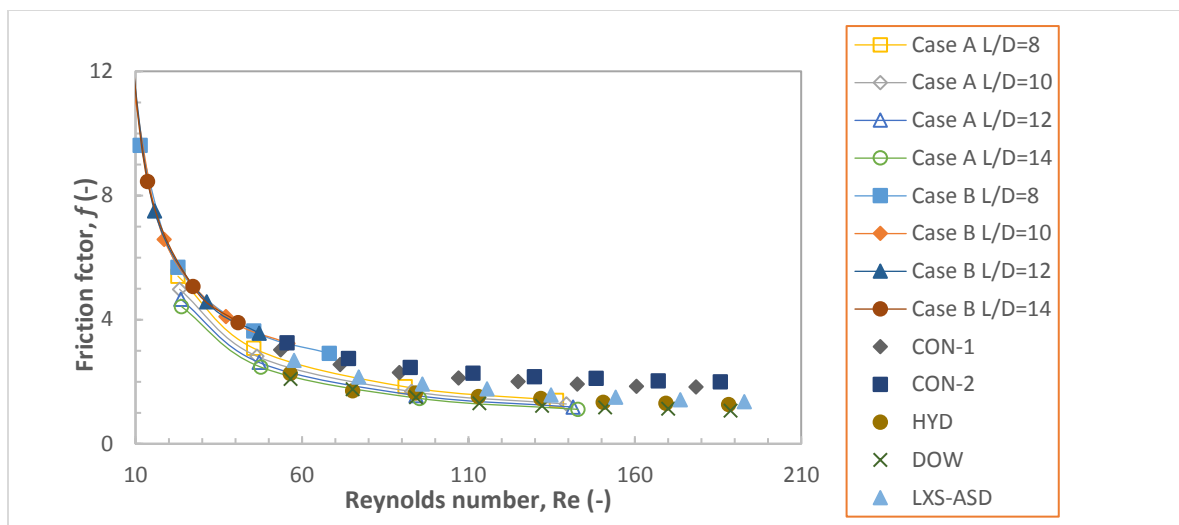
**Figure 5-32** indicates the general agreement on the inclination of the friction factor to decrease with an increasing Reynolds number, as shown in the present study [42]. Five kinds of commercial spacers from the study by Haaksman et al. were added for comparison,

which were available from Conwed Plastics (Minneapolis, USA), Hydranautics (California, USA), DOW Chemical (Michigan, USA), and Lanxess AG (Cologne, Germany), and were surveyed by the accurate 3D geometry obtained from X-ray computed tomography scans [19]. CON-2 produced the maximum value, and the DOW spacer gave the minimum value. For case B, the difference of the friction factor results between the four groups of different  $L/D$  ratios was small; however, the values were almost similar to that of CON-2. The value of case A  $L/D = 14$  was lower than for DOW. The same mass flow rate was applied in case A and case B and the hydraulic diameter was the same, but the cross section of the feed channel was larger in case B. This is the reason why the two flow directions had two different ranges of Reynolds numbers, and the range of Reynolds numbers was smaller in case B. In the two cases, the cause of differentiated curves was different porosity or element length; a different  $L/D$  ratio means different channel porosity. Friction factor values were higher when porosity was lower (element length was lower), but the amplitude became gradually smaller. This inclination was the same as reported in previous studies of feed channel porosity [33,34]. The effect of porosity in case A was higher than in case B due to separate inclination lines or the larger difference. Friction factor was higher in case B; when the main flow was vertical to the zigzag filament, higher pressure loss was caused by the longer transverse filament. This result cannot be detailed quantitatively without the simulation of every part of the spacer structure, which was outside the scope of this study. However, it yielded to the reason that given the same filament thickness for the filament length facing the flow direction, which decided the viscous drag from the spacer zigzag filament, it is longer than the arched filament. Haidari

et al. reported that comparing with an empty channel feed spacer, it caused a greater pressure drop [39]. Additionally, based on basic hydrodynamic theory, the difference of pressure loss means a different dead zone behind the spacer filament. The difference of the friction factor in case A was higher than in case B, therefore, the effect from the arched filament on flow characteristics was more significant than that from the zigzag filament. This inclination revealed that having more traverse filaments caused more energy consumption, agreeing with previous studies, and this study's results on the matter are listed in **Table 5-4** by applying the specific power consumption (SPC) ( $\equiv(\Delta P/L)U_{ave}$ , Pa  $s^{-1}$ ), which indicates the mechanical power consumption dissipated per cubic meter [44]. Through comparison with the study by Haaskmen et al., which was concluded by X-ray computed tomography [19], in case A, the value of the friction factor was smaller than their results and was similar with the HYD result. In case B, the value was a little bit higher than their result and was similar with the CON-2 result when the Reynolds number was close to 60, for which agreement of the value is provided by the study by Koutsou et al. [9].

**Table 5-4** Interpolated value from fixed superficial velocity at Reynolds number 40.

		Channel porosity	SPC(Pa/s)
Case A	L/D=8	0.828	10.399
	L/D=10	0.835	8.663
	L/D=12	0.841	7.554
	L/D=14	0.845	6.802
Case B	L/D=8	0.828	69.736
	L/D=10	0.835	92.111
	L/D=12	0.841	124.068
	L/D=14	0.845	151.636



**Figure 5-32** Comparison with the friction factor result of Haaksman et al. [9] as a function of Reynolds number.

### 5.3.2.2 The Modified Friction Factor

This subsection underlines the average value of shear stress on the upper and lower membrane surfaces after the discussion of shear stress distribution. The numerical dimensionless parameter, by applying the modified friction factor, was employed to enable comparison with previous works and confirm the value in the rational range. **Figure 5-33** shows the comparison with the previous study for a commercial spacer model [19]. In order to compare the values of shear stress with other spacer geometries, the modified friction factor as a dimensionless parameter was computed from the plot shown in **Figure 5-9**. As a function of the dimensionless power number, the modified friction factor is shown in Equation (6). The modified friction factor increased with the dimensionless power number in case A and case B. The difference of the modified friction factor was small at the same dimensionless power number, hence the effect of the  $L/D$  ratio or porosity on the average





**Figure 5-33** Comparison with the result of Haaksman et al. [9] in the commercial spacer simulation for the modified friction factor as a function of the dimensionless power number.

#### 5.4 Conclusion

To achieve enhanced mixing, the modified feed spacer was designed as the transversal filament from the upper membrane to the lower membrane. This structure changed the flow patterns in the total feed channel compared with the conventional spacer. Reduction of the shadow zone behind the transversal filament was realized with the arched filament, and the potential for mixing reached to the close vicinity of the filament.

Here, a CFD simulation result of the arc-like spacer was presented. Under laminar flow conditions, the element of the feed spacer between membrane envelopes was simulated. Subsequently, the geometry parameters of the arc-like spacer and this simulation's parameter values were compared with previous works and validated. The results revealed the detailed flow pattern and shear stress distribution. The main research findings revealed that:

- When the main flow was normal to the arched filament, the area of the dead zone behind the zigzag filament, which was connected with the membrane, decreased with an increasing Reynolds number. In addition, the zone of vortex shedding behind the arched filament caused different flow fields, which generated a high gradient of velocity, improving the mixing of the feed solution.

- The investigated data of power consumption (friction factor) was approximated to the conventional commercial spacer. The value was a little lower than the commercial spacer at high Reynolds numbers when the main flow was normal to the arched filament. From comparison with previous work, it can be extrapolated that the changing of flow patterns from the structure of the arc-like spacer did not cause too much energy consumption.
- The value of the modified friction factor as a dimensionless number was similar to the results of previous work on commercial spacers when the main flow was normal to the arched filament.
- The effect of porosity (element length) on the energy consumption of the arc-like spacer was in agreement with previous studies, but on shear stress, was smaller. This conclusion was indicated by result lines qualitatively.

## Reference

1. Jamaly, S.; Darwish, N. N.; Ahmed, I.; Hasan, S. W. A short review on reverse osmosis pretreatment technologies. *Desalination* 2014, 354, 30–38.
2. Tamburini, A.; La Barbera, G.; Cipollina, A.; Ciofalo, M.; Micale, G. CFD simulation of channels for direct and reverse electrodialysis. *Desalin. Water Treat.* **2012**, 48, 370–389, doi:10.1080/19443994.2012.705084.
3. Lee, J. Y.; Tan, W. S.; An, J.; Chua, C. K.; Tang, C. Y.; Fane, A. G.; Chong, T. H. The potential to enhance membrane module design with 3D printing technology. *J. Memb. Sci.* **2016**, 499, 480–490, doi:10.1016/j.memsci.2015.11.008.
4. Gu, B.; Adjiman, C. S.; Xu, X. Y. The effect of feed spacer geometry on membrane performance and concentration polarisation based on 3D CFD simulations. *J. Memb. Sci.* **2017**, 527, 78–91, doi:10.1016/j.memsci.2016.12.058.
5. Sablani, S. S.; Goosen, M. F. A.; Al-Belushi, R.; Gerardos, V. Influence of spacer thickness on permeate flux in spiral-wound seawater reverse osmosis systems. *Desalination* **2002**, 146, 225–230, doi:10.1016/S0011-9164(02)00477-0.
6. Radu, A. I.; Vrouwenvelder, J. S.; van Loosdrecht, M. C. M.; Picioreanu, C.; Posadzy-Malaczyńska, A.; Kosch, M.; Hausberg, M.; Rahn, K. H.; Stanisic, G.; Malaczynski, P.; Gluszek, J.; Tykarski, A.; Radu, A. I.; Vrouwenvelder, J. S.; van Loosdrecht, M. C. M.; Picioreanu, C. Effect of flow velocity, substrate concentration and hydraulic cleaning on biofouling of reverse osmosis feed channels. *Chem. Eng. J.* **2012**, 188, 30–39, doi:10.1016/j.cej.2012.01.133.
7. Bucs, S. S.; Valladares Linares, R.; Marston, J. O.; Radu, A. I.; Vrouwenvelder, J.

- S.; Picioreanu, C. Experimental and numerical characterization of the water flow in spacer-filled channels of spiral-wound membranes. *Water Res.* **2015**, *87*, 299–310, doi:10.1016/j.watres.2015.09.036.
8. Bucs, S.; Farhat, N.; Kruithof, J. C.; Picioreanu, C.; van Loosdrecht, M. C. M.; Vrouwenvelder, J. S. Review on strategies for biofouling mitigation in spiral wound membrane systems. *Desalination* **2018**, *434*, 189–197, doi:10.1016/j.desal.2018.01.023.
  9. Koutsou, C. P.; Yiantsios, S. G.; Karabelas, A. J. Numerical simulation of the flow in a plane-channel containing a periodic array of cylindrical turbulence promoters. *J. Memb. Sci.* **2004**, *231*, 81–90, doi:10.1016/j.memsci.2003.11.005.
  10. Ranade, V. V.; Kumar, A. Fluid dynamics of spacer filled rectangular and curvilinear channels. *J. Memb. Sci.* **2006**, *271*, 1–15, doi:10.1016/j.memsci.2005.07.013.
  11. Liu, J.; Liu, Z.; Xu, X.; Liu, F. Saw-tooth spacer for membrane filtration: Hydrodynamic investigation by PIV and filtration experiment validation. *Chem. Eng. Process. Process Intensif.* **2015**, *91*, 23–34, doi:10.1016/j.cep.2015.03.013.
  12. Cao, Z.; Wiley, D. E.; Fane, A. G. CFD simulations of net-type turbulence promoters in a narrow channel. *J. Memb. Sci.* **2001**, *185*, 157–176, doi:10.1016/S0376-7388(00)00643-8.
  13. Fernández-Sempere, J.; Ruiz-Beviá, F.; García-Algado, P.; Salcedo-Díaz, R. Experimental study of concentration polarization in a crossflow reverse osmosis system using Digital Holographic Interferometry. *Desalination* **2010**, *257*, 36–45,

doi:10.1016/j.desal.2010.03.010.

14. Karabelas, A. J.; Kostoglou, M.; Koutsou, C. P. Modeling of spiral wound membrane desalination modules and plants - review and research priorities. *Desalination* **2015**, *356*, 165–186, doi:10.1016/j.desal.2014.10.002.
15. Fimbres-Weihs, G. A.; Wiley, D. E. Numerical study of mass transfer in three-dimensional spacer-filled narrow channels with steady flow. *J. Memb. Sci.* **2007**, *306*, 228–243, doi:10.1016/j.memsci.2007.08.043.
16. Koutsou, C. P.; Yiantsios, S. G.; Karabelas, A. J. A numerical and experimental study of mass transfer in spacer-filled channels: Effects of spacer geometrical characteristics and Schmidt number. *J. Memb. Sci.* **2009**, *326*, 234–251, doi:10.1016/j.memsci.2008.10.007.
17. Koutsou, C. P.; Yiantsios, S. G.; Karabelas, A. J. Direct numerical simulation of flow in spacer-filled channels: Effect of spacer geometrical characteristics. *J. Memb. Sci.* **2007**, *291*, 53–69, doi:10.1016/j.memsci.2006.12.032.
18. Shakaib, M.; Hasani, S. M. F.; Mahmood, M. Study on the effects of spacer geometry in membrane feed channels using three-dimensional computational flow modeling. *J. Memb. Sci.* **2007**, *297*, 74–89, doi:10.1016/j.memsci.2007.03.010.
19. Haaksman, V. A.; Siddiqui, A.; Schellenberg, C.; Kidwell, J.; Vrouwenvelder, J. S.; Picioreanu, C. Characterization of feed channel spacer performance using geometries obtained by X-ray computed tomography. *J. Memb. Sci.* **2017**, *522*, 124–139, doi:10.1016/j.memsci.2016.09.005.
20. Da Costa, A. R.; Fane, A. G.; Fell, C. J. D.; Franken, A. C. M. Optimal channel

- spacer design for ultrafiltration. *J. Memb. Sci.* **1991**, *62*, 275–291, doi:10.1016/0376-7388(91)80043-6.
21. Fimbres-Weihs, G. A.; Wiley, D. E. Review of 3D CFD modeling of flow and mass transfer in narrow spacer-filled channels in membrane modules. *Chem. Eng. Process. Process Intensif.* **2010**, *49*, 759–781, doi:10.1016/j.cep.2010.01.007.
  22. Ma, S.; Song, L. Numerical study on permeate flux enhancement by spacers in a crossflow reverse osmosis channel. *J. Memb. Sci.* **2006**, *284*, 102–109, doi:10.1016/j.memsci.2006.07.022.
  23. Hayes, R. E. *Computational flow modeling for chemical reactor engineering*; 2002; Vol. 80; ISBN 0125769601.
  24. Schock, G.; Miquel, A. Mass transfer and pressure loss in spiral wound modules. *Desalination* **1987**, *64*, 339–352, doi:10.1016/0011-9164(87)90107-X.
  25. Geraldes, V.; Semião, V.; De Pinho, M. N. Flow management in nanofiltration spiral wound modules with ladder-type spacers. *J. Memb. Sci.* **2002**, *203*, 87–102, doi:10.1016/S0376-7388(01)00753-0.
  26. Song, L.; Ma, S. Numerical studies of the impact of spacer geometry on concentration polarization in spiral wound membrane modules. *Ind. Eng. Chem. Res.* **2005**, *44*, 7638–7645, doi:10.1021/ie048795w.
  27. Santos, J. L. C.; Geraldes, V.; Velizarov, S.; Crespo, J. G. Investigation of flow patterns and mass transfer in membrane module channels filled with flow-aligned spacers using computational fluid dynamics (CFD). *J. Memb. Sci.* **2007**, *305*, 103–117, doi:10.1016/j.memsci.2007.07.036.

28. Schwinge, J.; Wiley, D. E.; Fletcher, D. F. Simulation of the flow around spacer filaments between narrow channel walls. 1. Hydrodynamics. *Ind. Eng. Chem. Res.* **2002**, *41*, 2977–2987, doi:10.1021/ie010588y.
29. Gurreri, L.; Tamburini, A.; Cipollina, A.; Micale, G. CFD analysis of the fluid flow behavior in a reverse electrodialysis stack. *Desalin. Water Treat.* **2012**, *48*, 390–403, doi:10.1080/19443994.2012.705966.
30. Lim, S. Y.; Liang, Y. Y.; Fimbres Weihs, G. A.; Wiley, D. E.; Fletcher, D. F. A CFD study on the effect of membrane permeance on permeate flux enhancement generated by unsteady slip velocity. *J. Memb. Sci.* **2018**, *556*, 138–145, doi:10.1016/j.memsci.2018.03.070.
31. Kavianipour, O.; Ingram, G. D.; Vuthaluru, H. B. Investigation into the effectiveness of feed spacer configurations for reverse osmosis membrane modules using Computational Fluid Dynamics. *J. Memb. Sci.* **2017**, *526*, 156–171, doi:10.1016/j.memsci.2016.12.034.
32. Blocken, B.; Gualtieri, C. Ten iterative steps for model development and evaluation applied to Computational Fluid Dynamics for Environmental Fluid Mechanics. *Environ. Model. Softw.* **2012**, *33*, 1–22, doi:10.1016/j.envsoft.2012.02.001.
33. Saeed, A.; Vuthaluru, R.; Vuthaluru, H. B. Impact of Feed Spacer Filament Spacing on Mass Transport and Fouling Propensities of RO Membrane Surfaces. *Chem. Eng. Commun.* **2015**, *202*, 634–646, doi:10.1080/00986445.2013.860525.
34. Haidari, A. H.; Heijman, S. G. J.; van der Meer, W. G. J. Effect of spacer configuration on hydraulic conditions using PIV. *Sep. Purif. Technol.* **2018**, *199*, 9–

- 19, doi:10.1016/j.seppur.2018.01.022.
35. Schwinge, J.; Wiley, D. E.; Fletcher, D. F. Simulation of the Flow around Spacer Filaments between Channel Walls. 2. Mass-Transfer Enhancement. *Ind. Eng. Chem. Res.* **2002**, *41*, 4879–4888, doi:10.1021/ie011015o.
36. Saeed, A.; Vuthaluru, R.; Vuthaluru, H. B. Investigations into the effects of mass transport and flow dynamics of spacer filled membrane modules using CFD. *Chem. Eng. Res. Des.* **2015**, *93*, 79–99, doi:10.1016/j.cherd.2014.07.002.
37. Lau, K. K.; Abu Bakar, M. Z.; Ahmad, A. L.; Murugesan, T. Effect of feed spacer mesh length ratio on unsteady hydrodynamics in 2d spiral wound membrane (swm) channel. *Ind. Eng. Chem. Res.* **2010**, *49*, 5834–5845, doi:10.1021/ie9017989.
38. Da Costa, A. R.; Fane, A. G.; Wiley, D. E. Spacer characterization and pressure drop modelling in spacer-filled channels for ultrafiltration. *J. Memb. Sci.* **1994**, *87*, 79–98, doi:10.1016/0376-7388(93)E0076-P.
39. Haidari, A. H.; Heijman, S. G. J.; van der Meer, W. G. J. Visualization of hydraulic conditions inside the feed channel of Reverse Osmosis: A practical comparison of velocity between empty and spacer-filled channel. *Water Res.* **2016**, *106*, 232–241, doi:10.1016/j.watres.2016.10.012.
40. Siddiqui, A.; Lehmann, S.; Haaksman, V.; Ogier, J.; Schellenberg, C.; van Loosdrecht, M. C. M.; Kruithof, J. C.; Vrouwenvelder, J. S. Porosity of spacer-filled channels in spiral-wound membrane systems: Quantification methods and impact on hydraulic characterization. *Water Res.* **2017**, *119*, 304–311, doi:10.1016/j.watres.2017.04.034.



41. Subramani, A.; Kim, S.; Hoek, E. M. V Pressure, flow, and concentration profiles in open and spacer-filled membrane channels. *J. Memb. Sci.* **2006**, *277*, 7–17, doi:10.1016/j.memsci.2005.10.021.
42. Zimmerer, C. C.; Kottke, V. Effects of spacer geometry on pressure drop, mass transfer, mixing behavior, and residence time distribution. *Desalination* **1996**, *104*, 129–134, doi:10.1016/0011-9164(96)00035-5.
43. Da Costa, A. R.; Fane, A. G.; Wiley, D. E. Spacer characterization and pressure drop modeling in spacer-filled channels.pdf. *J. Memb. Sci.* **1994**, *87*, 79–98, doi:10.1016/0376-7388(93)E0076-P.
44. Li, F.; Meindersma, W.; De Haan, A. B.; Reith, T. Experimental validation of CFD mass transfer simulations in flat channels with non-woven net spacers. *J. Memb. Sci.* **2004**, *232*, 19–30, doi:10.1016/j.memsci.2003.11.015.

## General conclusions and perspectives

*This section sums up the work set forth in the foregoing chapters. In section 6.1, the summary of each chapter, including two spacers that is proposed for the improvement of the performance of the spiral wound membrane, is summarized. In section 6.2, the contributions of this study to the spacer designing are considered. Activities that will be beneficial for further understanding of spacer design are proposed. Finally, in section 6.3 some possible directions for future research are suggested.*

### 6.1 Summary

- Chapter 1 of this thesis helps to shine a light on the importance of spiral wound membranes. This chapter goes further to explain the importance of the role of feed spacer in membrane separation.
- Chapter 2 gives a detailed explanation of membrane separation. It further explains the functioning of the membrane modules and finally gives an in-depth description of spiral wound modules. It also explains the basic definitions and concepts used in the studies of membrane modules. Finally, it goes into previous studies of feed spacer and gives in-depth reasons that flow pattern was focused on in the feed channel. Furthermore, the shortcomings of the conventional spacer are elaborated; and two new spacers are proposed.

- Chapter 3 deals exclusively with the computational fluid dynamics techniques used to simulate the fluid flow in the feed spacer. It describes the geometries of the feed spacer and the meshing methods. The governing equations of mass, momentum, and species conservation used in the CFD simulation are set forth, and the boundary conditions are described. The steps of CFD modeling applying in simulations are explained in details. The finite element method used in CFX, which used in this simulation, is detailed in three parts. Finally, the application of CFX in novel spacers simulation is explained for the next chapters.
- Chapter 4 displays the design of the pillar-like spacer. Optimization of flow pattern in feed spacer and energy saving are investigated through discussing the results of the fluid flow simulations. For CFD simulation, the result of the study yields that flow in the feed spacer is laminar. However, the non-steady component in the transient flow is very miniscule in the range of Reynolds numbers in which real feed spacers operate. Later, the initial conditions and the boundary conditions used for the simulation are described. The geometric periodicity of the feed spacer is used to simulate just one repeating unit of the feed spacer. A periodic boundary condition with an assigned flow driving pressure difference is used to simulate the flow through the repeating unit and extrapolated to the entire feed spacer screen. The boundary condition for the membrane is complicated as there are fluid transfer and mass transfer across the boundary. However, for reverse osmosis separation conditions, the feed water flow velocity in the feed spacer is a few thousand times as that of the permeate water flow velocity through the membrane. Therefore, the

velocity of the feed water flow through the membrane is neglected. Upon assessment, the difference in the velocity patterns is negligible between the two types of flow and hence a no-slip boundary condition is used to simulate the flow through the feed spacer repeating unit. The simulation of pillar-like spacer separated into three parts different diameters of connecting filament, different cross-sections of conjunction and different configurations of the connecting filament. In every part, four groups of setting were selected to do the simulation. Energy consumption and shear stress on membrane surface are focused on by comparing with the commercial spacer in order to clarify the characteristics of the pillar-like spacer.

- Chapter 5 displays the design of the arc-like spacer. For CFD simulation, according to Reynold numbers steady flow was selected in simulation. The same boundary conditions used in Chapter 4 were applied to simulate the arc-like spacer. Considering the structure and the conjunction of the arc-like spacer, to investigate the flow conditions in dead zone behind zigzag filament mesh quality was validated in CFX simulation. A mesh independency study is conducted to ascertain the reliability of the mesh. The importance of mixing enhancement close related concentration gradient near the membrane surface is explained. The comparison conducted to validate the predictions made by using the observations and the results of computer simulations for commercial spacer in previous studies. Four types of spacer were conducted which were defined by the distance of arc-like filament. The

simulation aimed at understanding the flow pattern in spiral wound modules through shear stress predicting.

## **6.2 Conclusions**

Membrane processes have been widely used in product recovery, waste water treatment and pollution control by the chemical, electronic, food and biotechnical industries. Successful industrialisation of membrane technology not only depends on the development of high performance membranes, but also modules housing these membranes. Flux losses caused by boundary layer effects highlight the importance of good design of commercial membrane modules since proper fluid management can greatly improve mass transfer and reduce boundary layer effects.

The spiral wound module can provide a large membrane area per module consequently improving the module productivity. The optimization of the spiral wound module design generally refers to the optimization of feed channel spacers, which was investigated in this thesis. The feed channel spacers serve to improve the mass transfer by promoting turbulence and provide passage for the fluid. However, the presence of spacers also significantly increases the channel pressure drop and consequently increases the energy costs of the process. The spacer design could therefore have a significant effect on process economics. This thesis investigated the characteristics of two novel spacers by computational fluid dynamics simulations.

With the development in modern computer technology, computational fluid dynamics (CFD) has become more and more frequently used in simulation of laminar flow, transitional flow and turbulent flow. In this thesis, CFD simulation was used to assist two

kinds of spacer design. CFD simulations provide detailed visualization of flow management that spacers could achieve in real time. The information provided by the simulation was used as an important guide in novel spacers development and spacer optimization. It revealed that spacers could assist mass transfer in two ways. One is introducing high shear stress or shear stress fluctuation at the membrane surface. Another is introducing eddy activity at the membrane surface. Eddies were formed both in front of and after each transverse filament. The peaks in shear stress were just above or beneath each transverse filament depending on the position of the spacer in the channel. The shear stress after the filaments gradually reduced until a trough value was reached and the shear stress then gradually increased again as the next filament was approached. The instability introduced by eddy activity or shear stress fluctuation may greatly benefit the mass transfer at the membrane surface.

The CFD simulation also revealed that the intensity of eddy activity and fluctuation of shear stress could be adjusted or optimized by arranging the distance between two spacer transverse filaments in order to maximize mass transfer at the membrane surface while controlling the frictional pressure losses. The simulation also showed that, the configuration of transverse filament defined flow situations which effect the dead zone and concentration gradient near the membrane surface in many previous studies. Novel spacers were developed based on these simulation prediction.

Previous experimental results for pressure drop revealed that the transverse filament was one of the dominant factors in spacer design. Most of the pressure drop in the spacer filled channel was caused by the form drag introduced by the transverse filaments.

The variation in transverse filament distance affects the number of transverse filaments in the channel and consequently affects the pressure drop in the channel. The main function of parallel filaments is to provide support for the transverse filaments, which produce most of the turbulence in the channel. The results showed that the diameter of the transverse filament also had a significant effect on channel pressure drop and mass transfer, especially at high flow rates. Increasing transverse filament diameter may result in a rapid increase in pressure drop and mass transfer caused by increased form drag and enhanced turbulence. Total form drag in the channel was significantly increased with increasing flow rate. As predicted by CFD modeling, novel spacers with transverse filaments suspended in the middle of the channel and curved structure, produced a significant reduction in pressure drop but generated comparable shear stress and turbulence at the membrane surface.

Furthermore, in a spiral wound module design, managing channel pressure drop is very important in controlling operating costs. The pressure drop is not only associated with the factors shown above, it also relates to the feed characteristics. For the same module, the pressure drop will be much greater when it deals with high viscosity fluid rather than low viscosity fluid. However, by combining the consideration of feed characteristics, productivity and factors shown above, the pressure drop in a spiral wound module could be optimized. The inlet pressure drop (pressure drop caused by the flow narrowing from pipe to the membrane leaves in the spiral wound module) should also be considered and minimized in the module design.

Pressure driven membrane processes usually suffer from concentration polarization and fouling caused by gradual build-up and deposit of dissolved and/or

suspended species near and on to the surface of membranes. Some degree of fouling control can be achieved by the appropriate choice of operating parameters. Accumulation of rejected species can be suppressed by creating back mixing from the membrane to the bulk of the liquid. There is a need alleviating the concentration build-up at a relatively lower pressure drop across the module. Spacers are introduced in membrane modules to separate membrane leaves and reduce fouling by modifying the fluid flow behavior. These spacers or turbulence promoters for spiral-wound and flat sheet modules are often net-like materials, which enhance mass transfer as well as provide passage for feed solutions. It is obvious that back mixing is more effective in spacer-filled channels than in empty channels. However, introduction of spacers also increases the pressure drop over the feed channel. Therefore, it is necessary to understand the role of spacer shape in resulting fluid dynamics of membrane modules. Such an understanding will allow optimization of spacer shapes to obtain an improved performance in terms of mass transfer and mechanical energy dissipation.

In this thesis the impact of feed spacer filament geometric parameters on performance of a spiral wound module was investigated. To enable flow visualization ANSYS CFX was used as the working tool and the predicted results showed excellent agreement with the previous experimental and other numerical studies. It reveals that CFD predicts hydrodynamics and mass transport within feed channel of spacer obstructed membranes quite accurately.

Spiral wound modules are very popular module applied in membrane process, and SWMs are widely used for commercial applications ranging from RO to UF. The major



problems for an SWM are concentration polarization, fouling and high pressure loss. The net spacer in the feed channel not only keep the membrane layers apart, hence providing passage for the flow, but also significantly affect the flow and concentration patterns in the feed channel. On one hand they are responsible for the pressure drop and limited flow zones (dead zones) creation, and on the other hand, they are responsible to promote mixing between the fluid bulk and fluid elements adjacent to the membrane surface. In other words, they are intended to keep the membranes clean by enhancing mass transfer and disrupting the solute concentration boundary layer. Several experimental and theoretical studies were carried out to shed light on these phenomena and to optimize spacer configuration. So it is quite understandable that the presence of these spacers promotes directional changes in the flow which reduces membrane fouling and concentration polarization. Hence the efficiency of a membrane module depends heavily on the efficacy of the spacers to increase mass transport away from the membrane surface into the fluid bulk by increasing shear rate at the membrane surface.

As an analysis tool, ANSYS CFX provides the ability to change operating conditions, fluid properties and geometric characteristics of the flow channels in a flexible and practical way. The geometric parameters of the channels simulated can be varied without the need to construct and test new spacer meshes. This represents a significant advantage of the ANSYS CFX technique over traditional experimental methods. For example, the fluid velocity, solute diffusivity and inlet concentration can be set at the start of the simulation, and there is no need for control of these variables. In addition, flow data can be reported at any position and time during the simulation, and the evaluation of these

flow variables is possible without any disturbance to the underlying flow. Unlike many of the previously reported ANSYS CFX studies for spacer and SWM module performance, this thesis focused on the effects on the improvement of flow pattern and mixing enhancement caused by the two novel spacers meshes in membrane modules. The study of 3D simulations provided for evidence their characteristics.

Haaksman et al. developed a method to obtain accurate three dimensional geometry representations for any given spacer design from X-ray computed tomography (CT) scans. In their study, the commercial spacers were investigated, and the results were agree with previous studies. Their results were used to compare with this study in order to clarify energy consumption and distribution of shear stress on membrane surface.

In this thesis, the objectives can be divided into two spacer designs. The pillar-like spacer was designed to optimize feed spacer geometry. Compared with the conventional spacer, the contact method of the pillar-like spacer with the membrane changed with the area contact. Hence, it was possible that the diameter of the connecting filaments (transverse filament) had decreased to maximize the channel porosity. The energy consumption and shear stress were analyzed using a numerical method, and the results were compared to those of commercial spacers studied in previous works.

The arc-like spacer was designed to enhance the mixing ability, which was constructed with arched filaments and zigzag filaments. In this arc-like spacer design, the filament, which was parallel to the flow direction, was set as the zigzag configuration, and the transverse filament facing the flow direction was set as the arched filament in order to enhance the mixing between the fluid bulk and fluid elements adjacent to the membrane

surface. Furthermore, the conjunction between the arched filament and zigzag filament had a small area of contact with the membrane, which reduced the dead zone caused by the shadow of the filament. The arched filament in the middle of the feed channel enabled the disruption of the solute concentration boundary layer.

The conclusions drawn from this thesis are summarized as follows:

1) To lower the obstacle effect from the feed spacer in the SW Membrane feed channel, the support from the high porosity of the feed spacer structures with a small filament diameter was indispensable. The pillar-like feed spacer was introduced as a new template to manipulate energy consumption. Under laminar flow conditions, the element of the feed spacer between membrane envelopes was simulated using the CFD method. Subsequently, the simulation parameters were compared and validated with previous works.

- Regarding the pressure drop, the decline in the connecting filament diameter of the pillar-like spacer and the rise in channel porosity reached 0.979. The inlet velocity was set at 0.04 m/s (at a constant flow rate), the channel porosity increased by 5%, and the pressure drop reduced by 62.56%. Compared with the results of previous works on conventional spacers and an empty channel, the current study's results on the pressure drop tended to be in agreement with them.
- For the friction factor, based on the numerical predictions, the results for the dimensionless power number and the modified factor agreed with previous conventional spacer results. At the Reynolds number of 150, the group  $d/a = 0.25$  friction factor reduced by almost 43.63% and 49.23% compared with the commercial

- spacers CON-1 and CON-2, respectively, and the dimensionless power number was lower than the commercial spacer CON-2 by almost 47.31% at the same Reynolds number for the same group.
- Regarding the shear stress, homogenization of distribution changed the flow profile close to the membrane. At the dimensionless power number  $10^6$ , the modified friction factor was enhanced by almost 20.40% and 22.27% compared to the commercial spacers CON-1 and CON-2, respectively.
  - The effect from conjunction cross-section on energy consumption was lower than the traverse filament. For the modified friction factor the same inclination was with friction factor and the dimensionless power number.
  - The configuration of connecting filament defined the distribution of shear stress on membrane surface. The partial shear stress increasing caused more energy consumption.

2) To achieve enhanced mixing, the modified feed spacer was designed as the transversal filament from the upper membrane to the lower membrane. This structure changed the flow patterns in the total feed channel compared with the conventional spacer. Reduction of the shadow zone behind the transversal filament was realized with the arched filament and the potential for mixing reached to the close vicinity of the filament.

Here, a CFD simulation result of the arc-like spacer was presented. Under laminar flow conditions, the element of the feed spacer between membrane envelopes was simulated. Subsequently, the geometry parameters of the arc-like spacer and this

simulation's parameter values were compared with previous works and validated. The results revealed the detailed flow pattern and shear stress distribution.

- When the main flow was normal to the arched filament, the area of the dead zone behind the zigzag filament, which was connected with the membrane, decreased with an increasing Reynolds number. In addition, the zone of vortex shedding behind the arched filament caused different flow fields, which generated a high gradient of velocity, improving the mixing of the feed solution.
- The investigated data of power consumption (friction factor) was approximated to the conventional commercial spacer. The value was a little lower than the commercial spacer at high Reynolds numbers when the main flow was normal to the arched filament. From comparison with previous work, it can be extrapolated that the changing of flow patterns from the structure of the arc-like space did not cause too much energy consumption.
- The value of the modified friction factor as a dimensionless number was similar to the results of previous work on commercial spacers when the main flow was normal to the arched filament.
- The effect of porosity (element length) on the energy consumption of the arc-like spacer was in agreement with previous studies, but on shear stress, was smaller. This conclusion was indicated by re of sult lines qualitatively.

3) Spacer using should not only consider the productivity gains achieved by the spacers. Other factors such as feed characteristics should also be considered. For example, for feeds of low concentration and low viscosity, the selection of spacers is reasonably

flexible. However, for high viscosity fluids, or high concentration of particles, feed properties may substantially affect the spacer/membrane performance. Some spacers may block severely and consequently reduce the membrane productivity. Novel spacers, in which the transverse filaments are suspended in the channel, such like for the pillar-like spacer the connecting filament was set in the middle of the feed channel, may avoid the dead zone in which caused high concentration polarization and severe spacer block. Furthermore, for the are-like spacer the arc filament was set crossing the feed channel may possess an improved ability to mix feeds with high concentration.

### **6.3 Perspectives**

- CFD application in membrane processes

CFD simulation results here provided detailed visualization of flow management of different spacer arrangements and useful information to guide novel spacer design. The successful application of CFD modeling in this thesis suggests that it should be more widely used for research into membrane processes, especially to assist with module design. The simulation of membrane systems requires the proper application of boundary conditions and transport models. If suitable boundary conditions and mass transfer models can be established, CFD modeling may provide very useful visualization of concentration polarization and fouling in spacer design. CFD simulation could also be used in the simulation of fluid management concepts for membrane modules. For example, in the novel membrane module design different structures compare with conventional structures.

- Experimental study

The ratio between transverse filament diameter and separation distance and the ratio between transverse filament diameter and channel height are every important in determining mass transfer and pressure drop in the spiral wound module. Spacers designed in this thesis with the different structures comparing with the conventional spacer. While some observations of the effect of diameter and the configuration were made, the numerical simulation provides excellent agreement with the commercial spacer at the inclination of results. Because of the different structure, the further experimental study would be worthwhile for validating the numerical simulation results.

– Fouling study

In spiral wound membrane systems, colloidal, inorganic, organic, and biological are four major types of fouling occurred in separation process. The formation of a fouling layer, as dominant fouling mechanism on the membrane surface, is considered in previous studies. Moreover, the physicochemical properties of the membrane surface and the feed spacer geometry are major factors influencing membrane fouling indicated by many papers. In four types of fouling, because of microorganisms multiplying biofouling is the major fouling type of the membrane process, even if in feed pre-treatment 99.9% of microorganisms are removed. Due to more than 45% contribution to all membrane fouling biofouling has been reported as a major problem in nanofiltration (NF) and reverse osmosis (RO) membrane filtration. The increase in the hydraulic resistance and the trans-membrane osmotic pressure caused by biofouling are relate to the decline of in permeate water flux and the decrease of salt rejection. Because the increase in the trans-membrane osmotic pressure is defined by bacterial cells deposition. In this thesis, the hydrodynamic influence

caused by the geometry of two novel spacers on fouling was focused on. Biofouling is worthwhile to discuss in future work.

– Economic evaluation

In water treatment the large difference was contribute by the capital and operating costs at different regions and facilities. Through concerning the details of the parameters and methodologies used for local conditions the consultants realize calculation methodologies for operation cost of plants. The selection of feed spacers is vital to the main parameters influencing the total water cost applied in different separation technologies. The related improvements in feed spacer design present to cost reduction as well as the reduction in energy consumption. Most of the illustrative economic analysis which includes operating costs related to pressure drop related and capital costs related to flux is used to identify optimal spacer designs for different membranes. Two kinds of novel spacers designed in this thesis suggested a new template to higher mass transfer and lower energy loss. The economic evaluation for real life would be worthwhile.